Hypervelocity Flow over Spheres

Thesis by

Chihyung Wen

In Partial Fulfillment of the Requirements

for the Degree of

Doctor of Philosophy

California Institute of Technology

Pasadena, California

1994

(Submitted Feburary 7, 1994)

to
my parents and my wife

Acknowledgments

I wish to express my deepest gratitude to my advisor, Professor Hans Hornung, for his guidance, patience, and support throughout the whole course of my graduate studies at Caltech. His dedication to scientific research, combined with his attitude of being a friend to his students, makes him the very best advisor any graduate student can have.

I wish also to thank all the GALCIT members for contributing to various aspects of this research and making GALCIT such a friendly place to be. In particular, I would like to thank Professor Dale Pullin, Professor Bradford Sturtevant, and Professor Anatol Roshko for many enlightening discussions and T5 team members Jacques Bélanger, Eric Cummings, Patrick Germain, Simon Sanderson and Bahram Valiferdowsi for their help and advice.

Special thanks to Professor Graham Candler of the University of Minnesota for providing the computation program and kind collaboration.

Finally, I thank my family, especially my wife Chuanyao, for their hearty encouragement and constant support.

Abstract

The nature of the nonequilibrium flow of dissociating gases over spheres was investigated experimentally, numerically and theoretically. A series of experiments with three different gases, nitrogen, air and carbon dioxide, was performed in the shock tunnel T5 at GALCIT. Five spheres of different radii equipped with thermocouples for surface heat flux measurements were used. The state-of-the-art numerical method by Candler (1988) was used to conduct a parallel study which strongly complemented the experimental and theoretical efforts.

Experimental heat flux measurements are presented. Good agreement was observed among the measured stagnation point heat transfer rates, computational results and Fay and Riddell's theoretical predictions. For nitrogen and air, the measured heat flux distributions were also in good agreement with numerical computation results and Lees' theory. For carbon dioxide, large deviations were observed. Early transition tripped by surface roughness is a possible cause for the deviation of heat flux distribution from the theory. The experimental differential interferograms were compared with the images constructed from computational flowfields. Good agreement of fringe pattern and shock shape was observed.

An analytical solution is obtained for inviscid hypervelocity dissociating flow over spheres. The solution explains the correlation between the dimensionless stand-off distance and the dimensionless reaction rate parameter previously observed by Hornung (1972) for nitrogen. The physics of the correlation can be shown as the binary scaling. Based on the solution, a new dimensionless reaction rate parameter is defined to generalize Hornung's correlation for more complex gases than nitrogen. Experimental and numerical results confirm the new correlation.

The effect of nonequilibrium recombination downstream of a curved two-dimensional shock was also addressed. An analytical solution for an ideal dissociating gas was obtained, giving an expression for dissociation fraction as a function of temperature on a streamline.

The solution agrees well with the numerical result and provides a rule of thumb to check the validity of binary scaling for the experimental conditions. The effects upon the binary scaling of the large difference in freestream temperature between flight and free-piston shock tunnel conditions are discussed.

Table of Contents

List of Figures

List of Tables

List of Symbols

English Symbols

A	recombination factor in Eq. (6.10)
A_1	defined by Eq. (6.19)
a	nose radius of sphere
a_f	frozen speed of sound
B	recombination factor in Eq. (6.10)
B_1	defined by Eq. (6.20)
b	defined by Eq. (6.12)
C	reaction rate constant, see Eq. (5.44)
c	specific heat of a solid material
c_p, c_{pi}	specific heat at constant pressure of the gas mixture, species i
c_s	mass fraction of species s
$c_{v trans}, c_{v rot}$	translational, rotational specific heat
D	diffusion coefficient
E	total energy per unit volume
E_v, e_v	vibrational energy per unit volume, mass
e	electromotive force of the thermocouple
e_v^*	equilibrium vibrational energy per unit mass
$F^\star$	defined by Eq. (6.7)
$G^\star$	defined by Eq. (6.7)
g_r	degeneracy of mode r
h	enthalpy
h^0	heat of formation
K	heat transfer coefficient defined by Eq. (4.9), $\mathrm{kg/(s\text{-}m^{3/2}\text{-}atm^{1/2})}$
K	defined by Eq. (5.28)
K_c	equilibrium constant of reaction,see Eq. (5.43)

K_i	Gladstone-Dale constant of species i
K_r	defined by Eq. (6.27)
k	heat transfer coefficient defined by Eq. (4.10)
k	heat conductivity
$k_{f,1}, k_{f,2}$	forward reaction rate constants, see Eq. (5.42)
k_{v_s}	conductivity of e_{v_s}
L	constant defined by Eq. (5.24)
Le	Lewis number
M, M_i	molecular weight of the gas mixture, species i
M_{N_2}	molecular weight of nitrogen
Ma	Mach number
$\hat{N}$	Avogadro number
n	refractive index; total number of species
n_0	reference refractive index
Pr	Prandtl number
P_{sr}	probability of a r to s $v - v$ exchange
p	pressure
Q	integrated heat
Q_{T-v}	translation-vibration energy transfer rate
Q_{v-v}	vibration-vibration energy transfer rate
q_v	vibrational heat flux
$\dot{q}$	heat transfer rate
R	universal gas constant
Re	Reynolds number based on diameter
Re_x	local Reynolds number defined by Eq. (4.20)
r_{sh}	radius of curvature of the shock
S	rule of thumb for binary scaling, see Eq. (6.33)
s	specific entropy
St	Stanton number

St_x	local Stanton number defined by Eq. (4.21)
T	temperature
T_v	vibrational temperature
t	time variable
U_1	vector of conserved quantities
U_2, U_3	inviscid fluxes in x and y directions
U_{2v}, U_{3v}	viscous fluxes in x and y directions
u	velocity component in the x-direction
u_i	velocity component in the i-direction
$V^\star$	flow speed, sed Eq. (6.6)
v	velocity component in the y-direction
v_{sj}	diffusion velocity of species s in j-direction
W	vector of chemical source term
w	chemical source term
x_j	spatial coordinate in j direction
Z_{sr}	s-r collision number per unit volume

Greek Symbols

α	atomic mass fraction
Γ	$\equiv \sum_{i=1}^{n} c_i / M_i \equiv 1/M$, see Eq. (5.16)
γ	ratio of specific heats
$\bar{\gamma}$	mean ratio of specific heats in shock layer
ϕ_{opt}	phase shift of the object beam
Δ	stand-off distance
$\bar{\Delta}$	dimensionless stand-off distance defined by Eq. (5.4)
δ	Dirac's delta function, see Eq. (3.2)
ϵ	Constant parameter defined by Eq. (6.1)
η	reaction rate constant, see Eq. (5.44)
θ_d	characteristic temperature of dissociation
θ_v	characteristic temperature of vibration

κ_0	radius of curvature of the shock
λ	wavelength; parameter defined by Eq. (6.14)
μ	viscosity; dimensionless parameter defined by Eq. (5.1)
ν	defined by Eq. (6.22)
$\hat{\mu}$	specific chemical potential defined by Eq. (5.7)
ξ	defined by Eq. (6/13)
ρ	density
$\bar{\rho}$	average density in the shock layer
ρ_b	density on the body
ρ_d	characteristic density of dissociation for IDG
ρ_{eq}	equilibrium density
σ	defined by Eq. (6.14)
τ_{ij}	stress tensor
τ_s	vibration relaxation time
Υ	density slope parameter at the shock (see Eq. (5.33))
Λ	dimensionless parameter $(\equiv a C \rho_\infty \theta_\infty^n / u_\infty)$
Ω	dimensionless reaction rate parameter defined by Hornung (1972); Damköhler number, see Eq. (5.2) and Eq. (5.29)
$\tilde{\Omega}$	new dimensionless reaction rate parameter defined by Eq. (5.52)

Superscript Symbols

$\star$	dimensionless quantities, see Chapter 6

Subscript Symbols

e	value at the edge of boundary layer
eff	effective shock values, see Chapter 6
r	shock conditions at which recombination becomes important, see Chapter 6
s	value of chemical species s; value at stagnation point
sh	value just after the normal shock wave, see Chapter 5; values just downstream of the shock wave, see Chapter 6
w	value at the wall

0   reservoir, or total value(in the case of h: specific)

∞ freestream or upstream of the shock layer

CHAPTER 1

Introduction

The recent human endeavor to build vehicles to traverse the atmosphere of the planets of the solar system in the hypervelocity regime, such as NASP in the United States, HERMES in Europe, and HOPE in Japan, has revived the research activities in chemical nonequilibrium flow. The term "hypervelocity" is used in distinction from the term "hypersonic". In hypervelocity flows, the stagnation enthalpy can be large enough to cause dissociation of the gas after the bow shock ahead of a blunt body. The term "hypervelocity" implies not only high Mach number but also very high freestream velocity. The term "hypersonic" flow is used to describe situations in which the flow speed is several times higher than the freestream speed of sound. It can, of course, be generated by lowering the speed of sound without increasing the flow speed. In such "cold" hypersonic flow, the flow still behaves as a perfect gas and the important dissociative and other real-gas effects of a hypervelocity flow will not occur.

The nature of chemical nonequilibrium flows about blunt bodies is important in the aerodynamic design of orbital vehicles. Stalker (1989) has pointed out that models using frozen or equilibrium chemistry are unable to predict the nonequilibrium flow field. One important difference was found when the shuttle Orbiter experienced a pitching moment significantly different from the pre-flight predictions (Maus, Griffith & Szema, 1984). These predictions were obtained from extensive cold hypersonic wind-tunnel testing in facilities which could not produce the real gas effects.

In the present study, some aspects of hypervelocity flow over spheres with nonequilibrium chemical reactions are investigated through theoretical derivations and a series of computations and experiments using nitrogen, air, and carbon dioxide as test gases. The latter gas is of interest in Martian atmospheric entry, where the atmosphere is composed

primarily of carbon dioxide. It also exhibits more dramatic real-gas effects than air or nitrogen because of the large fraction of energy that goes into vibration and dissociation.

1.1 A Review of Previous Work and Motivation

It is clear that very substantial chemical activity will take place in hypervelocity blunt body flow. Because of the complex idiosyncrasies of air or carbon dioxide at such high specific energy, it is not possible to simulate them with other gases, and we are necessarily forced to reproduce the actual flow speed that the body sees.

A second feature of the problem is that in many parts of the flow field around a body, the chemical reactions occur at speeds which are comparable to the local flow speed, so that it is necessary to study not only equilibrium high-enthalpy effects but also those that arise because of the finiteness of the chemical reaction rates. These, by virtue of the flow speed, introduce characteristic lengths into the problem, which depend on the properties of the gases as well as on the flow variables. Two kinds of chemical reactions may broadly be distinguished: binary and ternary reactions, for which the characteristic lengths vary as the inverse of the freestream density and as the inverse of the square of the freestream density, respectively. In a simulation where one wishes to reproduce the ratio of body size to characteristic chemical length, it is therefore necessary to reproduce

$$\rho_\infty a \qquad \text{or} \qquad \rho_\infty^2 a \ ,$$

depending on whether binary or ternary reactions are dominant in the phenomenon of interest. It is not possible to simulate situations involving both types correctly except at full scale.

The features of hypervelocity blunt body flow have been studied extensively both theoretically and numerically. Hall *et al.* (1962) have shown that binary reactions dominate the features of blunt body flows at high altitudes where the density is low and the atom concentrations are effectively frozen in the nose region after a short distance behind the curved shock wave. "Binary scaling" then provides an important scaling for the ground testing of

nonequilibrium flow fields. Gibson and Marrone (1964) concluded that for two different flows with the same freestream velocity, temperature, and dissociation fraction, but different values of the freestream density and radius, the chemical nonequilibrium flowfields with the coordinate system scaled by the radius a will be the same if the binary scaling $\rho_\infty a$ is the same between the two flows. Since the above considerations formed the core of the simulation principle of the ground testing facilities, the validity of binary scaling in experimental environments needs to be checked.

In an earlier numerical and experimental investigation of the effect of chemical nonequilibrium effects on blunt-body flows, Hornung (1972) has shown that the stand-off distance and flow pattern of nonequilibrium dissociating flow of nitrogen over the front part of a blunt body can be correlated in terms of a single reaction rate parameter Ω, which is an effective Damköhler number and is the ratio of the chemical reaction rate to the flow rate, taking account of parameters describing the speed, density, dissociation, and temperature of the freestream. In Hornung's experimental results using optical interferometry in a free piston shock tunnel, T3 , the density was too low to get good resolution of the fringe shift of flows over spheres. For that reason the investigation was made using cylinders, where the path length of light was significantly larger. Unfortunately, the end expansion effects involved in such flows manifest themselves in just the same manner as the nonequilibrium effect and therefore obscure it. Macrossan (1990) also suggested that the driver gas contamination is a further limitation on the accuracy in the stand-off distance for high enthalpy conditions in T3. With the new shock tunnel at GALCIT, T5, much higher density can be achieved, and sphere-flow interferograms produce as many as 15 fringes, see Hornung *et al.* (1994), giving excellent resolution. The size and density achievable in T5 has now extended the available parameter range sufficiently to avoid the end-effect problem by studying the axisymmetric situation, *i.e.*, by using spheres as models. It is also interesting to try to explain the physics of the correlation.

Hornung (1976) performed an approximate analysis of the nonequilibrium flow behind a curved shock wave, under the assumption that binary reactions are dominant. He concluded that the flow could be conveniently divided into a region of intense dissociation

close to the shock followed by a large region of chemically frozen flow, which confirmed the numerical results mentioned earlier in this section by Hall *et al.* (1962). Macrossan (1990) has shown that the recombination reaction is not negligible at the higher values of the density in the test section of the free piston shock tunnel, although, further downstream the flow is frozen again. Macrossan's results motivate us to relax Hornung's binary reaction assumption and to understand the mechanism which 'freezes' the recombination.

Aerodynamic heating in hypersonics is another major problem for hypersonic cruise. Lees (1956) outlined the pioneering theoretical study of the laminar heat transfer rate to a blunted cone and a sphere based on the self-similar solution of the hypersonic boundary layer. Fay and Riddell (1958) obtained the most well-known correlation of the stagnation point heat transfer rate for a diatomic dissociating gas. Sutton and Graves (1971) have generalized Fay and Riddell's analyses to arbitrary gas mixtures, including polyatomic dissociating gases. Koppenwallner (1984) correlated several investigators' experimental data of the stagnation point heat transfer rate over the hemisphere-cylinder in hypersonic flows. He also provided the heat flux distribution downstream of the stagnation point. Most of these experimental results on heat transfer rates through highly cooled boundary layers have been obtained from measurements made in shock tubes. These experiments correctly simulate the stagnation enthalpy which is the parameter of major interest in heat transfer measurements. However, the Reynolds number is always low. The free piston shock tunnel T5 can operate at Reynolds numbers based on the diameter of the model up to one million and stagnation enthalpies up to 25 MJ/kg. The size of the model is also much larger than those used in the shock tube, so that nonequilibrium effects can be studied without the size constraint of the model.

At the same time, the development of numerical methods for the computation of blunt body flow fields has become very much quicker since the 1970's, so that even interferograms of three-dimensional chemically reacting flows can be computed with reasonable speeds, see *e.g.*, Rock *et al.* (1992) and Hornung *et al.* (1994). For laminar flow, the viscous case is also accessible, so that heating rates too may be compared with theoretical models, see *e.g.* Candler (1988). Since the shock values of temperature, vibrational temperatures and

density are not accessible during the experiment, the computational method provides a good way to obtain partial information about them.

The following chapters present an investigation in T5 of the blunt body problem and the limits of binary scaling, and the accompanying computational and theoretical works.

1.2 The Scope of the Current Work

The thesis is divided into eight chapters, including this introduction. A short description of the experimental facility – the free piston shock tunnel T5, models, the instrumentation and flow visualization techniques is presented in chapter 2. Chapter 3 describes the numerical code, the computational interferometry, and the program to extract solutions on a streamline from the computed flow field. The results of heat transfer measurements and examples of experimental interferograms are compared with their computational counterparts in chapter 4. An analytic solution of the correlation between the dimensionless stand-off distance and the dimensionless reaction rate parameter, Ω, for nitrogen found by Hornung (1972) is first derived in chapter 5, using the Lighthill-Freeman gas model. The analytic solution is then compared with the numerical and experimental results. To generalize Hornung's correlation for more complex gases than nitrogen, a new dimensionless reaction rate parameter, $\tilde{\Omega}$, is defined. Numerical and experimental results of the correlation between the dimensionless stand-off distance and $\tilde{\Omega}$ for air and carbon dioxide are also presented. In chapter 6, the effect of nonequilibrium recombination after a curved shock wave in a hypervelocity dissociating flow of an inviscid Lighthill-Freeman gas is considered. A rule of thumb to check the validity of binary scaling is also derived. Numerical examples are presented and the results are compared with solutions obtained with two-dimensional Euler equations using Candler's code (1988). One of the interesting features of hypervelocity blunt-body flows, namely the vorticity concentration associated with the edge of the high-entropy layer generated in the nose region by the curved shock, will be touched upon in chapter 7. Also included is the first attempt at the experimental and computational verification of various vibrational energy relaxation models. Chapter 8 is a conclusion of the research.

CHAPTER 2

Experimental Method

This chapter presents a description of the experimental facility, the instrumentation of the facility and the models, the data acquisition system, and the flow visualization techniques. The method to determine the freestream conditions is also described.

2.1 Experimental Facility

The GALCIT free-piston shock tunnel T5 which has the specific aim of studying the fundamental features of high-enthalpy reacting flows was used for the experiments. The facility was named T5 in honor of its Australian predecessors T1 to T4. The facility uses the principle of free-piston adiabatic compression of the driver gas of a shock tunnel to achieve the high shock speeds and densities required to generate the high enthalpy and reaction scaling. It is capable of producing flows of air or nitrogen up to specific reservoir enthalpy of 25 MJ/kg at reservoir pressure up to 100 MPa and reservoir temperature up to 10000 K. Helium is usually used as the driver gas because it is a light gas and has no low-energy internal degrees of freedom and hence behaves like a perfect gas up to relatively high temperatures. The shock tunnel has two additional essential features. One is that the test duration is sufficiently short (typically 1 ms) to avoid destruction of the machine by melting, yet long enough to provide good measurements during the steady-flow period. The other is that the gas is partially dissociated at the nozzle exit, especially in the cases of air and carbon dioxide at high specific reservoir enthalpies, where they also contain some nitric oxide and carbon monoxide. The schematic of the facility is shown in Fig. 2.1 and its primary parameters are summarized in Table 2.1.
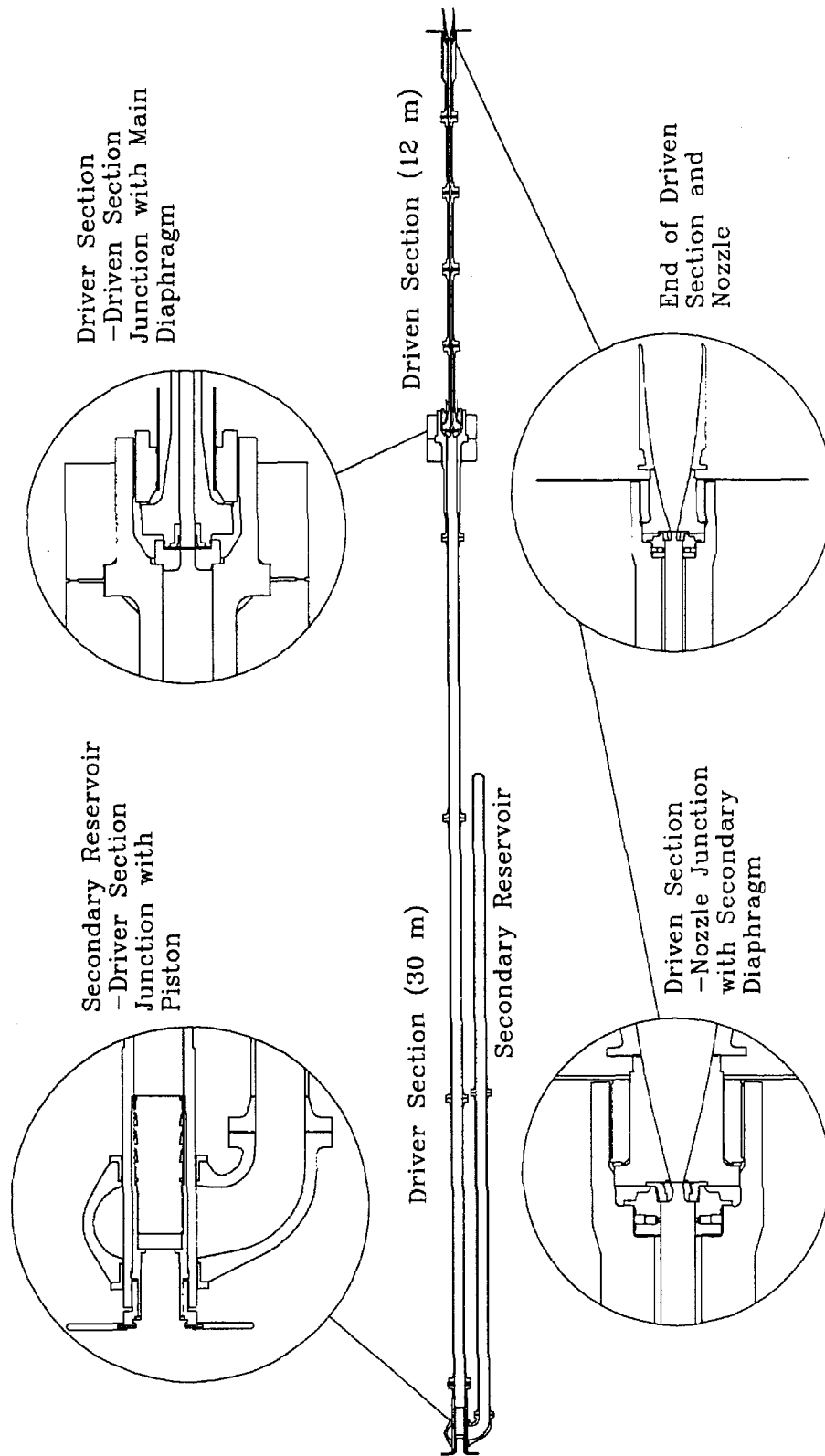
FIG. 2.1. Schematic drawing of the free-piston shock tunnel T5 with details of the critical section.

Maximum diaphragm burst pressure	130 MPa
Maximum secondary reservoir pressure	15 MPa
Driver section diameter	0.3 m
Driver section length	30 m
Driven section diameter	0.09 m
Driven section length	12 m
Piston mass	120 kg
Nozzle exit diameter	0.3 m

Table 2.1. Primary parameters of T5.

In a typical run, the secondary reservoir is filled with compressed air at 10 MPa, the driver section contains helium at 120 KPa, and the driven section contains air at 20 KPa. The driver and driven sections are separated by a main diaphragm of a 7 mm thick stainless steel 304 plate with a burst pressure of 100 MPa. The diaphragm has two grooves which cross normal to each other (for more detail, see Cummings (1993)). This pre-stressed groove configuration improves dramatically the repeatability of the desired burst pressure and it produces very little debris at the test section. When the piston is released, it is accelerated by the compressed air to a maximum speed of about 300 m/s. The piston compresses the helium to 1/55 of its original volume and heats the helium to around 4600 K at diaphragm rupture. A strong shock wave is formed and propagates in the shock tube at 4.6 km/s. The incident shock will reflect off the end wall and creates a reservoir region. The reservoir enthalpy is about 21 MJ/kg, the reservoir pressure is about 75 MPa, and the reservoir temperature is about 9000 K. The gas is then expanded through a contoured nozzle of 300 mm exit diameter and 30 mm diameter throat, producing a flow of about 6 km/s.

As the piston accelerates along the driver section, this center of mass shift is compensated by a recoil of the driver section, driven section and nozzle. The test section and dump tank remain stationary, and the secondary air reservoir recoils in the opposite direction under the action of the thrust of the outflowing air. To accommodate the resulting relative

motions, the joints at the nozzle and at the launch manifold are fitted with sliding axial seals. The recoil speed determines the level at which the tube is stressed by a wave released by the rapid piston deceleration. This and other considerations make it desirable to reduce the recoil speed as much as possible. For this reason a substantial inertial mass of 14 tons (prominent in Fig. 2.1) is fixed to the high-pressure end of the driver section, the origin of the stress wave. The recoil distances are typically 100 mm and 150 mm for driver section and secondary air reservoir respectively.

A more detailed description of T5 and its performance envelope, flow quality and repeatability may be found in Hornung (1992).

2.2 Instrumentation of the Facility

2.2.1 Data Acquisition System (DAS)

DSP Technology's TRAQ system, a modularized system to acquire analog or digital data from multiple input channels, was used to acquire the experimental data. The current modules of the data acquisition system are summarized in Table 2.2, and the schematic of the system is shown in Fig. 2.2.

Each of the forty A/D digitizers has a resolution of 12 bits and a maximum sampling rate of 1 MHz. The total through-put is limited to 16 MSamples/s. The system is controlled from a Sun SPARCstation computer with software facilities enabling 'quick-look' examination of the data immediately after the shot. For these experiments, the sampling rate was 200 kHz and each digitizing channel had 4 kByte length. 1/8 of the memory of each digitizing channel was pre-trigger data.
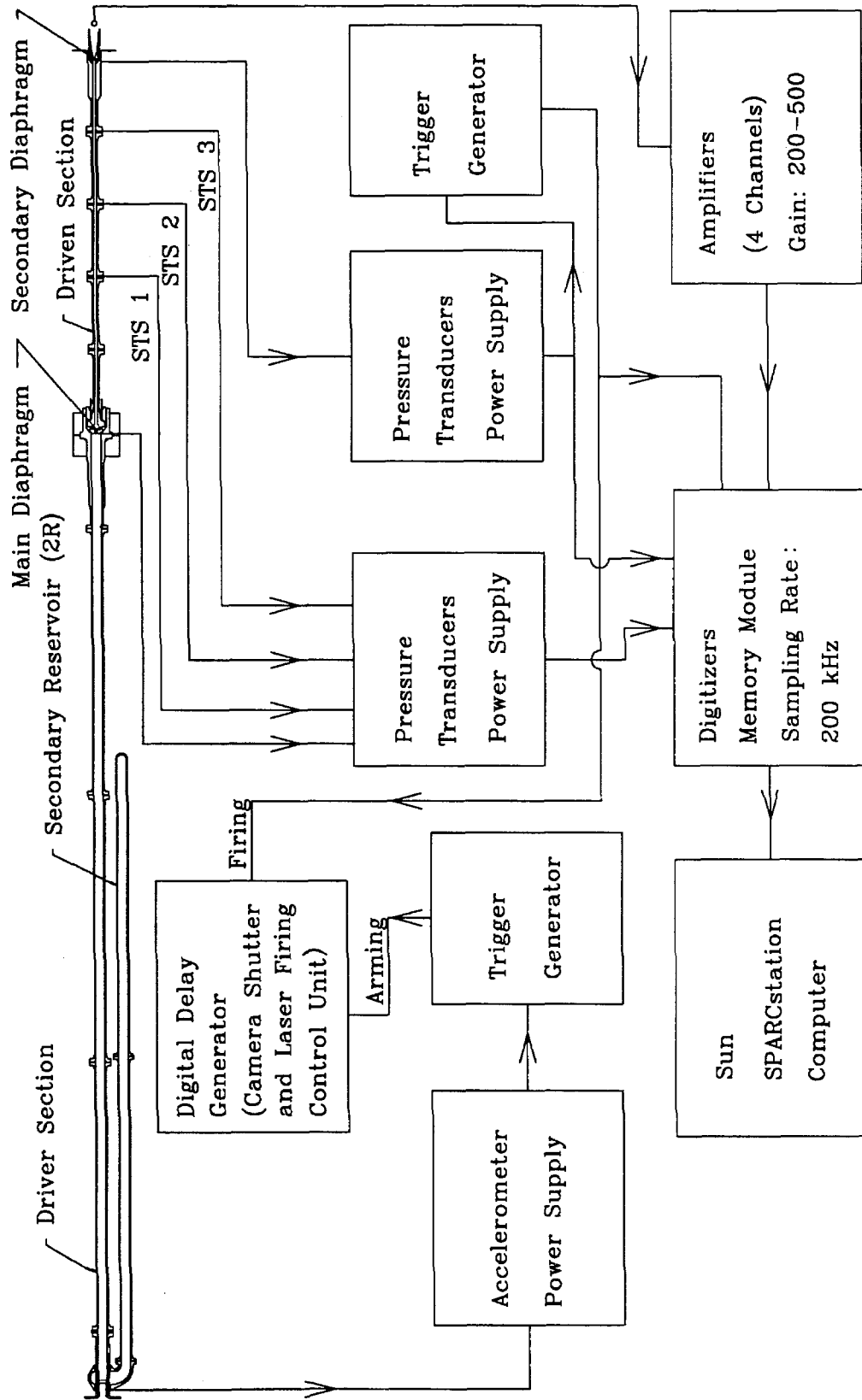
FIG. 2.2. Schematic diagram of the data acquisition system arrangement.

Module	Number of channels
Enhanced TRAQ controller (DSP 4012A)	1
Memory module (DSP 5200)	1
A/D digitizer (DSP 2860)	40
Trigger generator (DSP 1024)	8
Amplifier (DSP 1402E)	24
Digital counter	1
Digital delay generator	1
PCB piezotronics pressure transducer power supply	24

Table 2.2. Primary modules of the data acquisition system.

2.2.2 Pressure and Shock Speed Measurements

Seven PCB Piezotronics Inc. pressure transducers (Model number 119M44) were used for the shock tunnel. A pair of pressure transducers were installed at the end of the driver section to monitor the burst pressure of the diaphragm. Another pair of pressure transducers were installed at the end of the driven section to record the nozzle reservoir pressure history and two signals were linked to an OR logic controller in the trigger generator to insure the triggering of the whole data acquisition system. The other three pressure transducers were mounted in three shock-timing stations (STS) along the driven section to obtain the shock speed. For the experiments, the shock speed is calculated from the distance separating station 2 and 3 divided by the time difference of the signal rise. Fig. 2.3 shows the typical pressure traces of three shock-timing transducers and one of the nozzle reservoir transducers during a run. Because the nozzle reservoir pressure and the shock speed are two important parameters in calculating the freestream conditions at the nozzle exit, the repeatability of these two parameters must be addressed. Hornung (1992) has demonstated that the repeatability of the nozzle reservoir pressure and the shock speed for T5 is $\pm$ 4% and $\pm$ 1%, respectively.
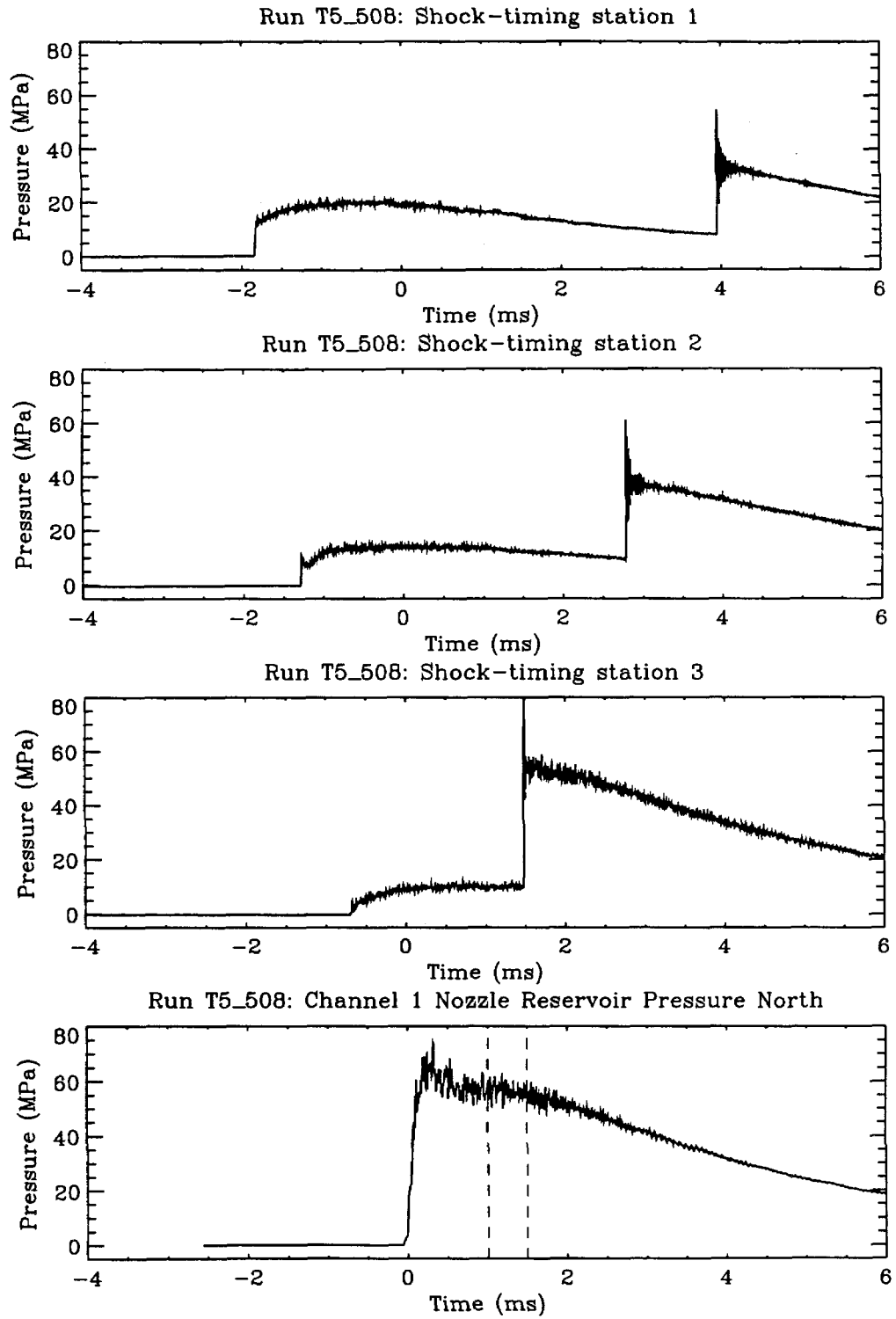
FIG. 2.3. Time traces given by three shock-timing pressure transducers and one of the nozzle reservoir pressure transducers (during a experiment). The velocity of the incident shock wave is obtained from the distance separating station 2 and 3 divided by the time difference of the signal rises. The fourth pressure trace gives the value of p_0, the average of the signal between $t = 1.0$ ms and $t = 1.5$ ms is made.

2.3 Free Stream Conditions

An equilibrium shock tube calculation (ESTC) code (McIntosh, 1970) was used to calculate the nozzle reservoir conditions. The measured shock speed and the initial test gas pressure, composition, and temperature were used to evaluate the conditions behind the incident and reflected shocks. The nozzle reservoir conditions were then obtained by changing the conditions after the reflected shock isentropically so that the total pressure matched the measured nozzle reservoir pressure. These reservoir conditions are then used as the input of a quasi one-dimensional nonequilibrium nozzle calculation NENZFG (Lordi *et al.*, 1965) or an axisymmetric inviscid nonequilibrium flow calculation SURF (Rein, 1989) to give the freestream conditions at the nozzle exit. Table 2.3 gives the ranges of the reservoir and freestream conditions chosen for the present investigation. The Mach number of the freestream is about 5.5 for nitrogen, 5.3 for air, and 4.6 for carbon dioxide. The shot number, reservoir and freestream conditions of each run in this study are listed in detail in tables in Appendix A.

parameter	p_0(MPa)	h_0(MJ/kg)	u_∞(km/s)	T_∞(K)	ρ_∞(kg/m^3)
Nitrogen					
from	30	10.58	4.2	1390	0.0175
to	90	21.06	5.5	2760	0.0561
Air					
from	30	9.81	3.9	1340	0.0152
to	90	22.15	5.6	2930	0.0627
Carbon dioxide					
from	30	4.5	2.5	1130	0.0326
to	90	11.95	3.6	2400	0.162

Table 2.3. Range of values of reservoir and freestream conditions chosen for experiments.

2.4 Model, Instrumentation of the Model, and Data Reduction

2.4.1 The Model and its Instrumentation

The models chosen were a set of spheres with diameters 1, 2, 3, 4, and 6 in. in order to vary the reaction rate parameter at a given tunnel condition. This has an upper limit of 6 in. because of the useful diameter of the flow, and a lower limit of 1 in. because of the resolution of the optical system. The models were made of stainless steel 302 for the considerations of strong pressure load, durablility and matching as nearly as possible the value of heat transfer constant $\sqrt{\rho c k}$ to that of the thermocouple material to maintain the surface continuity of the convective heat transfer rate and obtain accurate measurement of the rapidly changing surface temperature. With the extremely high values of heat flux encountered at the stagnation point of the sphere, the classical thin-film metal gauges are not suitable. Thermocouple gauges were found to serve our purpose very well. Therefore, four Medtherm coaxial thermocouples of type E (chromel-constantan) were mounted flush with the surface of the sphere to measure the heat transfer distribution for the 2, 3, 4, and 6 in. model. They are 1.6 mm in diameter and are mounted at the stagnation point and 20°, 40°, and 60° from the stagnation point. For the 1 in. model, only the stagnation point heat transfer rate was measured. The response time of the thermocouples is about 1 μs and the recommended temperature range is from 78 to 1270 K, according to the manufacturer. The response time is more than adequate for the test time of T5, which is about 1.5 ms. The junction was formed by gently sanding the surface to be exposed to the flow. The cold junction was the feed-through plate for signal cables between the test section and the laboratory. A PCB Piezotronics Inc. pressure transducer was used for Pitot pressure measurement.

The sphere was positioned at zero incident angle and with the stagnation point just at the nozzle exit before the test to avoid the interference of the expansion wave from the edge of the nozzle after the recoil. The centerline of the sphere-sting assembly was set 0.5 in. below the centerline of the nozzle to avoid the shock-focusing from the nozzle. All the thermocouples were in the lower half-sphere. The Pitot probe was set far enough

away in order not to interfere with the sphere flow. The method used to make sure that the centerline of the sphere-sting assembly is parallel to the centerline of the nozzle is described in Germain (1993). Fig. 2.4 shows the schematic of the arrangement of the test section.

2.4.2 Data Reduction

The emf signals of thermocouples of type E were converted to temperature by a polynomial fit (see Avallone and Bannierster, 1987) :

$$T\ (K) = Ae\ +\ Be^2\ +\ Ce^3\ +\ Dc^4\ , \tag{2.1}$$

where

$$A = 17.022525$$

$$B = -2.209724\ \times 10^{-1}$$

$$C = 5.4809314\ \times 10^{-3}$$

$$D = -5.7669892 \times 10^{-5}\ ,$$

and e is in mV. The one-dimensional semi-infinite slab theory was then used to reduce the time history of the surface temperature to heat flux, given that the test time is short compared to the heat penetration time into the gauge (see Schultz and Jones, 1973):

$$\dot{q} = \sqrt{\frac{\rho ck}{\pi}} \int_0^t \frac{dT(\tau)}{d\tau} \frac{d\tau}{\sqrt{t - \tau}}\ , \tag{2.2}$$

where the thermal product $\sqrt{\rho ck}$ for the gauge material was determined to be 8919 W/(mK). The indirect method, in which integration was performed first to compute the cumulative heat input $Q(t)$ and then the differentiation to obtain $\dot{q}$, was used to process these data numerically. The cumulative heat input to a semi-infinite solid is given by

$$Q(t) = \sqrt{\frac{\rho ck}{\pi}} \int_0^t \frac{T(\tau)}{\sqrt{t - \tau}} d\tau\ , \tag{2.3}$$

and the finite-difference representation is

$$Q(t_n) = \sqrt{\frac{\rho ck}{\pi}} \sum_{i=1}^n \frac{T(t_i) - T(t_{i-1})}{\sqrt{t_n - t_i} + \sqrt{t_n - t_{i-1}}} (t_n - t_{n-1})\ . \tag{2.4}$$

FIG. 2.4. Schematic of the arrangement of the test section.

An expression for differeniating the discrete function $Q(t)$ is

$$\dot{q}(t_n) = \frac{dQ(t_n)}{dt} = \frac{1}{40\,(t_n - t_{n-1})}\,(-2Q_{n-8} - Q_{n-4} + Q_{n+4} + 2Q_{n+8})\ . \qquad (2.5)$$

The initial integration to obtain $Q(t)$ tends to smooth the data and no preliminary noise reduction is generally required.

Fig. 2.5 shows the traces of surface temperature history, cumulative heat input, and heat transfer rate of four thermocouples for shot 471, using Eq. (2.1), Eq. (2.4), and Eq. (2.5). The heat flux of each thermocouple was computed by taking the average at a certain time over a certain time width.
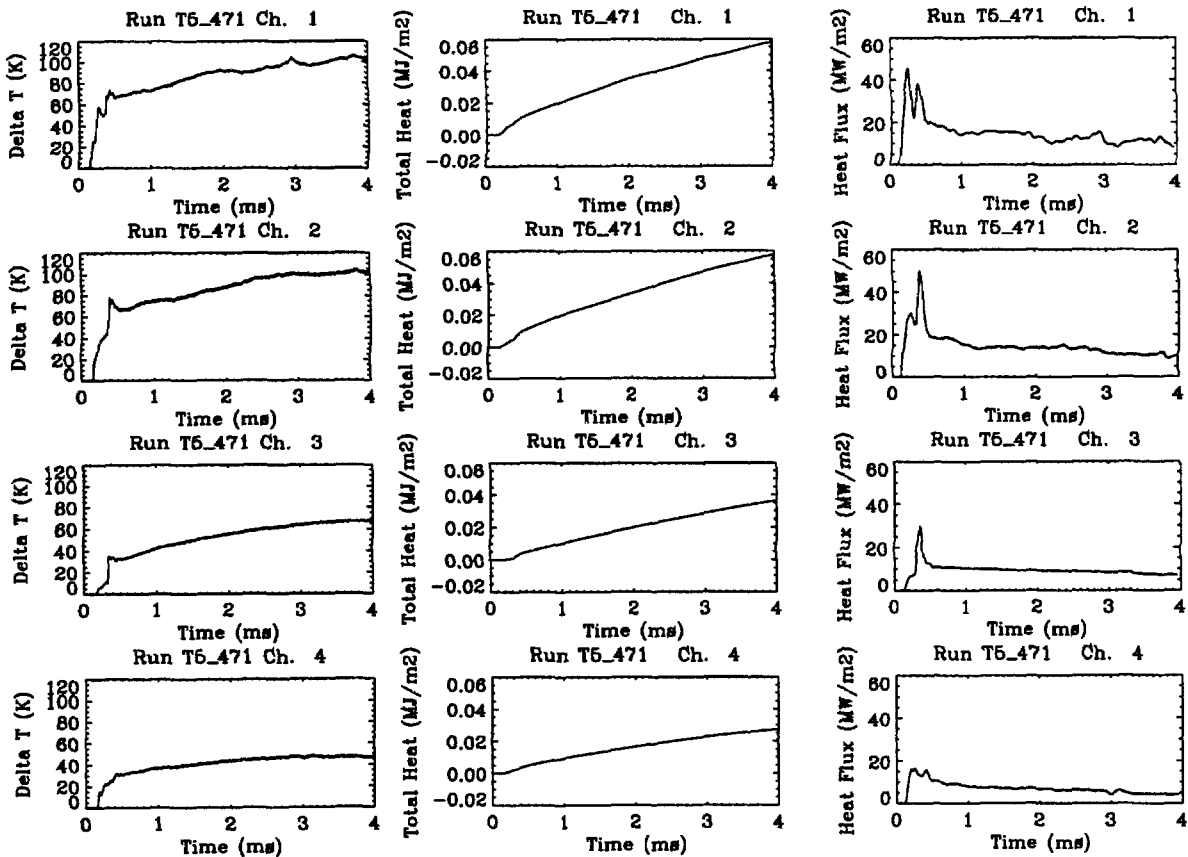
FIG. 2.5. Time traces of surface temperature history, cumulative heat input, and heat transfer rate of four thermocouples for shot 471, using Eq. (2.1), Eq. (2.4), and Eq. (2.5). The average of heat transfer rate was taken between $t = 1.0$ ms and $t = 1.5$ ms.

2.5 Flow Visualization

Two flow visualization techniques were used for the experiments. Finite-fringe differential interferometry using a Wollaston prism with a divergence angle of 2' 15" was used throughout most of the experiments. The optical system has an 8 in. field of view, which is the same as the diameter of spherical mirrors and optical windows, and is a typical Z shape single pass system with one optical table on each side of the test section. The Wollaston prism and the spherical mirrors with a focal length of 10 ft. (3.049 m) produce correspondingly a double image of a maximum displacement of approximately 2 mm. The light source used for the differential interferometry was an injection-seeded, frequency-doubled, neodymium-YAG laser for the first 25 shots and a tunable dye laser pumped by the neodymium-YAG laser for the remaining shots. The neodymium-YAG laser produces pulses at 532 nm wavelength with about 5 mJ pulse energy and 6 ns pulse width. The wavelength of the dye laser is about 589 nm with a bandwidth of 3 GHz. Fig. 2.6 shows the schematic of the optical system. Examples of differential interferograms of the hypervelocity flow over a sphere are shown in chapter 4.

In the last five shots, resonantly-enhanced shadowgraphy with sodium seeding was used with the original aim to see the boundary layer structure along the wall of the model. This technique relies on the fact that the refractive index of a gas goes through a maximum very close to a spectral line of the medium. The value of the refractive index at this maximum is considerably above the broad-band value. The flow was then seeded by painting a very thin layer of a saturated saline solution in a small spot at the nose of the sphere. This was left to dry, so that a thin film of salt was left to be ablated during the test. The light source used was the tunable dye laser mentioned above with wavelength tuned at about 589 nm and just off the center of one of the sodium D-lines. Note that only 100 parts per billion of sodium would have to be present in the flow to get good sensitivity. Even if the wavelength is not perfectly tuned, such that it is in the center of one of the D-lines where the refractive index contribution of the line is zero, the absorption of the light by the resonance is very high, and the technique will still function satisfactorily. The optical system was the same as that shown in Fig. 2.6 except with the Wollaston prism and two polarizers removed. For

Print Film   Neutral Density Filter   Wollaston Prism

Shutter

Bandpass Filter

Polarizers

Digital Delay
Generator
(Camera Shutter
and Laser Firing
Control Unit)

DAS

Windows

Model

Nd:YAG	Tunable
Laser	Dye Laser
532 nm	589.6 nm

Test Section
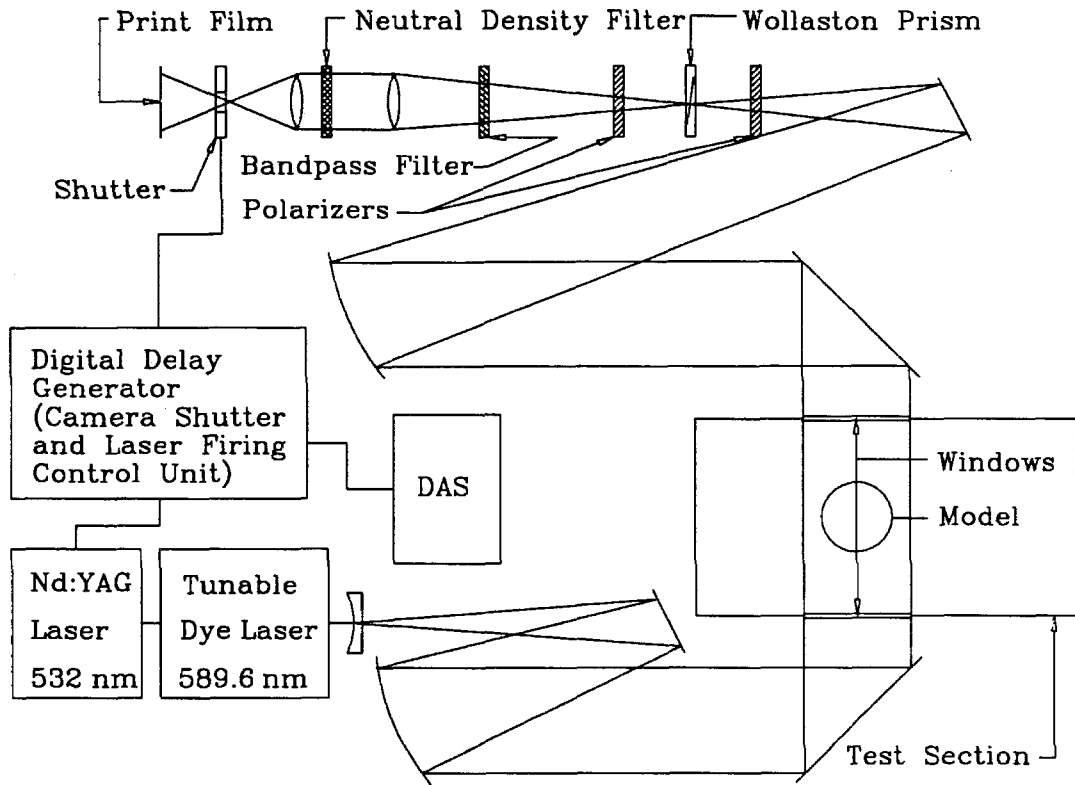
FIG. 2.6. Schematic diagram of the optical arrangement. The neutral density filter is used to get rid of the luminosity emitted from the test gas. The bandwidth of the band-pass filter is 10 nm centered at 590 nm for the dye laser and 10 nm centered at 532 nm for the neodymium-YAG laser. The dye solution used in the dye-laser is Rhodamine 6G (610 nm) diluted in methanol.

more information about the resonantly-enhanced technique see *e.g.* Blenstrup *et al.* (1979) and Germain *et al.* (1993). An example of the resonantly-enhanced shadowgraph will be presented in chapter 7.

The pictures were taken at the time when the flow was steady and not yet contaminated by the driver gas, which is typically 1.5 ms for the lower and medium enthalpy shots ($h_0 \leq$ 15 MJ/kg) and 1.0 ms for the high enthalpy shots ($h_0 > 15$ MJ/kg), after the arrival of the shock at the end of the shock tube. The laser was triggered by the programmable digital delay generator (Camera shutter and laser firing control unit) in Fig. 2.2 and Fig. 2.6. Kodak TMAX (ASA 400, 4 in. × 5 in.) film, developed normally, was used for all the photographs.

CHAPTER 3

Computational Method

The difficulties associated with the experimental investigation of hypervelocity flow over spheres made application of numerical simulation an attractive complement to the experimental effort. In this chapter, the numerical code used to compute the hypervelocity dissociating flow over the front part of a sphere or a circular cylinder is described. The code was provided by Candler and was used extensively in the current study. The methodology for the computational interferometry and the particle-tracing technique, developed as part of this thesis work, will also be addressed. The computational interferogram generated from the computational flow field can provide a useful visualization tool for the validation of the numerical code and the particle-tracing technique can extract all the flow information along a specific streamline. These computations were used to enhance the understanding provided by the experimental data and theoretical derivations.

3.1 Description of Candler's Code

Candler's (1988) code was used to construct the inviscid reacting flow over a sphere. The flow field is described by coupled partial differential equations for the conservation of species, mass, mass-averaged momentum, vibrational energy of each diatomic species and total energy. A finite-volume method using modified Steger-Warming flux-vector splitting is used to obtain the steady-state solution to these fully coupled equations for different gases. Park's semi-empirical two-temperature model and chemical kinetics model (Park, 1988, 1989) were used to calculate the reaction rates for different reactions. The scheme is implicit, using Gauss-Seidel line relaxation, and is second-order accurate in the tangential direction. The code is also set up for viscous flow. The inviscid code was used to obtain the conditions at the edge of the boundary layer for the theoretical heat flux predictions and

to construct the computational differential interferograms for comparsion with the experimental pictures. Extensive documentation of successful examples exists in reproducing in great detail those experimental results, see *e.g.*, Candler (1988), Rock *et al.* (1992), Wen and Hornung (1993), and Hornung *et al.* (1994). Since the shock values of temperature, vibrational temperatures, and density are not accessible during the experiment, the computational method provides a good way to obtain partial information about them. The flow field computations were performed using a CRAY Y-MP2 at the Jet Propulsion Laboratory (JPL), Pasadena, CA. It took 0.11 to 0.20 millisecond of CPU per grid per iteration on the CRAY Y-MP2 and 1000 to 2000 iterations were required for each case.

3.1.1 Governing Equations and the Numerical Method

The equations that describe the thermo-chemical nonequilibrium flow over a sphere will be summarized below. No ionization is considered for the present work, although the code is capable of implementing it. With a multicomponent gas that is characterized by a translational-rotational temperature and a common vibrational temperature for all the diatomic species, we must solve the following equations:

a mass conservation equation for each species,

$$\frac{\partial \rho_s}{\partial t} + \frac{\partial}{\partial x_j}(\rho_s u_j) = -\frac{\partial}{\partial x_j}(\rho_s v_{sj}) + w_s \ ; \tag{3.1}$$

a mass-averaged momentum equation,

$$\frac{\partial}{\partial t}(\rho u_i) + \frac{\partial}{\partial x_j}(\rho u_i u_j + p\delta_{ij}) = -\frac{\partial \tau_{ij}}{\partial x_j} \ ; \tag{3.2}$$

a vibrational energy equation for each diatomic species,

$$\frac{\partial E_{vs}}{\partial t} + \frac{\partial}{\partial x_j}(E_{vs} u_j) = -\frac{\partial}{\partial x_j}(E_{vs} v_{sj}) - \frac{\partial q_{vsj}}{\partial x_j} + Q_{T-vs} + Q_{v-vs} + w_s e_{vs} \ ; \tag{3.3}$$

and a total energy equation,

$$\frac{\partial E}{\partial t} + \frac{\partial}{\partial x_j}[(E+p)u_j] = -\frac{\partial}{\partial x_j}(q_j + q_{vj}) - \frac{\partial}{\partial x_j}(u_i \tau_{ij}) - \frac{\partial}{\partial x_j}\sum_s v_{sj} \rho_s h_s \ . \tag{3.4}$$

Equations (3.1-3.4) can be written in two-dimensional conservation-law form

$$\frac{\partial U_1}{\partial t} + \frac{\partial U_2}{\partial x} + \frac{\partial U_3}{\partial y} = -\frac{\partial U_{2v}}{\partial x} - \frac{\partial U_{3v}}{\partial y} + W \ . \tag{3.5}$$

Once the fluxes have been split, they are upwind differenced using a modified Steger-Warming flux-vector splitting method. The governing equations are then solved using the numerical method based on MacCormack's implicit Gauss-Siedel line relaxation technique. A more detailed description of the numerical method may be found in Candler (1988).

The caloric equation of state for mass-averaged gas is derived by substracting the vibrational, kinetic, and chemical energies from the total energy to yield the energy in the translational and rotational modes. Assuming that the rotational energy modes are in equilibrium with the translational modes, the translational-rotational temperature, T, can be determined as:

$$\sum_s \rho_s c_{v_s} T = E - \frac{1}{2} \sum_s \rho_s u_i u_i - \sum_s E_{v_s} - \sum_s \rho_s h_s^0 \ . \tag{3.6}$$

The pressure is the sum of the partial pressures,

$$p = \sum_s \rho_s \frac{R}{M_s} T \ . \tag{3.7}$$

The shear stress tensor and heat conduction vectors are given by

$$\tau_{ij} = -\mu \left(\frac{\partial u_i}{\partial x_j} + \frac{\partial u_j}{\partial x_i} \right) + \frac{2}{3} \mu \frac{\partial u_k}{\partial x_k} \delta_{ij} \ , \tag{3.8}$$

$$q_j = -k \frac{\partial T}{\partial x_j} \ , \qquad q_{vsj} = -k_{vs} \frac{\partial e_{vs}}{\partial x_j} \ , \tag{3.9}$$

The conduction of vibrational energy is treated in this fashion because of the nonlinear variation of vibrational temperature with energy (Vincenti and Kruger, 1965).

A viscosity model for reacting gases developed by Blottner et al. (1971) is used to determine species viscosity. The conductivities of the translational-rotational temperature and vibrational energy for each species are given by

$$k_s = \mu_s \left(\frac{5}{2} c_{vtrans_s} + c_{vrot_s} \right) \ , \qquad k_{vs} = c_s \mu_s \ , \tag{3.10}$$

which are derived from an Eucken relation (Vincenti and Kruger, 1965). The total viscosity and the total conductivity of the gas mixture are then calculated using Wilke's semi-empirical mixing rule (Wilke, 1950).

The diffusion velocities of all components of the gas mixture are assumed to be proportional to the gradients of the mass fractions

$$\rho_s v_{sj} = -\rho D_s \frac{\partial c_s}{\partial x_j} \; . \tag{3.11}$$

The expression for the species diffusion coefficients is obtained by assuming a constant Lewis number ($L_e = 1.4$).

3.1.2 Energy Exchange Mechanisms

The energy exchange mechanisms that appear on the right side of Eqs. (3.3) will be outlined below.

The rates of energy exchange between the translational and vibrational energy modes Q_{T-v_s} are assumed to be of the Landau-Teller form,

$$Q_{T-v_s} = \rho_s \frac{e_{v_s}^*(T) - e_{v_s}}{<\tau_s>} \; . \tag{3.12}$$

An expression developed by Lee (1985) yields the Landau-Teller relaxation time, $< \tau_s >$.

In a mixture of diatomic gases that have been thermally excited, as one species becomes excited it tends to transfer its vibrational energy to other species in vibration-vibration ($v-v$) energy exchanges. The rate of vibrational energy transfer from species r to s is the product of the probability of a $v-v$ exchange, the number of collisions, and the change in the energy during the collision. This may be written as

$$Q_{v-v_{sr}} = P_{sr} \cdot Z_{sr} \cdot \Delta \varepsilon_{v_{sr}} \; , \tag{3.13}$$

where $\Delta \varepsilon_{v_{sr}}$ is the change in the s particle vibrational energy due to the $v-v$ energy transfer.

Assume that after the collision, the two collision partners have the same vibrational temperature, T'_{vsr}. Thus, balancing the energy before and after the collision yields

$$\varepsilon_{vs}(T_v) + \varepsilon_{vr}(T_v) = \varepsilon_{vs}(T'_{vsr}) + \varepsilon_{vr}(T'_{vsr}) \ . \tag{3.14}$$

From this expression, T'_{vsr} can be solved using the definition of the vibrational energy per particle for a simple harmonic oscillator

$$\varepsilon_{vs}(T_v) = \frac{R}{\hat{N}} \frac{\theta_{vs}}{e^{\theta_{vs}/T_v} - 1} = \frac{M_s}{\hat{N}} e_{vs}(T_v) \ . \tag{3.15}$$

Thus, the change in the s particle vibrational energy due to a collision with r is

$$\Delta\varepsilon_{vsr} = \varepsilon_{vs}(T'_{vsr}) - \varepsilon_{vs} \ . \tag{3.16}$$

And, therefore, for n species, the $v - v$ energy transfer rate is

$$Q_{v-vs} = \sum_{r \neq s}^{n} Q_{v-vsr} = \sum_{r \neq s}^{n} P_{sr} \cdot Z_{sr} \cdot \frac{M_s}{\hat{N}} [e_{vs}(T'_{vsr}) - e_{vs}] \ . \tag{3.17}$$

Z_{sr} is determined from kinetic theory (see Vincenti and Kruger, 1965), and the probabilities of vibrational energy exchange during a collision have been measured for several molecules experimentally (see Taylor et al., 1967). For temperatures of interest (above 2000 K), P_{sr} is typically of the order of 0.01, and for this work, it has been assumed to be constant at that value.

3.1.3 Vibrational Energy Model for CO_2

Carbon dioxide has three vibrational modes, one of which is doubly degenerate. Again, a simple harmonic oscillator is employed to describe the vibrational potential of each vibrational mode of the molecules. With the same assumption as above, that there is a unique vibrational temperature at each point in the flowfield, the vibrational energy per unit mass of CO_2 is given by

$$e_{vCO_2} = e_{vCO_2,1} + e_{vCO_2,2} + e_{vCO_2,3} \ , \tag{3.18}$$

where

$$e_{vCO_2,r} = g_r \frac{R}{M_s} \frac{\theta_{vCO_2,r}}{e^{\theta_{vCO_2,r}/T_v} - 1} \ . \tag{3.19}$$

The values of $\theta_{v_{CO_2},r}$ and g_r for CO_2 are listed in Table 3.1.

$\theta_{v_{CO_2},r}$ K	g_r
1903	1
945	2
3329	1

Table 3.1 Vibrational energy constants of CO_2

The total vibrational energy of the CO_2 mixture is the sum of the individual vibrational energies of the molecular species, and the energy exchange mechanisms for the dissociating CO_2 flows are modelled with the same methods as the mixture of diatomic gases mentioned above.

3.1.4 Chemical Source Terms

The chemical reaction considered for nitrogen flow is

$$N_2 + M \; \rightleftharpoons \; 2N + M \; . \tag{3.20}$$

For flows not involving ionization, there are five primary chemical species, N_2, O_2, NO, N, and O for air flows and CO_2, CO, O_2, C, and O for carbon dioxide flows. The primary chemical reactions between the five species considered in this work are

$$\begin{aligned}
N_2 + M &\; \rightleftharpoons \; 2N + M \\
O_2 + M &\; \rightleftharpoons \; 2O + M \\
NO + M &\; \rightleftharpoons \; N + O + M \\
N_2 + O &\; \rightleftharpoons \; NO + N \\
NO + O &\; \rightleftharpoons \; O_2 + N \; ,
\end{aligned} \tag{3.21}$$

for air, and

$$CO_2 + M \rightleftharpoons CO + O + M$$

$$CO + M \rightleftharpoons C + O + M$$

$$O_2 + M \rightleftharpoons 2O + M \tag{3.22}$$

$$CO_2 + O \rightleftharpoons O_2 + CO$$

$$CO + O \rightleftharpoons O_2 + C ,$$
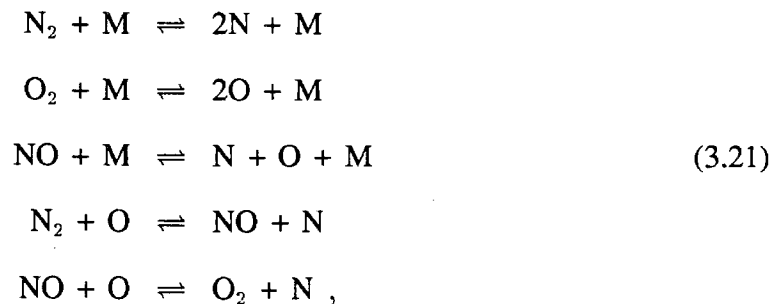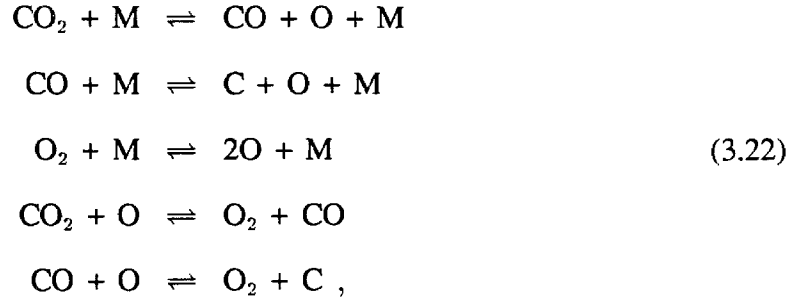
for carbon dioxide.

The reaction rate constants for these reactions were taken from Park (1985) for nitrogen and air, and from Park *et al.*(1991) for carbon dioxide. Note that, in Park's two-temperature chemical kinetic model (Park, 1988, 1989), the forward reaction rate will be a function of the vibrational excitation of the diatomic molecule or carbon dioxide and the translational temperature of the impacting particle in the first three reactions of air and carbon dioxide. Thus, using the arguments of Park, an average temperature, T_{ave}, defined as

$$T_{ave} = \sqrt{TT_v} \; , \tag{3.23}$$

will determine these reaction rates. The backward reaction rates will depend only on the translational temperature, T.

3.1.5 Boundary Conditions

Uniform supersonic freestream conditions are assumed. The outflow is also supersonic, and therefore, a zero-gradient exit condition is appropriate. In viscous computation, a no-slip velocity condition is applied, while in the inviscid case, the velocity is free-slip at the wall. The other wall boundary conditions are specified by assuming a fixed-wall temperature, a zero normal pressure gradient, and a noncatalytic wall, which implies that the normal gradient of each species mass fraction is zero at the wall.

3.1.6 Computation Grid

Throughout the present work, the computations were performed on body-fitted meshes with 56 points axially along the sphere and 100 points in the flowfield normal to the body. An exponentially expanding mesh in the wall-normal direction was used. For viscous flow computations, a fine mesh spacing near the wall is necessary to reproduce the boundary layer profile which determines the accuracy of the heat flux computations. However, refining the mesh near the wall while keeping the number of cells fixed yields a coarser mesh spacing away from the wall. This implies that the resolution near the shock region becomes worse. Therefore, different meshes were used for the viscous computation and inviscid computation. The mesh fineness is expressed by the minimum cell size in y-direction, dy_{min}, which is represented by the fraction of the nose radius, a. A mesh with dy_{min} equal to $a/10000$ was used for viscous computations to get good resolution in the boundary layer and a mesh with dy_{min} equal to $a/600$ was used for inviscid computations to get good resolution near the shock region. These meshes are shown in Fig. 3.1 and Fig. 3.2 for the viscous and inviscid case, respectively.

3.2 Computational Interferometry

3.2.1 Computation of Mach-Zehnder Interferograms

A Mach-Zehnder interferometer is an optical device that makes possible the visualization of density fields in a flow. The Mach-Zehnder interferograms are created by recording the intensity of two superposed beams: the reference beam and the object beam. The reference beam does not pass through the flowfield and its phase is not changed. The object beam does pass through the flowfield, and its phase is changed by the density variations. When the object beam interferes with the reference beam, under the assumption that the conditions of optical coherence are fulfilled, the two constructively and destructively combine to form a manifest series of dark and light fringes.
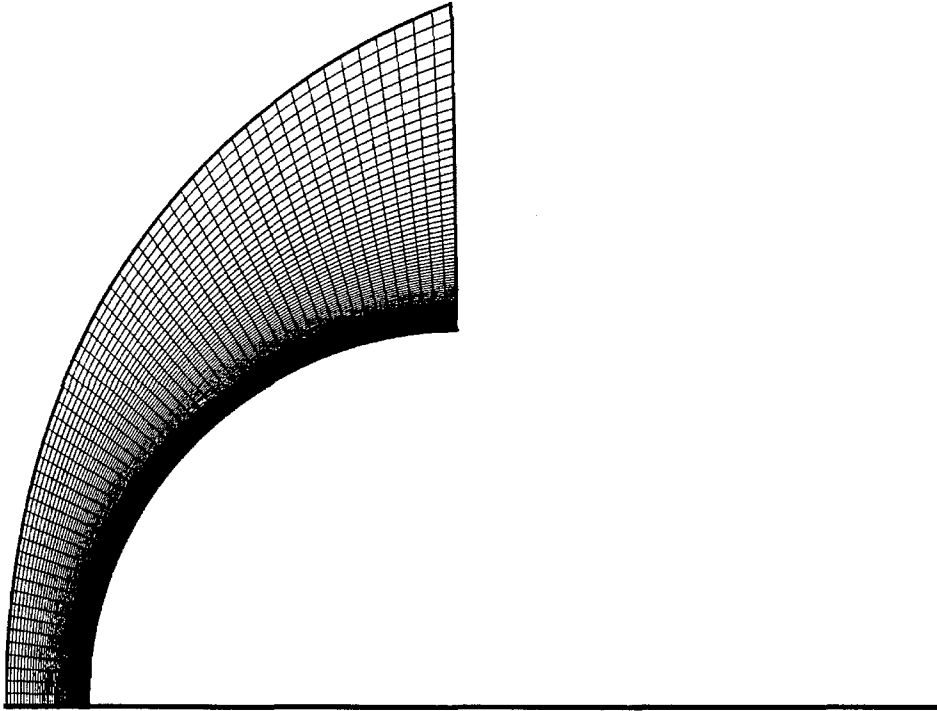
FIG. 3.1. 56 × 100 grid used for viscous computations.

When calculating Mach-Zehnder interferograms from computed flowfields, the phase shift of the object beam relative to the reference beam was obtained by integrating the following equation along a line of sight:

$$\phi_{opt} = \frac{2\pi}{\lambda} \int_0^z (n - n_0) dl \ . \tag{3.24}$$

For equilibrium or nonequilibrium reacting gases, the refractive index is given by Merzkirch (1987)

$$n = 1 + \sum_i K_i \rho_i \ . \tag{3.25}$$

The values of Gladstone-Dale constants are listed in Table 3.2.

The integration of Eq. (3.24) is performed along the optical path length of the light
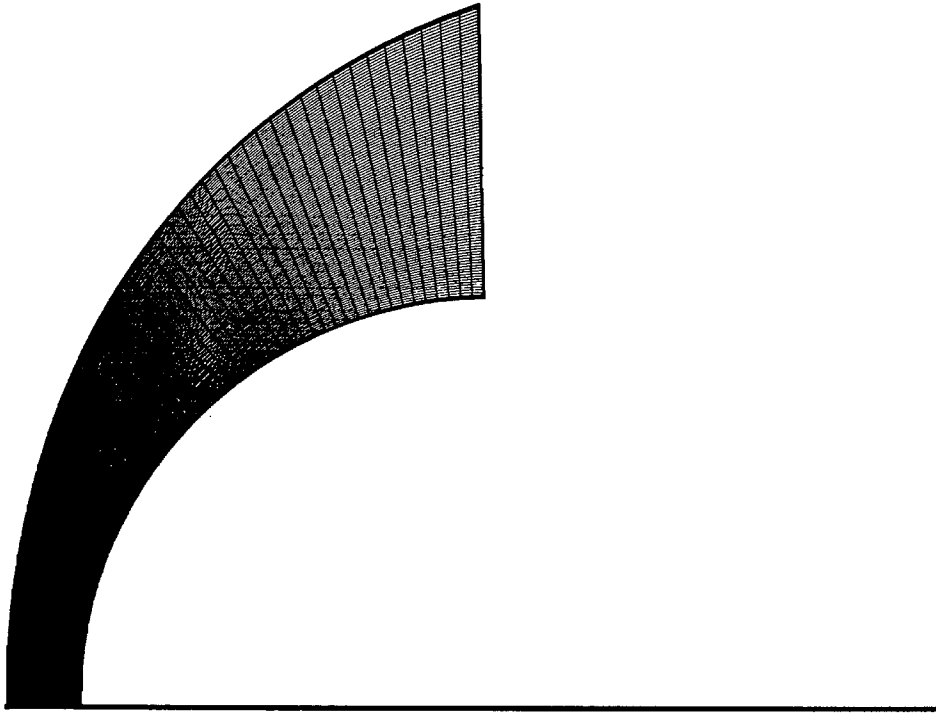
FIG. 3.2. 56 × 100 grid used for inviscid computations.

source passing through the flow. By using the approximation that the light's path is a straight line perpendicular to the image plane, it is possible to construct interferograms without ray tracing. Tracing the actual light path as it bends through the flowfield solution and integrating the appropriate function of the refractive index along this path is computationally expensive. Yates (1992) has shown that for regions of the flow without shocks, this approximation should have a minimal effect on the constructed images, and in shock regions where the refractive index will change rapidly, the approximation may introduce errors. However, Yates concluded that these errors are in many cases on the order of, or smaller than, the solution and experimental errors. Straight line approximation also implies that the diffraction around the object can be neglected.

species	$K_i \times 10^{-3}$ m^3/kg
N_2	0.238
O_2	0.19
NO	0.221
N	0.31
O	0.182
CO_2	0.230
CO	0.270
C	0.404

Table 3.2 Gladstone-Dale constants for use in Eq. (3.25). Values from Merzkirch (1987), Alpher and White (1959), and Kaye and Laby (1986).

Because Candler's code gives only the solution on one of the axisymmetric planes, the axisymmetric flowfield is obtained by rotating the computational grid 90 degrees around the x-axis. The computational grid for the inviscid flows and the coordinate system are shown in Fig. 3.3. The $x - y$ plane is the image plane and the light path direction coincides with the z direction. A beam starts from a grid point in the $x - y$ plane with dz as the marching length in the physical domain.

Since the flow solution is obtained on a curvilinear coordinate system, a line of sight calculation must be performed to evaluate the integration in Eq. (3.24). This calculation is achieved by transforming the physical space into a computational space, $(x, y, z) \rightarrow (\xi, \eta, \zeta)$. The line of sight calculation can then be performed in the computational space in an efficient manner. The straight line assumption requires that x and y remain constant ($dx=0$ and $dy=0$), while $z(dz)$ is allowed to vary. x_ζ is also equal to zero. These conditions lead to the following set of equations that govern the integral calculation.

$$d\xi = \frac{x_\eta y_\zeta}{J} dz$$

$$d\eta = -\frac{x_\xi y_\zeta}{J} dz \qquad (3.26)$$

$$d\zeta = \frac{(x_\xi y_\eta - x_\eta y_\xi)}{J} dz \ ,$$

where

$$J = \det \begin{vmatrix} x_\xi & x_\eta & x_\zeta \\ y_\xi & y_\eta & y_\zeta \\ z_\xi & z_\eta & z_\zeta \end{vmatrix} \ . \qquad (3.27)$$

The new starting point will be located at $(\xi + d\xi, \eta + d\eta, \zeta + d\zeta)$. Let int(x) be a function so that int(x) gives the largest integer which is not larger than x. The density at the new starting point during the integration was then obtained by first order linear interpolation about the grid point (int$(\xi + d\xi)$, int$(\eta + d\eta)$, int$(\zeta + d\zeta)$) and the line integration of Eq. (3.24) was done by the trapezoidal rule. The phase shift obtained from Eq. (3.24) was then multiplied by two because the flowfields are symmetric with respect to the $x - y$ plane.

For infinite fringe interferograms, the quantity actually recorded is the intensity of the interference of the recombined beams. The intensity, I, is related to the phase shift by

$$I \sim \cos^2(\phi_{opt}/2) \ . \qquad (3.28)$$

Contours of I then give a computational Mach-Zehnder interferogram.

For finite fringe interferograms, a linearly-varying phase is added to Eq. (3.24):

$$\phi_{opt,linear} = k_x x + k_y y \ , \qquad (3.29)$$

and the spacing and orientation of the freestream fringes are determined by k_x and k_y, which can be measured from the experimental interferograms. Examples of computational Mach-Zehnder interferograms will be shown in chapter 4. The generation of computational Mach-Zehnder interferogram took about 3 hours of CPU time on a Sun SPARCstation computer and about 30 seconds of CPU on the CRAY Y-MP2.
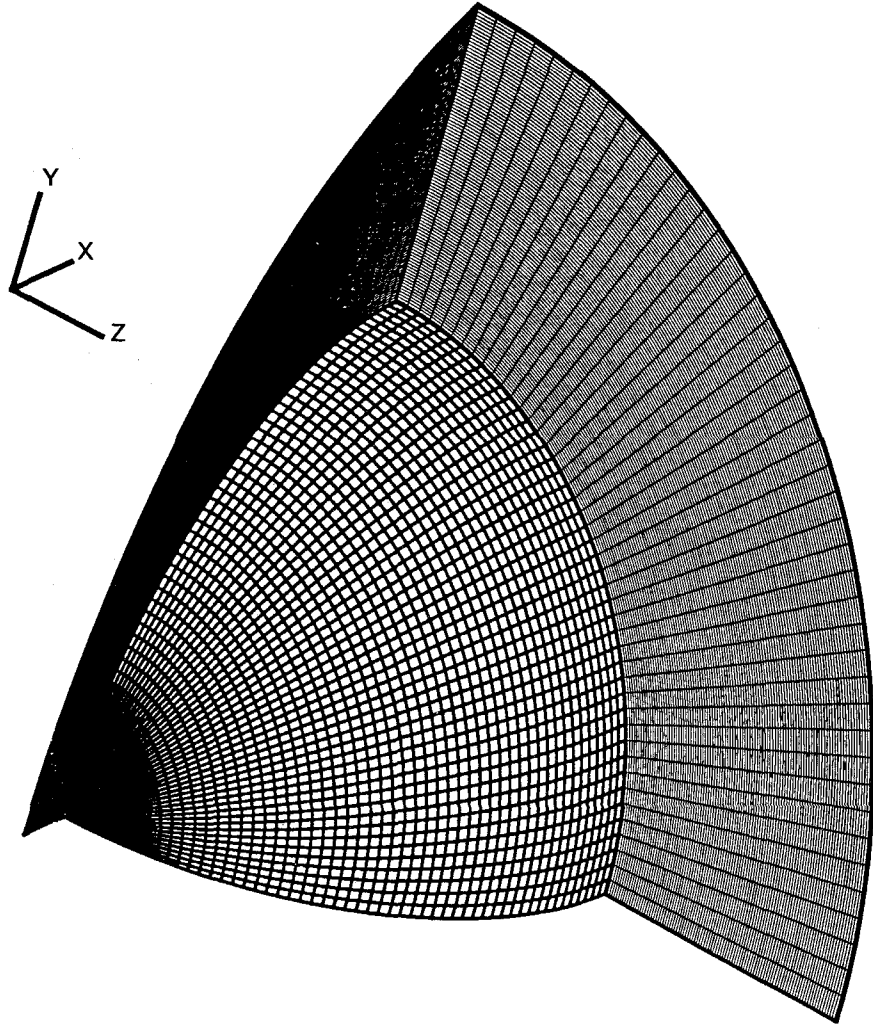
FIG. 3.3. Grid used for computations of inviscid Mach-Zehnder interferograms.

3.2.2 Computation of Differential Interferograms

Differential interferometry measures gradient of optical path length. In contrast to the Mach-Zehnder interferometry, the signal obtained with a differential interferometer is caused by the interference of two light rays passing through the test flow. Two parallel, laterally displaced light rays passing through the flow at positions $(x + dx/2, y + dy/2)$ and

$(x - dx/2, y - dy/2)$ on the image plane are considered. The shearing element, Wollaston prism, positioned in or near the focal point provides that components of the two rays coincide after they have passed through this element. Assuming the two coinciding rays are optically coherent, they can interfere with each other. If the refractive indices, n, of two rays are not equal, they will exhibit a difference in their optical phases, $\delta\phi_{opt}$, given by

$$
\begin{aligned}
\delta\phi_{opt}(x, y) &= \frac{2\pi}{\lambda} \int_0^z n(x + \frac{dx}{2}, y + \frac{dy}{2}, z)dz - \frac{2\pi}{\lambda} \int_0^z n(x - \frac{dx}{2}, y - \frac{dy}{2}, z)dz \\
&= \phi_{opt}(x + \frac{dx}{2}, y + \frac{dy}{2}) - \phi_{opt}(x - \frac{dx}{2}, y - \frac{dy}{2}) ,
\end{aligned}
\tag{3.30a}
$$

or

$$
\begin{aligned}
\delta\phi_{opt}(x, y) &= \frac{2\pi}{\lambda} \int_0^z n(x - \frac{dx}{2}, y - \frac{dy}{2}, z)dz - \frac{2\pi}{\lambda} \int_0^z n(x + \frac{dx}{2}, y + \frac{dy}{2}, z)dz \\
&= \phi_{opt}(x - \frac{dx}{2}, y - \frac{dy}{2}) - \phi_{opt}(x + \frac{dx}{2}, y + \frac{dy}{2}) .
\end{aligned}
\tag{3.30b}
$$

The sign difference in Eq. (3.30a) and Eq. (3.30b) corresponds to the orientation of the Wollaston prism used in the experimental differential interferometry. This sign determines the direction of the fringe shift. The quantity $\delta\phi_{opt}(x, y)$ is measured in the recording plane in the form of interference fringes and is related to the intensity, I, as in Eq. (3.28).

Eq. (3.30) is derived under two assumptions. First, the path lengths of two light rays through the flow are equal. Second and more important, the propagation of light in the flow is straight and undeflected, *i.e.*, the straight line assumption for computational Mach-Zehnder interferometry.

The edges of rigid bodies, which are normal to the direction of shear, appear as a double image or gray zone of width $d = \sqrt{(dx)^2 + (dy)^2}$ (or $d\cos\theta$, where θ is the angle between the direction of shear and the normal to the wall). The formation of this double image is due to the blocking of one of the two conjugate rays by the wall. The exact position of the wall edge is in the middle of the gray zone. The boundary layer will be partially or totally embedded in the double image.

The direction of shear and the maximum size of the double image d can be measured from the experimental interferogram. The direction of shear d is perpendicular to the direction of freestream fringes, or parallel to the wall-normal direction of the point with the maximum size of the double image.

Using the integrated optical phase, ϕ_{opt}, of each grid point on the image plane from a computational Mach-Zehnder interferogram, a computational differential interferogram can be obtained using Eq. (3.30). For instance, consider a light beam passing through the flow at the grid point $X(\xi, \eta)$ on the image plane. The optical system is set up so that the light beam will interfere with a light beam passing through the flow at point X' with the coordinate $(x+dx, y+dy)$ in the physical domain. Here, dx and dy are the shear components in the x and y direction. $dx = d \cdot \cos \theta$, $dy = d \cdot \sin \theta$ and θ is the direction of the shear. Jacobian matrices are used to transform the physical space into the computaional space. The transformation equations are as follows:

$$d\xi = \frac{y_\eta dx - x_\eta dy}{J}$$
$$d\eta = \frac{x_\xi dy - y_\xi dx}{J} \tag{3.31}$$

and

$$J = \det \begin{vmatrix} x_\xi & x_\eta \\ y_\xi & y_\eta \end{vmatrix} .$$

The coordinate of point X' in the computational domain is $(\xi+d\xi, \eta+d\eta)$. The integrated optical phase at point X' can then be obtained by first order linear interpolation about the grid point $(\text{int}(\xi + d\xi), \text{int}(\eta + d\eta))$. Subtracting the value of the integrated optical phase at point X' from that of point X and taking the intensity of this phase difference yields the signal at the midpoint of point X and X'. If point X' falls inside the wall, its optical phase will be set to zero. No interference will occur in this case and these single-ray signals provide the double image for the computational differential interferogram. Contours of intensity I of $\delta\phi_{opt}$ then give a computational differential interferogram. Examples of computational differential interferograms and comparsion with experimental ones will be shown in chapter

4. The computational differential interferogram could be generated from the computational Mach-Zehnder interferogram within a minute by a Sun SPARCstation computer.

3.3 Particle-Tracing Technique

The concept of streamlines in a steady flow provides a means by which solutions to the governing equations may be interpreted physically. Hence, it is important to be able to follow a streamline and gather all the physical information along the streamline from a computational flowfield. In steady flow, streamlines, particle paths, and streaklines are all identical. A particle is instantaneously moving along a streamline; if that streamline is unchanged at a slightly later time, the particle will continue to move along it, and so the particle path coincides with the streamline. In order to establish the equations of the pathlines in a given flowfield, consider an axisymmetric or a two-dimensional flowfield in which the velocity has components u and v in the x and y directions, respectively. Then, by virtue of the definition of a pathline, the equations of the pathline are

$$\frac{dx}{dt} = u \; , \quad \frac{du}{dt} = v \; . \tag{3.32}$$

Using Candler's code, one can get velocity, density, temperature, pressure, reaction rates, ... *etc.* at each grid point on an axisymmetric or a two-dimensional plane. If a given fluid particle is released at grid point (ξ, η) at time $t = 0$, the particle under consideration will move with the fluid at its local, known velocity.

We now proceed as in section 3.2.2 and transform the physical space into a computational space, $(x, y) \rightarrow (\xi, \eta)$. By choosing a small dt, the increments dx and dy can be obtained by Eq. (3.32). The Jacobian transformation equations in Eqs. (3.31) are then used to find the next starting point $(\xi + d\xi, \eta + d\eta)$ in the computational space. All the physical parameters of interest can be found by taking the first order linear interpolation about the grid point (int($\xi + d\xi$), int($\eta + d\eta$)), for example, the physical coordinate (x, y), velocity, density, reaction rates, ... *etc.*. The same procedures are followed until the particle reaches

beyond the computational space. Fig. 3.4 shows the density and temperature variation along two selected streamlines. More examples will be shown in chapter 6. The particle-tracing calculation can be done within a few senconds by a Sun SPARCstation computer.
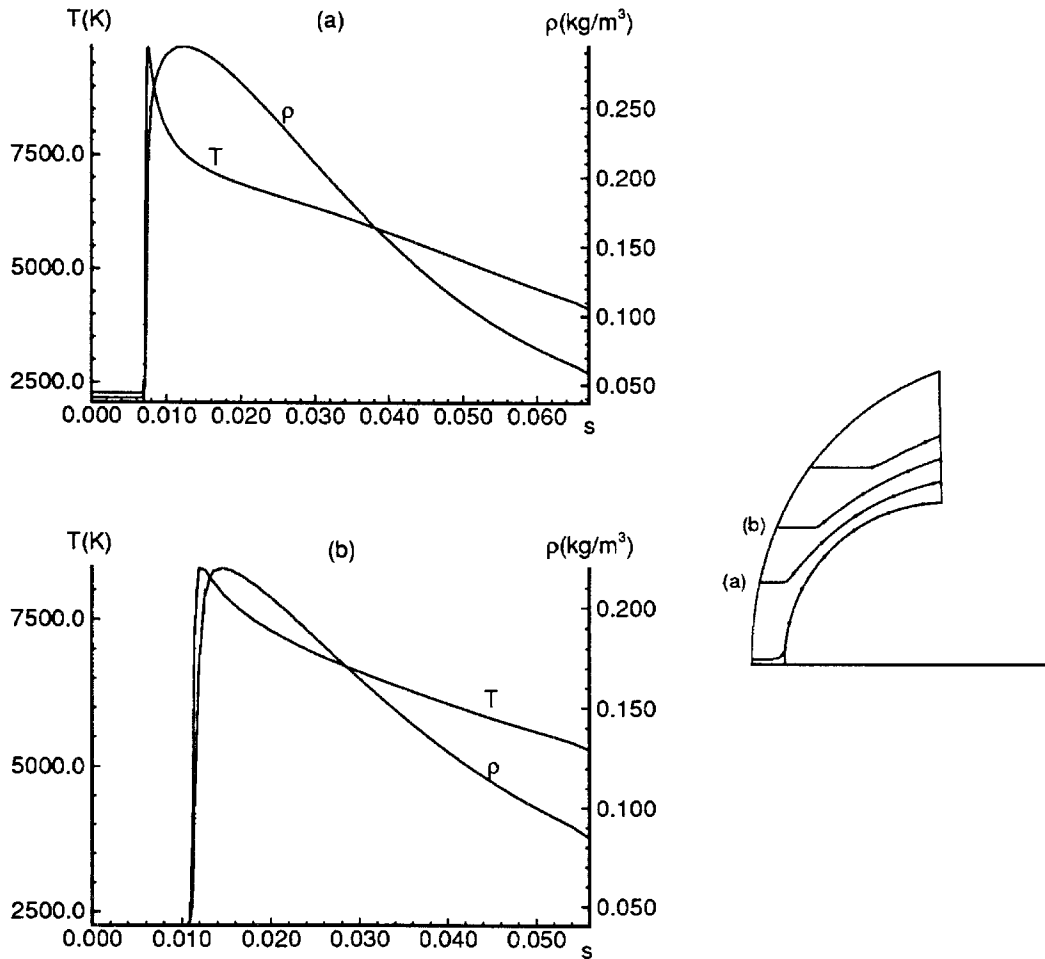
FIG. 3.4. Density and temperature variation along two selected streamlines. The streamlines are labelled a and b in the diagram on the right. The kink in the streamline indicates the shock location. Freestream conditions: nitrogen flow over a sphere of D=4 in., 5.07 km/s, 0.04 kg/m^3, 2260 K, 16.46 MJ/kg.

CHAPTER 4

Results of Heat Transfer Rate Measurements and Flow Visualization

This chapter presents the experimental results of measurements of the heat transfer rates experienced by spherical models of 1, 2, 3, 4, and 6 inch diameter in nitrogen, air, and carbon dioxide at stagnation enthalpies ranging from 4 to 22 MJ/kg and stagnation pressures from 30 to 90 MPa. These experimental results are compared with theoretical predictions and with numerical calculations. The results of heat transfer rate measurements will be discussed. The experimental pictures obtained by optical differential interferometry are compared with the images constructed from flowfields computed using the method of Candler. The comparison of the computational results with the experimental differential interferograms and heat transfer rate measurements provides a means to validate the numerical code.

4.1 Theoretical Predictions

4.1.1 Stagnation Point Heat Transfer Rate

For laminar boundary layer flow, Lees (1956) studied the heat transfer rate over blunt-nosed bodies at hypersonic flight speeds based on self-similar solutions and made a pioneering step forward in the analysis of chemically reacting viscous flow. The stagnation point heat transfer rate given by Lees for an equilibrium boundary layer is

$$\dot{q}_s = \frac{0.5 \times 2^{k/2} \, Pr^{-2/3} \, \sqrt{(\rho_e \mu_e)_s} \, \sqrt{u_\infty} h_0 \, G(Ma_\infty, \bar{\gamma}, \gamma_\infty)}{\sqrt{a}} \, , \qquad (4.1)$$

where

$$G(Ma_\infty, \bar\gamma, \gamma_\infty) = \left\{ \left(\frac{\bar\gamma - 1}{\bar\gamma} \right) \left(1 + \frac{2}{\gamma_\infty - 1} \frac{1}{Ma_\infty^2} \right) \left(1 - \frac{1}{\gamma_\infty Ma_\infty^2} \right) \right\}^{1/4} . \qquad (4.2)$$

Here $k = 0$ for a planar body and $k = 1$ for a body of revolution.

In the present work, the principle of equipartition of energy is used to estimate $\bar\gamma$ and

$$\bar\gamma = \frac{(f + 2)(1 - \alpha) + 5\alpha}{f(1 - \alpha) + 3\alpha} . \qquad (4.3)$$

The vibrational energy was assumed to be half excited, as in the case of ideal dissociating gas proposed by Lighthill (1957) and Freeman (1958). Therefore, the value of 6 was used for f in Eq. (4.3).

Fay and Riddell (1958) generalized the self-similar method of Lees and carried out the most important classic solution for the stagnation point heat transfer rate. Based on a large number of calculations covering flight velocities from 1.8 km/s to 7 km/s, altitudes from 7.6 km to 36.6 km, and wall temperatures from 300 K to 3000 K, they proposed a correlation for stagnation point heat transfer rate in dissociated air. This correlation for dissociated air is still in regular use today by industry for hypersonic vehicle analysis. For an equilibrium boundary layer (spherical nose), the correlation is

$$\dot{q}_s = 0.76 Pr^{-0.6} (\rho_e \mu_e)^{0.4} (\rho_w \mu_w)^{0.1} \sqrt{\left(\frac{du_e}{dx} \right)_s} (h_0 - h_w) \left[1 + (Le^{0.52} - 1)(\frac{h_D}{h_0}) \right] . \qquad (4.4)$$

For a frozen boundary layer with a fully catalytic wall (spherical nose), the correlation is

$$\dot{q}_s = 0.76 Pr^{-0.6} (\rho_e \mu_e)^{0.4} (\rho_w \mu_w)^{0.1} \sqrt{\left(\frac{du_e}{dx} \right)_s} (h_0 - h_w) \left[1 + (Le^{0.63} - 1)(\frac{h_D}{h_0}) \right] . \qquad (4.5)$$

And for a frozen boundary layer with a noncatalytic wall (spherical nose), the correlation is

$$\dot{q}_s = 0.76 Pr^{-0.6} (\rho_e \mu_e)^{0.4} (\rho_w \mu_w)^{0.1} (h_C - h_w) \sqrt{\left(\frac{du_e}{dx} \right)_s} . \qquad (4.6)$$

In Eqs. (4.4)-(4.6), the stagnation point velocity gradient is given by Newtonian theory as follows:

$$\left(\frac{du_e}{dx}\right)_s = \frac{1}{a}\sqrt{\frac{2(p_e - p_\infty)}{\rho_e}} \ , \tag{4.7}$$

and h_D is defined as

$$h_D = \sum_s c_s h_s^0 \ . \tag{4.8}$$

Note that Eqs. (4.4) and (4.5) are essentially the same, varying only in the slightly different exponent on the Lewis number. This demonstrates that the surface heat transfer is essentially the same whether the flow is in local chemical equilibrium or is frozen with a fully catalytic wall.

In the theoretical analysis of Fay and Riddell, the properties of a symmetric diatomic gas are implicitly contained. No theoretical effort has been made for carbon dioxide.

Sutton and Graves (1971) extended the theoretical analysis of the stagnation point heat transfer to an axisymmetric blunt body and developed a general relation for arbitrary gases and gas mixtures in chemical equilibrium. Their equation is given as

$$\dot{q}_s = K(p_s/a)^{1/2}(h_0 - h_w) \ , \tag{4.9}$$

where K can be determined by a simple technique over a wide range of gas mixtures and is equal to 0.121 kg/(s-m$^{3/2}$-atm$^{1/2}$) for carbon dioxide.

Eqs. (4.1), (4.4)-(4.6), and (4.9) can be written in dimensionless form as

$$St_s = \frac{k}{\sqrt{Re_\infty}} \ , \tag{4.10}$$

where

$$k = \sqrt{\frac{\rho_e \mu_e}{\rho_\infty \mu_\infty}} Pr^{-2/3} G(Ma_\infty, \bar{\gamma}, \gamma_\infty) \ , \tag{4.11}$$

for Lees's theory,

$$k = 0.76\sqrt{2} Pr^{-0.6} \frac{(\rho_e \mu_e)^{0.4}(\rho_w \mu_w)^{0.1}}{(\rho_\infty \mu_\infty)^{0.5}} \left[\frac{2(p_e - p_\infty)}{\rho_\infty u_\infty^2}\frac{\rho_\infty}{\rho_e}\right]^{1/4} \left[1 + (Le^{0.52} - 1)(\frac{h_D}{h_0})\right] \ , \tag{4.12}$$

for Fay and Riddell's equilibrium boundary layer correlation, and

$$k = K\sqrt{\frac{2p_s}{\rho_\infty u_\infty \mu_\infty}} \; .$$

(4.13)

for Sutton and Grave's method.

Stagnation point heat transfer data were then presented in the form of Stanton number and Reynolds number. The Stanton number at the stagnation point and freestream Reynolds number based on the model diameter are defined as

$$St_s = \frac{\dot{q}_s}{\rho_\infty u_\infty (h_0 - h_w)} \; ,$$

(4.14)

$$Re_\infty = \frac{\rho_\infty u_\infty D}{\mu_\infty} \; .$$

(4.15)

A viscosity model for reacting gases developed by Blottner $et\ al$ (1971) is used to determine species viscosity. The viscosity of the gas mixture is then calculated using Wilke's semi-empirical mixing rule (Wilke, 1950). In the range of the present experiments, the wall enthalpy is in fact negligible compared with the stagnation enthalpy.

Although Lees' theory and Fay and Riddell's correlation implicitly contain the real gas properties of air in the variation of $\rho\mu$ through the boundary layer, it is proposed here to use Eqs. (4.1) and (4.4) to predict the stagnation point heat transfer rate for nitrogen, but to substitute the thermodynamic and transport properties of nitrogen for those of air wherever they occur in the final formulas. Eq. (4.4) was also employed to predict the stagnation point heat transfer rate for carbon dioxide.

Candler's inviscid code was used to obtain the density, pressure, and viscosity values at the edge of boundary layer for Lees' theory and Fay and Riddell's correlation. Prandtl number 0.71 and Lewis number 1.4 were chosen for the present study.

Fig. 4.1 shows the heat transfer rate predicted by Lees' theory for each experimental condition with nitrogen or air as the test gas. The standard deviation of the heat transfer coefficient k is only 1.5 % and 2.2 % for nitrogen and air, respectively. The maximum deviation from the mean value of k is 2.8 % for nitrogen and 3.7 % for air. Therefore, k can be considered as a constant for nitrogen and air in the range of the present study.
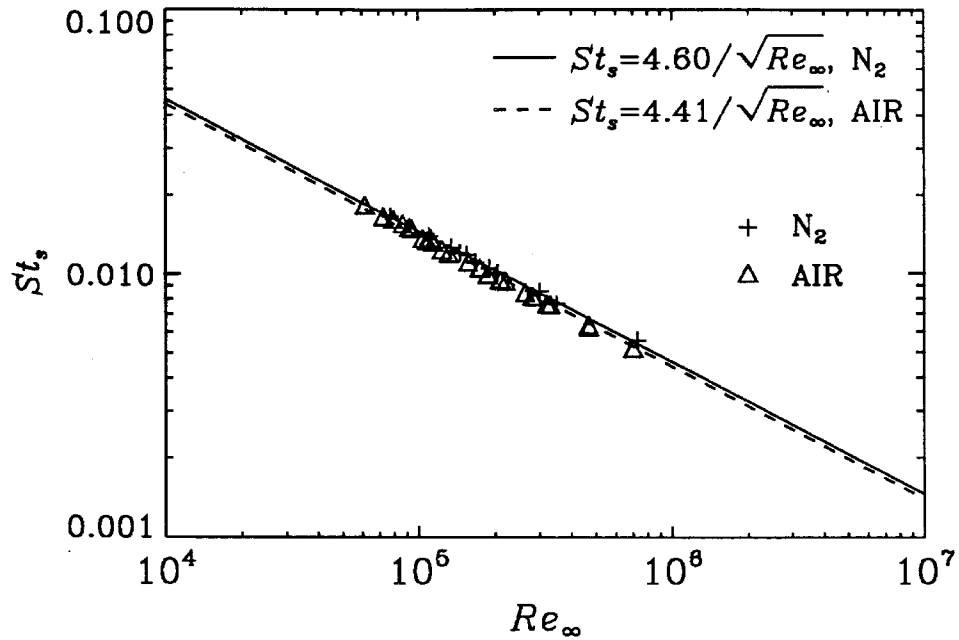
FIG. 4.1. Stagnation point heat flux in dimensionless form predicted by Lees' theory.

The predicted values of stagnation point heat transfer for each test gas using Fay and Riddell's equilibrium correlation and the predicted values of stagnation point heat transfer for carbon dioxide using Sutton and Graves' method are shown in Fig. 4.2 and Fig. 4.3, respectively. The mean value, standard deviation, and maximum deviation of k from the three different methods are summarized in Table 4.1.

	FR	FR	FR	Lees	Lees	Lees	SG	SG	SG
Gas	$\bar{k}$	$\sigma/\bar{k}$	$(\Delta k/\bar{k})_{max}$	$\bar{k}$	$\sigma/\bar{k}$	$(\Delta k/\bar{k})_{max}$	$\bar{k}$	$\sigma/\bar{k}$	$(\Delta k/\bar{k})_{max}$
N_2	4.97	1.9 %	2.3 %	4.60	1.5 %	2.8 %	–	–	–
Air	4.76	2.0 %	3.0 %	4.41	2.2 %	3.7 %	–	–	–
CO_2	3.50	6.2 %	9.7 %	–	–	–	4.08	3.8 %	7.5 %

Table 4.1 Summary of the mean value, standard deviation, and maximum deviation of k (Eq. (4.10)) from three different methods. FR: Fay and Riddell's equilibrium correlation, Eq. (4.12). Lees: Lees'theory, Eq. (4.11). SG: Sutton and Graves' correlation, Eq. (4.13).
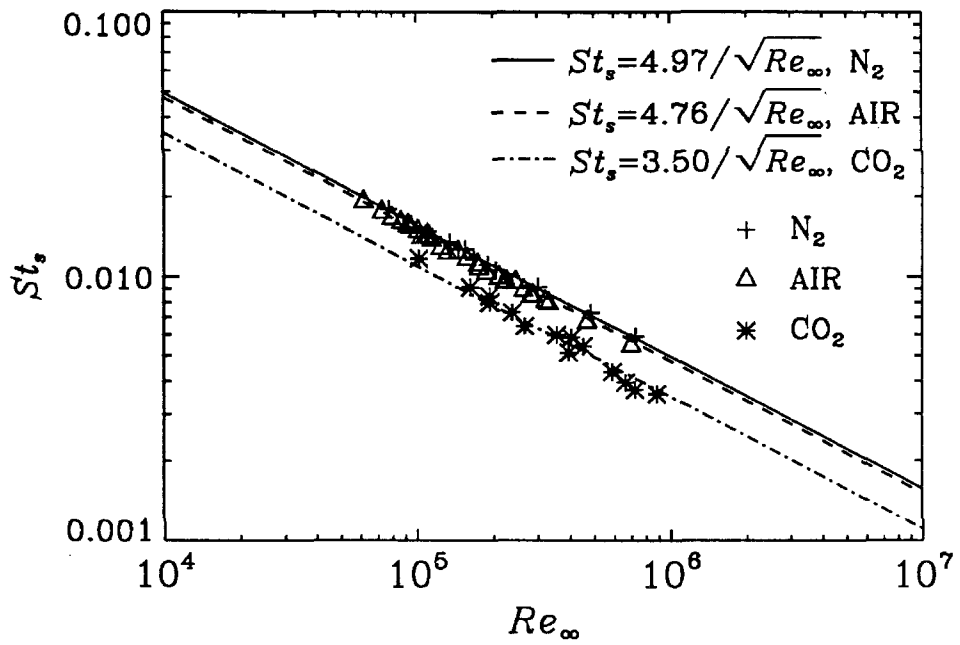
FIG. 4.2. Stagnation point heat flux in dimensionless form predicted by Fay and Riddell's equilibrium correlation.
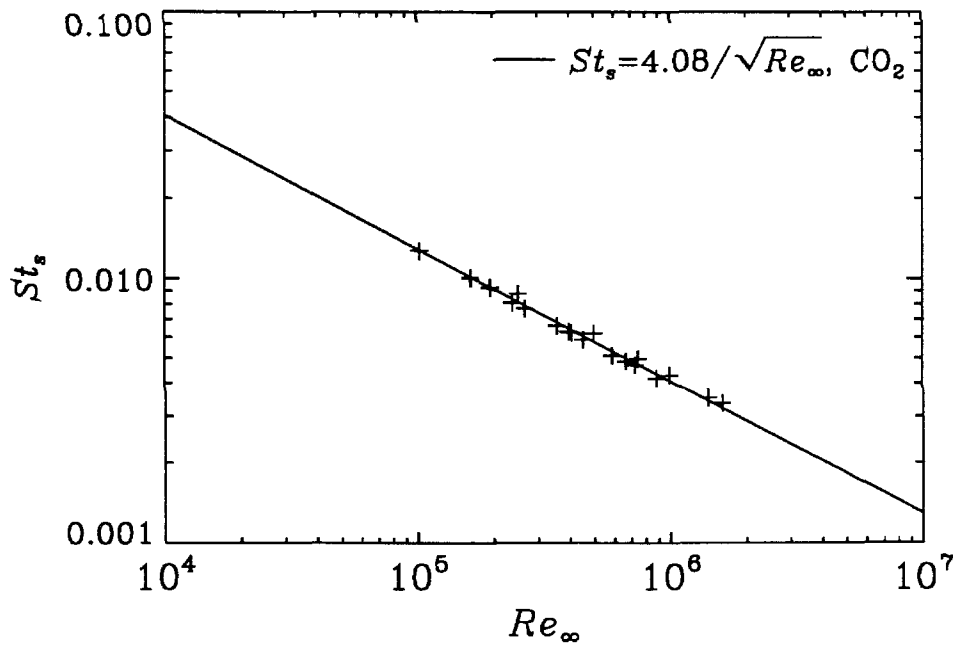
FIG. 4.3. Stagnation point heat flux in dimensionless form predicted by Sutton and Graves' correlation.

As may be seen, the heat transfer coefficient k can be considered as a constant for each in the range of the present experiment. Evidently, k is only a weak function of parameters in the freestream and at the edge of the boundary layer at the stagnation point.

4.1.2 Heat Flux Distribution on the Sphere

In Lees's study of laminar heat transfer rate over blunt-nosed bodies described in section (4.1.1), he also investigated the heat transfer distribution over spheres. According to his result, the heat transfer distribution normalized with the stagnation point heat transfer rate is given by

$$\frac{\dot{q}(\theta)}{\dot{q}_s} = \frac{2\theta \sin \theta \left\{ \left(1 - \frac{1}{\gamma_\infty M a_\infty^2}\right) \cos^2 \theta + \left(\frac{1}{\gamma_\infty M a_\infty^2}\right) \right\}}{\sqrt{D(\theta)}} , \qquad (4.16)$$

where

$$D(\theta) = \left(1 - \frac{1}{\gamma_\infty M a_\infty^2}\right) \left(\theta^2 - \frac{\theta \sin 4\theta}{2} + \frac{1 - \cos 4\theta}{8}\right)$$
$$+ \frac{4}{\gamma_\infty M a_\infty^2} \left(\theta^2 - \theta \sin 2\theta + \frac{1 - \cos 2\theta}{2}\right) . \qquad (4.17)$$

In Fig. 4.4, the ratio $\dot{q}(\theta)/\dot{q}_s$ is plotted as a function of θ for $Ma_\infty = 2.0, 5.0$ and ∞, with $\gamma_\infty = 1.4$, and for $Ma_\infty = 5.0$, with $\gamma_\infty = 1.2$. The quantity $\sqrt{p/p_s}$ for $Ma_\infty = 5.0$ is also shown in Fig. 4.4 for comparsion. According to the modified Newtonian flow approximation for spheres,

$$\frac{p}{p_s} = \cos^2 \theta + \left(\frac{1}{\gamma_\infty M a_\infty^2}\right) \sin^2 \theta . \qquad (4.18)$$

Evidently, for $Ma_\infty > 5.0$, Eq. (4.16) is close to its hypersonic limits and becomes Mach number independent. It will also be a weak function of γ_∞ and appears independent of the freestream Reynolds number, a result which has its analogy in the blunt body pressure distribution.
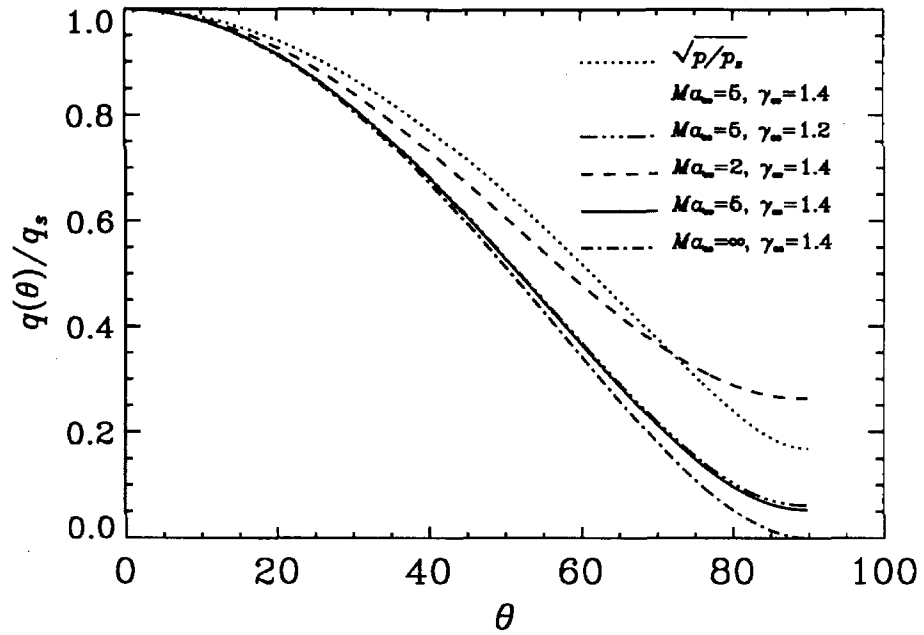
FIG. 4.4. Laminar heat transfer rate distribution over a sphere with Lees' theory (see Eq. (4.16)).

4.2 Comparison with Experimental Data and Computational Results

Candler's viscous code was used to compute the heat transfer rate along the wall of the model. For viscous reacting flow, the heat flux due to diffusion of species s should be taken into account. Therefore, the surface heat transfer is written as

$$\dot{q}_w = \left(k \frac{\partial T}{\partial y} \right)_w + \left(\rho D_{12} \sum_s h_s \frac{\partial c_s}{\partial y} \right)_w .$$ (4.19)

Since the viscous code provided by Candler was set up for the noncatalytic wall boundary condition (see section 3.1.5), the second term of Eq. (4.19) was put equal to zero in the heat flux computation. The experimental heat transfer data were then compared with the theoretical predictions and numerical computations in the following section.

4.2.1 Stagnation Point Heat Transfer Rate

The measured stagnation point heat transfer rate was normalized to form the Stanton number, and a plot of this against the Reynolds number is shown in Fig. 4.5. Also shown in Fig. 4.5. are the theoretical predictions of Fay and Riddell's correlation of the equilibrium boundary layer for air, nitrogen and carbon dioxide. The mean value, standard deviation and maximum deviation of heat transfer coefficient k for experimental data of each gas are summarized in Table 4.2, along with those of computational results using Candler's viscous code. As may be seen, the agreement of the present measurements with theoretical predictions of Fay and Riddell is good.

	Experimental			Computational		
Gas	$\bar{k}$	$\sigma/\bar{k}$	$(\Delta k/\bar{k})_{max}$	$\ddot{k}$	$\sigma/\bar{k}$	$(\Delta k/\bar{k})_{max}$
N_2	4.99	5.6 %	5.1 %	4.71	12.0 %	7.3 %
Air	4.77	5.5 %	10.9 %	5.07	5.6 %	11.1 %
CO_2	3.65	7.3 %	5.2 %	3.65	12.6 %	7.3 %

Table 4.2 Summary of the mean value, standard deviation, and maximum deviation of k (Eq. (4.10)) of experimental data and computational results.

In Fig. 4.6, the experimental data for nitrogen are compared with the numerical results and Lees's theory. In Fig. 4.7 and Fig. 4.8, the experimental data for air and carbon dioxide are compared with the numerical results and the existing data obtained by the ballistic range facility at NASA Ames (Yee et al, 1961). Lees' theory for air and Sutton and Graves's correlation for carbon dioxide are also plotted in Fig. 4.7 and Fig. 4.8, respectively. All the data follow the theoretical predictions though data show more scatter for the carbon dioxide case. The agreement of computational results with the experimental data is also good. It seems that the experimental data for carbon dioxide agree better with Fay and Riddell's equilibrium correlation than with Sutton and Graves' correlation.
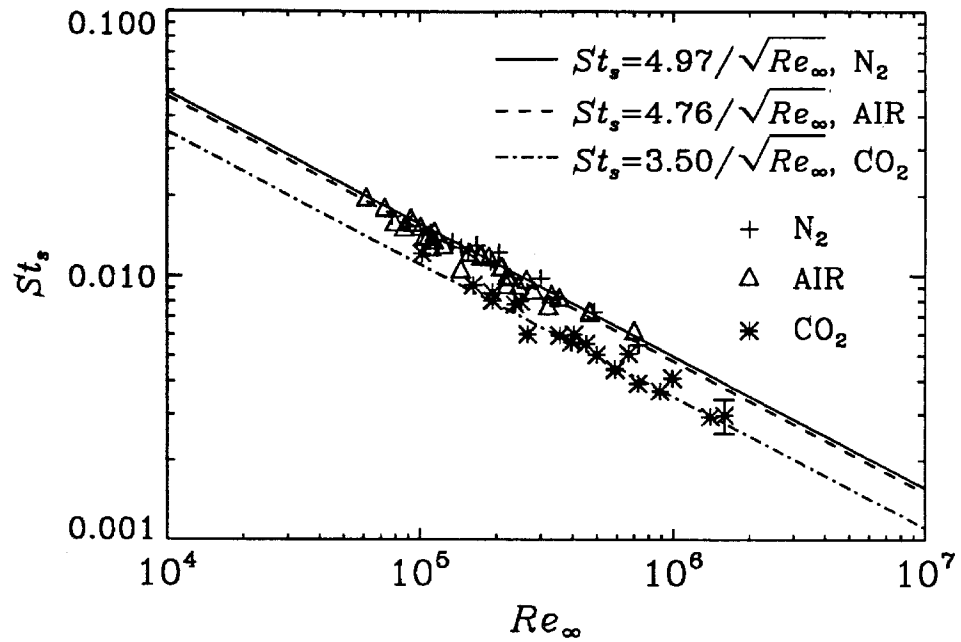
FIG. 4.5. Experimental stagnation point heat fluxes of T5 in dimensionless form and comparison with Fay and Riddell's correlations
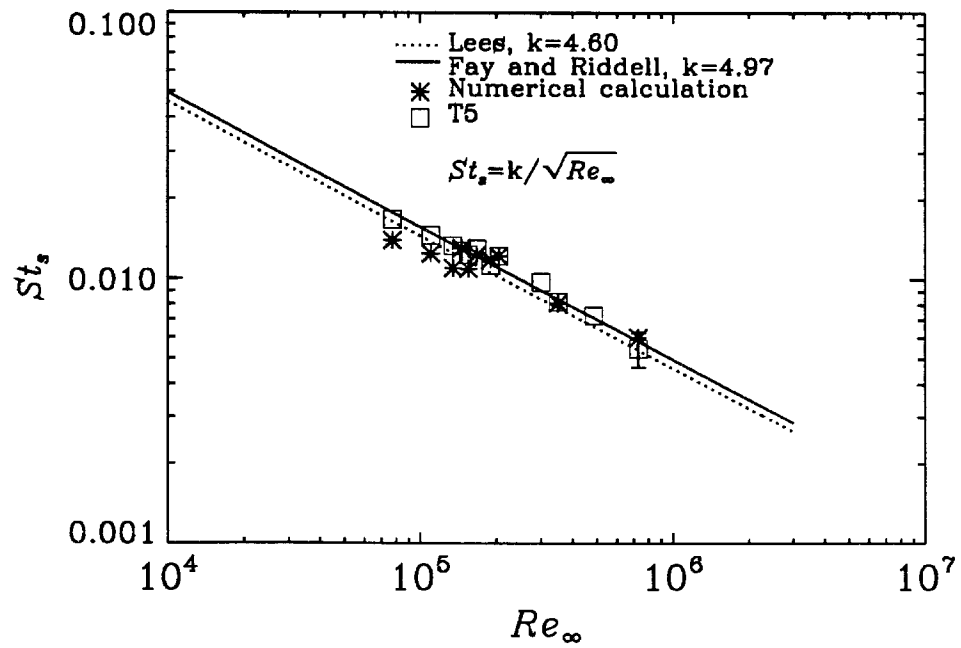
FIG. 4.6. Comparison of experimental stagnation point heat fluxes of T5 , numerical results, and theoretical predictions for N_2.
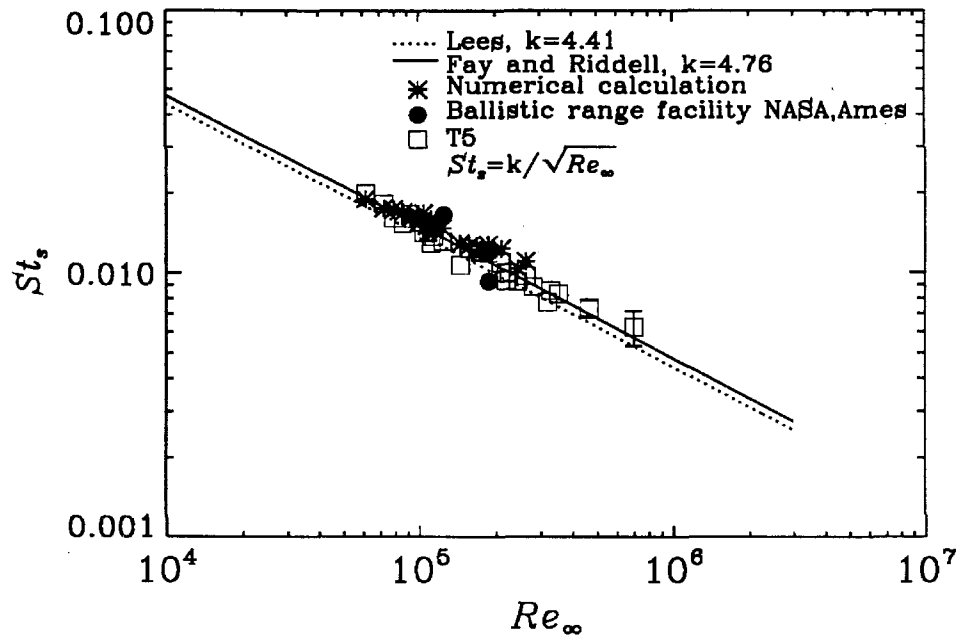
FIG. 4.7. Comparison of experimental stagnation point heat fluxes of T5 and NASA Ames' ballistic range facility, numerical results, and theoretical predictions for air.
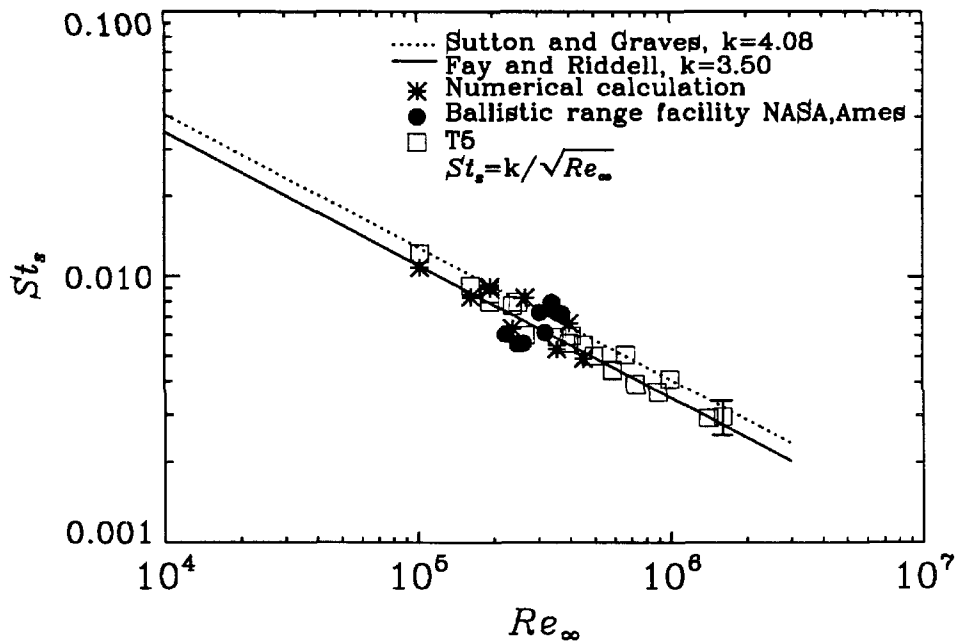
FIG. 4.8. Comparison of experimental stagnation point heat fluxes of T5 and NASA Ames' ballistic range facility, numerical results, and theoretical predictions for CO_2.

From Fig. 4.6 and Fig. 4.7, it is seen that Lees' theory gives lower heat transfer rate than Fay and Riddell's correlation for nitrogen and air. Actually, Table 4.1 suggests that Lees' theory gives heat transfer rate about 7.4 % lower than Fay and Riddell's correlation for both nitrogen and air. As shown in Kemp *et al.* (1959), Lees' theory for the stagnation point heat transfer rate is low by a factor $(\rho_e \mu_e / \rho_w \mu_w)_s^{0.1}$, in addition to having no Lewis number term. The value of $\dot{q}_s$ obtained by Fay and Riddell's equilibrium correlation can be larger than Lees' by a factor 1.3. The reason we obtained a smaller deficit than Kemp *et al.* (1959) is that $\bar{\gamma}$ in the present calculation is overestimated by Eq. (4.3). The average value of $\bar{\gamma}$ in the present work is about 1.39 compared with 1.13 used by Kemp *et al.*.

The error bars for the heat transfer measurements in the plots shown above represent an accuracy of 15 %, 10 % of which comes from the uncertainty of the freestream conditions and the other 5 % is contributed by the uncertainty of the bulk heat transfer properties of the thermocouple materials, see Germain (1993). Performing an experiment in the T3 shock tunnel using similar gauges, Gai and Joe (1992) assessed the accuracy to be on the order of 15 % too.

4.2.2 Heat Flux Distribution on the Sphere

Experimental heat flux distributions are shown in Fig. 4.9 to Fig. 4.17. The distribution obtained from Lees' formula for laminar flow, Eq. (4.16), is also plotted on each figure. As discussed in section 4.1.2, Eq. (4.16) is a weak function of γ_∞ and becomes Mach number independent for $Ma_\infty > 5.0$. Therefore, $\gamma_\infty = 1.2$ and $Ma_\infty = 5.0$ were used for the theoretical predictions in the present study. For nitrogen and air cases, experimental data and the theoretical predictions are in reasonably good agreement. But for the carbon dioxide cases, data show much more scatter and an unexpected phenomenon occurs in the heat flux distribution. For each model, it seems that the data follow the theoretical curve reasonably well in the first few shots, and start to rise over the theoretical curve in the later shots, especially for those at 40° and 60°. Also this transition-like phenomenon seems more obvious for shots with higher freestream Reynolds number. Transition is not expected

at our values of Re_∞ for the front part of sphere flow under investigation because of the strong favorable pressures gradient associated with it. However, having a close look at each model, it was found that the surface of each model, especially at the nose region, was roughened after surviving the severe conditions of high temperature and high pressure. The surface roughness was estimated for each model at the end of the present experiment and is listed in Table 4.3. Note that, for each model, the surface got rougher and rougher as the series of experiments progressed and the carbon dioxide tests came last. This together with the relatively higher Reynolds numbers in the cases of carbon dioxide than in the cases of nitrogen and air may explain why this transition-like phenomenon is most evident in the carbon dioxide experiments.

D(in.)	2	3	4	6
Roughness ($\times 10^{-3}$ in.)	0.220	0.455	0.875	0.875

Table 4.3 Roughness at the surface of models at the end of test.
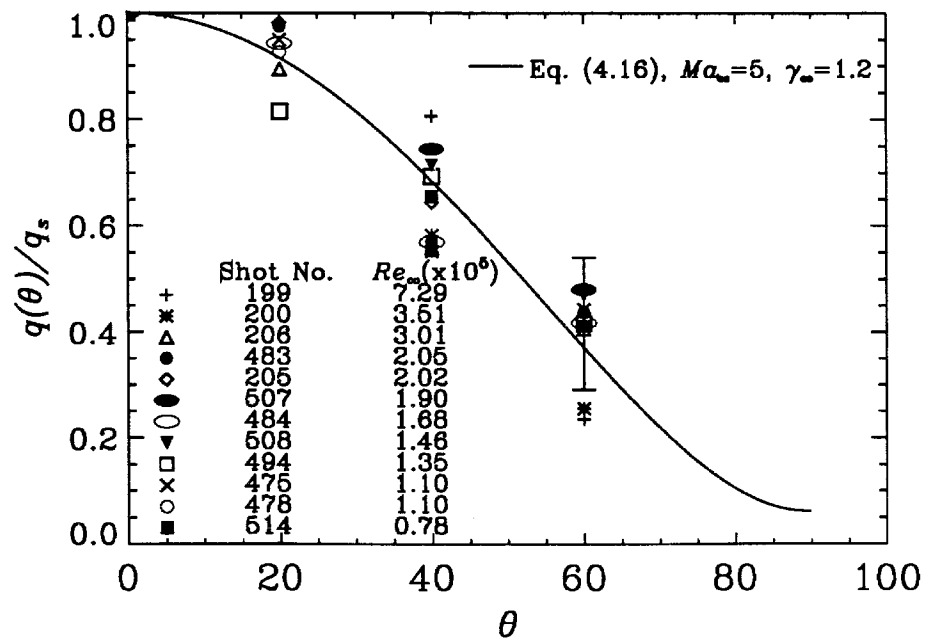
FIG. 4.9. Comparison of experimental heat flux distribution of T5 and Lees' theoretical prediction (Eq. 4.16) for N_2.
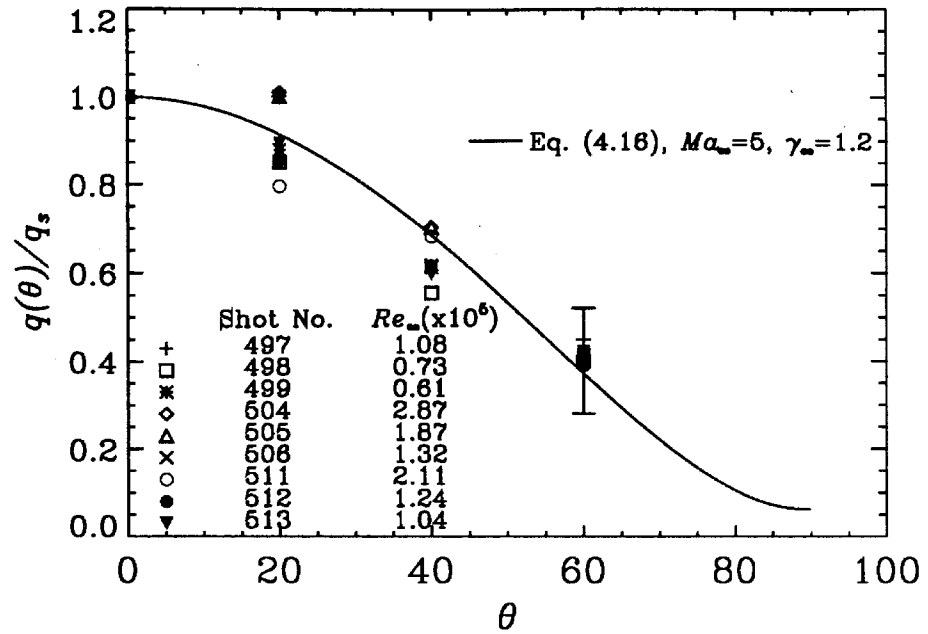
FIG. 4.10. Comparison of experimental heat flux distribution over a sphere of 2 in. diameter and Lees' theoretical prediction (Eq. 4.16) for air.
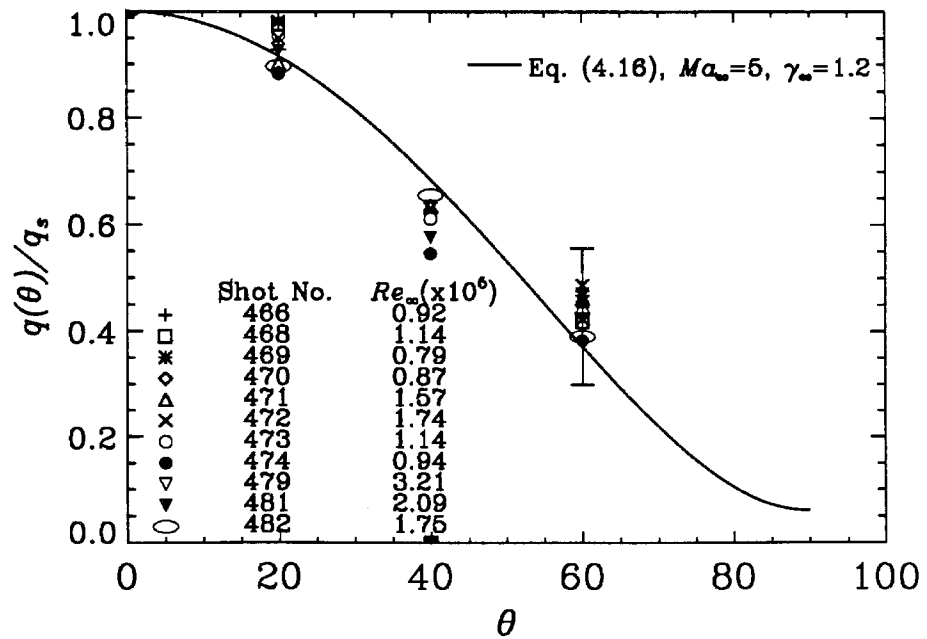
FIG. 4.11. Comparison of experimental heat flux distribution over a sphere of 3 in. diameter and Lees' theoretical prediction (Eq. 4.16) for air.
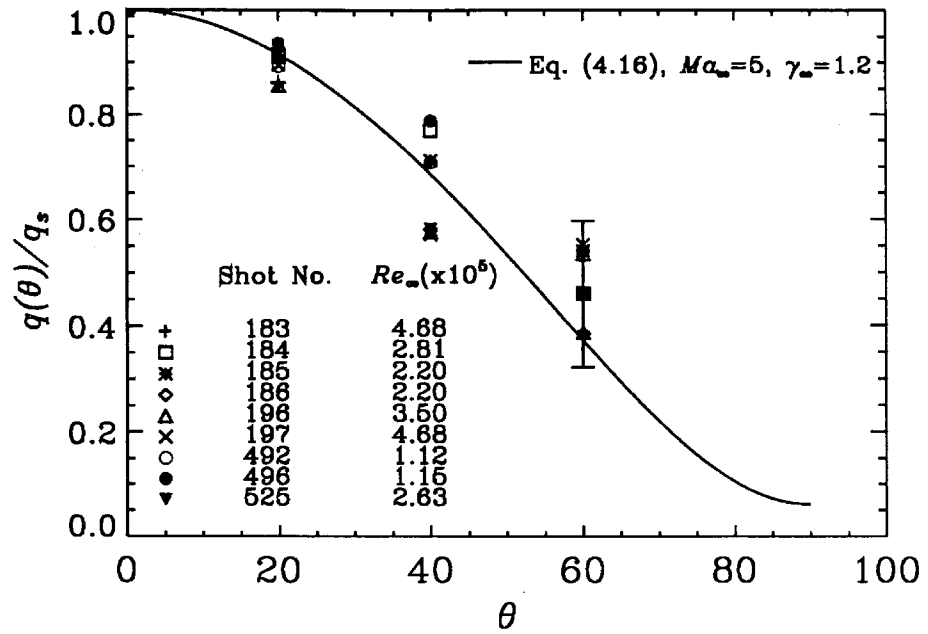
FIG. 4.12. Comparison of experimental heat flux distribution over a sphere of 4 in. diameter
and Lees' theoretical prediction (Eq. 4.16) for air.
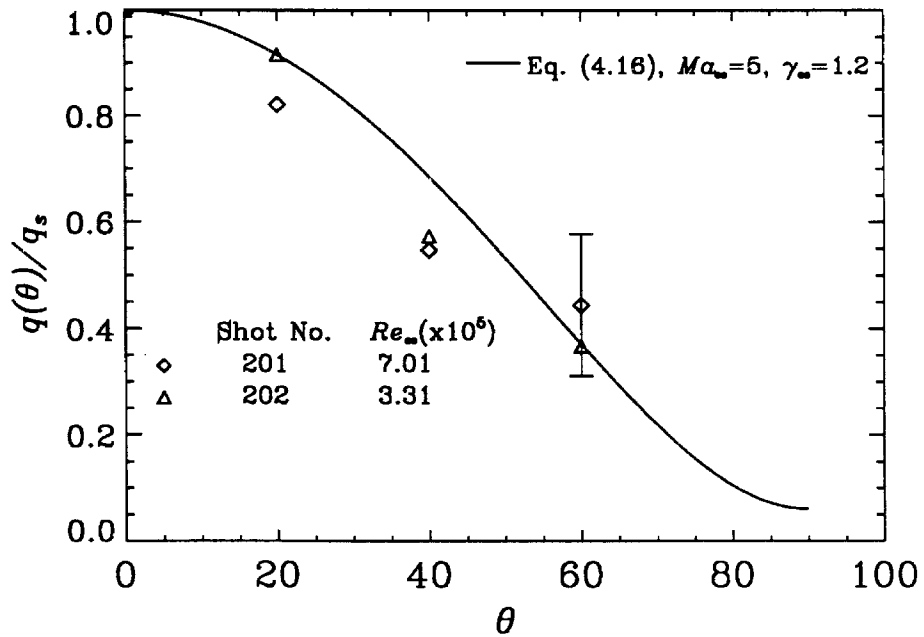
FIG. 4.13. Comparison of experimental heat flux distribution over a sphere of 6 in. diameter
and Lees' theoretical prediction (Eq. 4.16) for air.
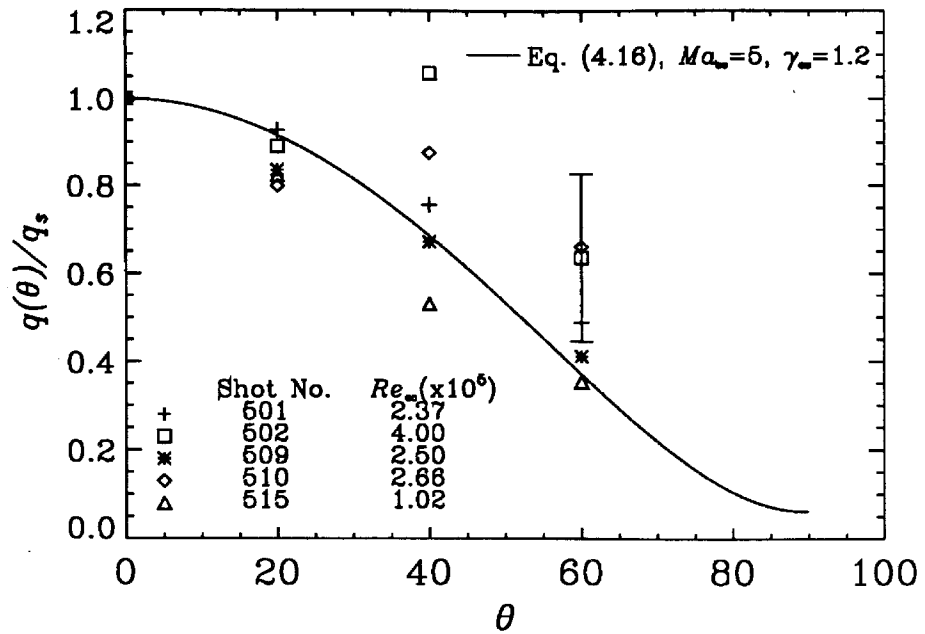
FIG. 4.14. Comparison of experimental heat flux distribution over a sphere of 2 in. diameter and Lees' theoretical prediction (Eq. 4.16) for CO_2.
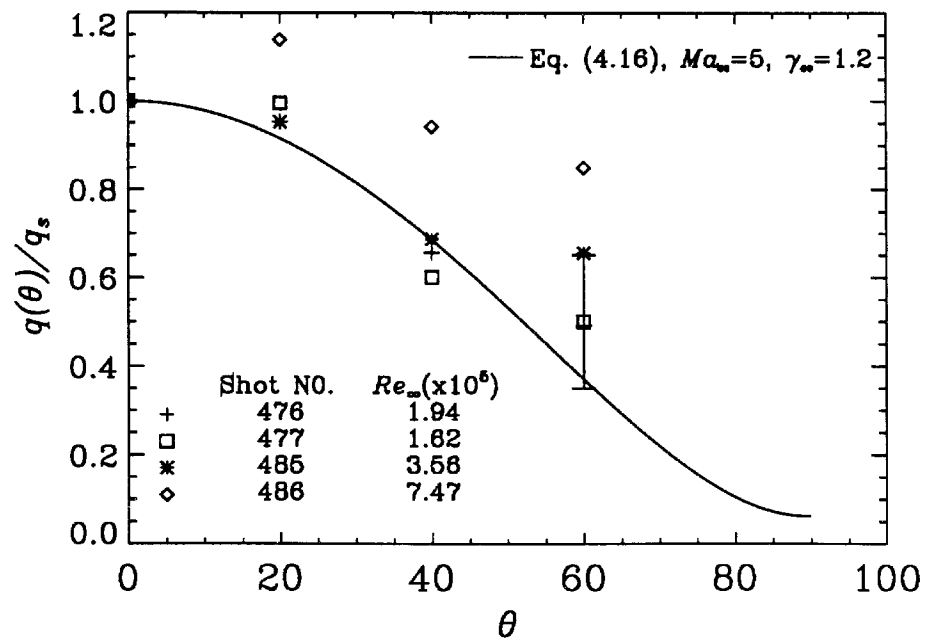
FIG. 4.15. Comparison of experimental heat flux distribution over a sphere of 3 in. diameter and Lees' theoretical prediction (Eq. 4.16) for CO_2.
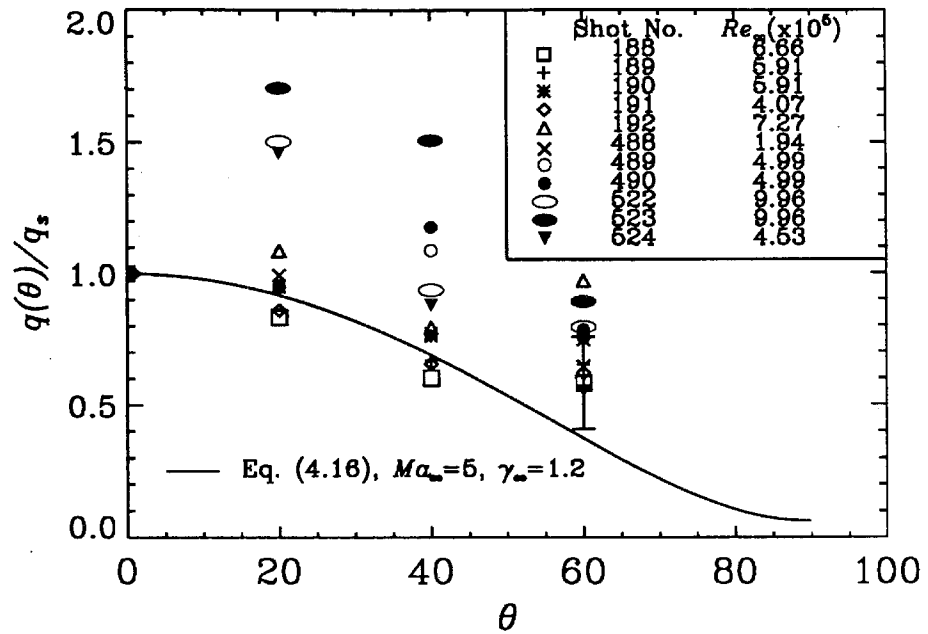
FIG. 4.16. Comparison of experimental heat flux distribution over a sphere of 4 in. diameter and Lees' theoretical prediction (Eq. 4.16) for CO_2.
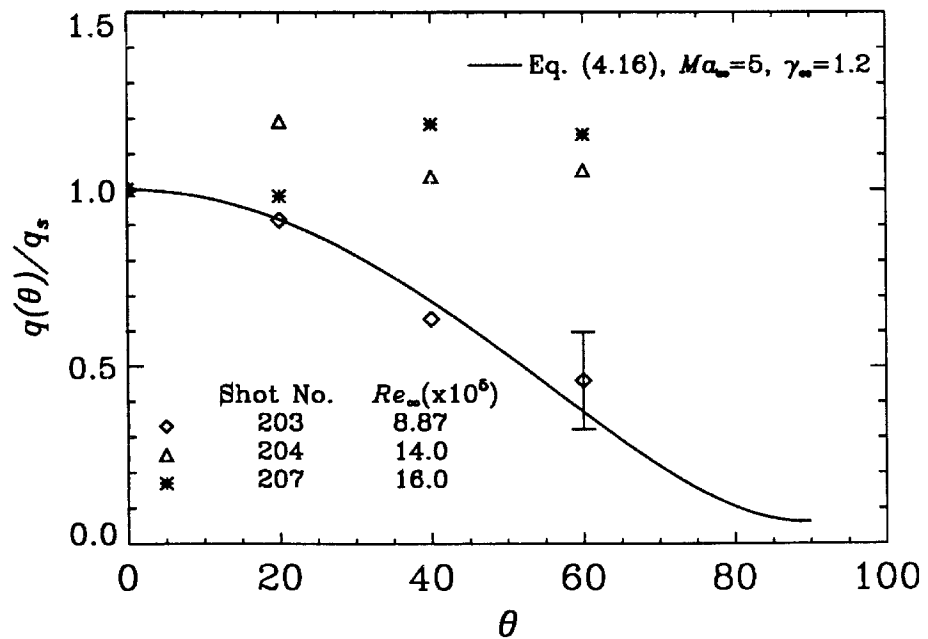
FIG. 4.17. Comparison of experimental heat flux distribution over a sphere of 6 in. diameter and Lees' theoretical prediction (Eq. 4.16) for CO_2.

A further attempt to understand this interesting and peculiar phenomenon for carbon dioxide is to look at the data of heat flux distribution in the space of local Stanton number, St_x, and local Reynolds number, Re_x. The local Stanton number and local Reynolds number based on the distance from the stagnation point x are defined as

$$St_x = \frac{\dot{q}_x}{\rho_e u_e h_0} \ ; \tag{4.20}$$

$$Re_x = \frac{\rho_e u_e x}{\mu_e} \ . \tag{4.21}$$

Figs. 4.18 to 4.20 show the examples of theoretical heat transfer rates at 20°, 40°, and 60° for nitrogen, air, and carbon dioxide. The local heat transfer rate $\dot{q}_x$ for the theoretical prediction is obtained by multiplying Lees' formula, Eq. (4.16), with the stagnation point heat transfer rate $\dot{q}_s$ taken from Fay and Riddell's equilibrium correlation. As pointed out in section 4.2.1, Fay and Riddell's correlation for $\dot{q}_s$ agrees with the experimental data better than Lees'. The $\dot{q}_x$ is then normalized by ρ_e, u_e, and h_0 obtained from Candler's inviscid code.
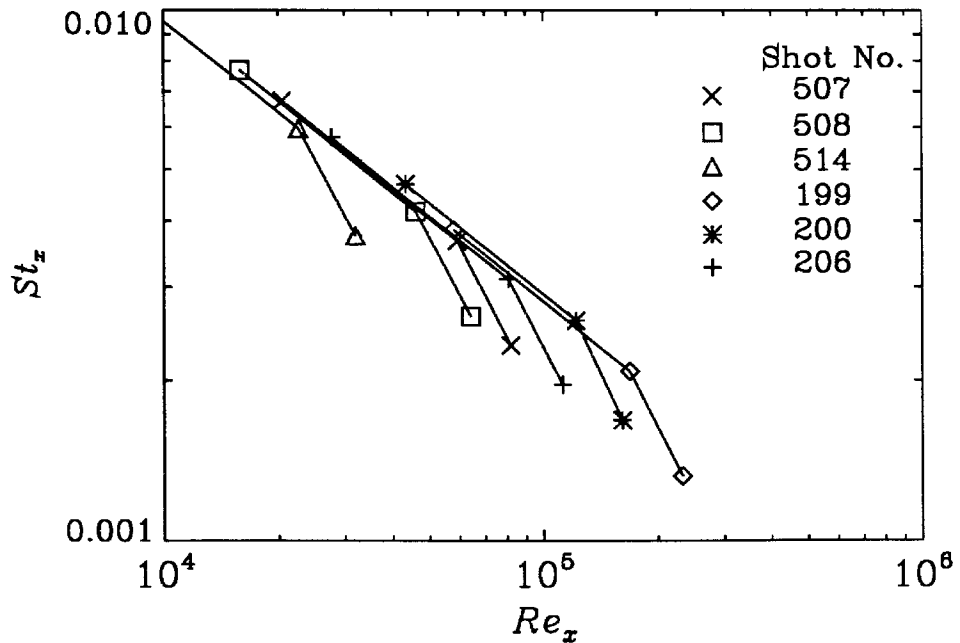
FIG. 4.18. Theoretical heat transfer rates in dimensionless form at 20°, 40°, and 60° for selected experimental conditions for N_2. Theoretical predictions of each shot are connected by a solid line.
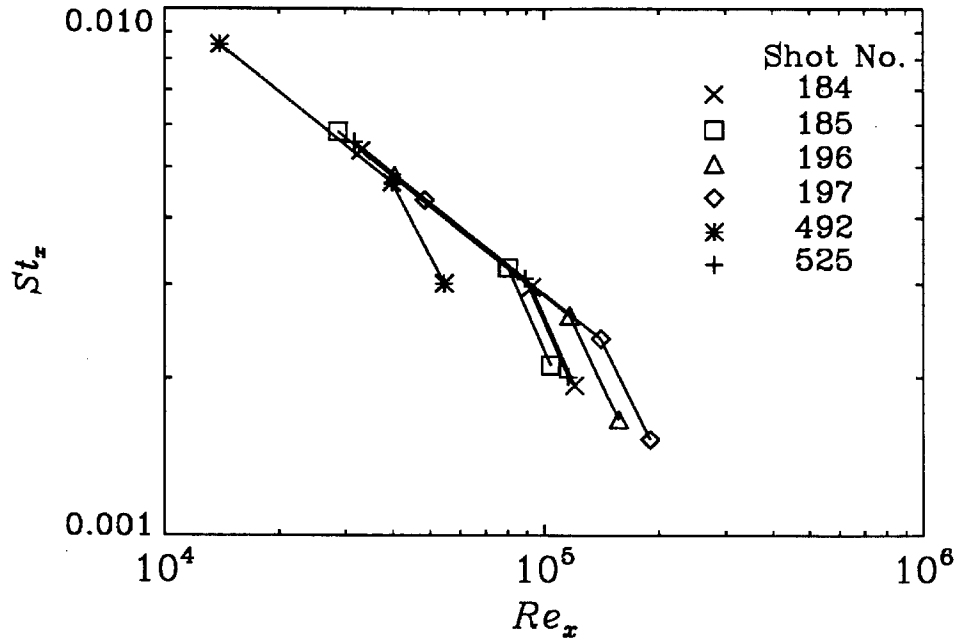
Fig. 4.19. Theoretical heat transfer rates in dimensionless form at 20°, 40°, and 60° for selected experimental conditions for air. Theoretical predictions of each shot are connected by a solid line.
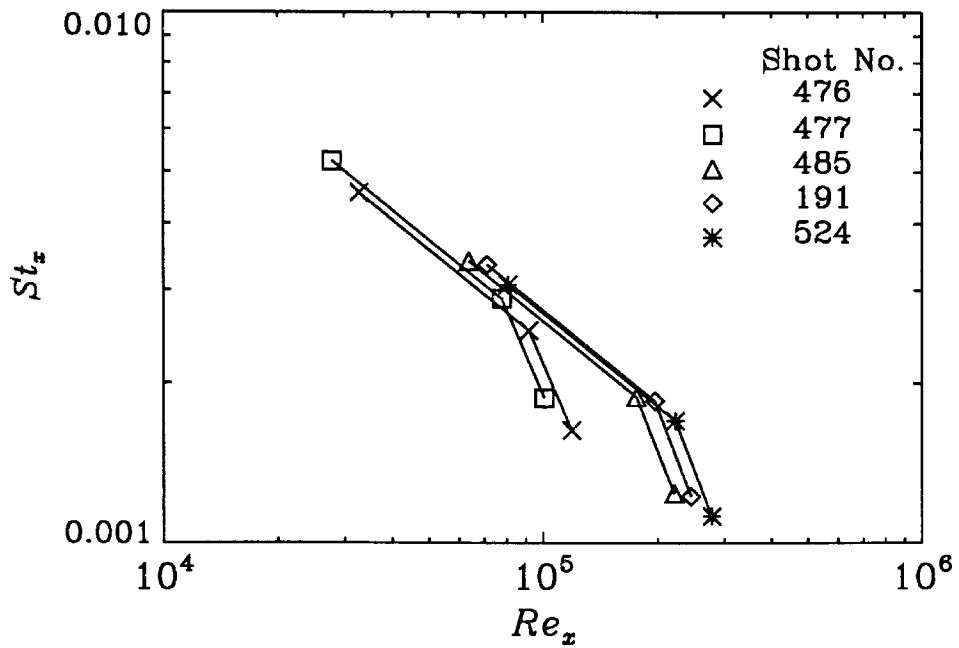
Fig. 4.20. Theoretical heat transfer rates in dimensionless form at 20°, 40°, and 60° for selected experimental conditions for CO_2. Theoretical predictions of each shot are connected by a solid line.

As may be seen in Figs. 4.18 to 4.20, the dependence of St_x on Re_x is a function of angle θ. No simple relation like

$$St_x = \frac{b}{Re_x^a} \qquad (4.22)$$

exists. Here a and b are constants. As Re_x increases, St_x tends to decrease more steeply on the Log-Log plot for each shot. However, if we plot the theoretical heat transfer rates at 20°, 40°, and 60° together for all the experimental conditions for each gas, it is found that Eq. (4.22) is actually a satisfactory assumption. Figs. 4.21 to 4.23 show the theoretical heat flux distributions for all the experimental conditions for each gas. The line of least-squares curve fitting to the theoretical heat flux distributions is also plotted for each gas. The standard deviation for each gas is about 13 %. The simple relation like Eq. (4.22) seems to correlate the theoretical heat flux distributions approximately. The correlation of theoretical heat flux distributions of each test gas suggests that the normalized experimental data should follow the same trend and should be contained mostly inside the range of standard deviations of the theoretical predictions.
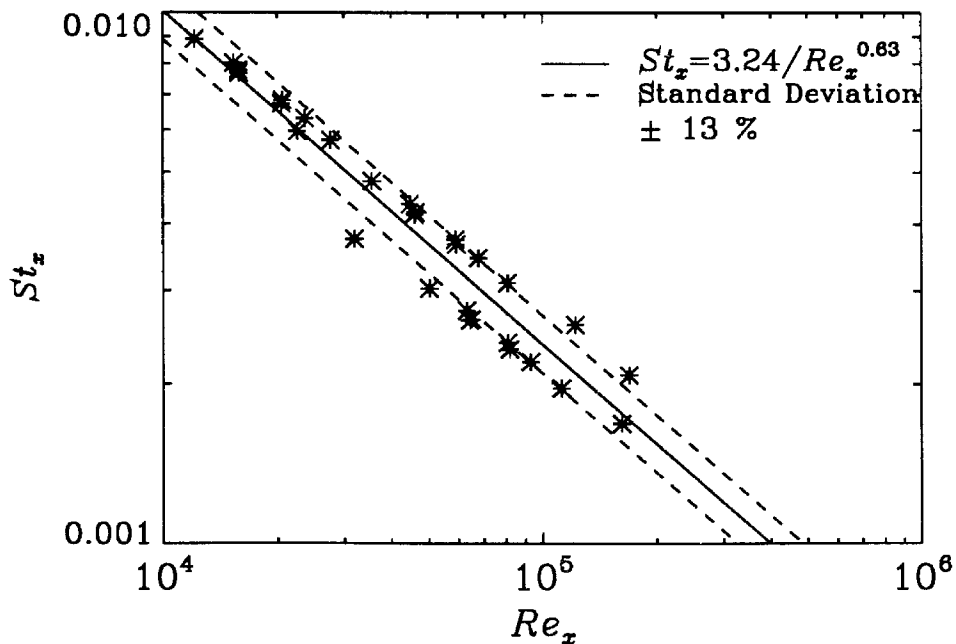
Fig. 4.21. Theoretical heat transfer rates in dimensionless form at 20°, 40°, and 60° for all the experimental conditions for N_2.
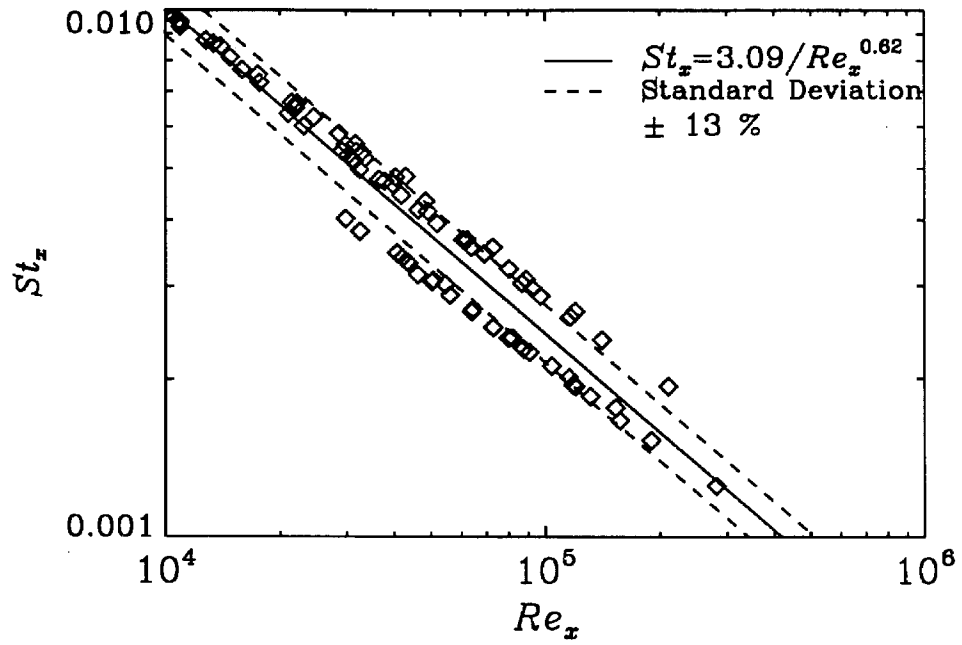
FIG. 4.22. Theoretical heat transfer rates in dimensionless form at 20°, 40°, and 60° for all the experimental conditions for air.
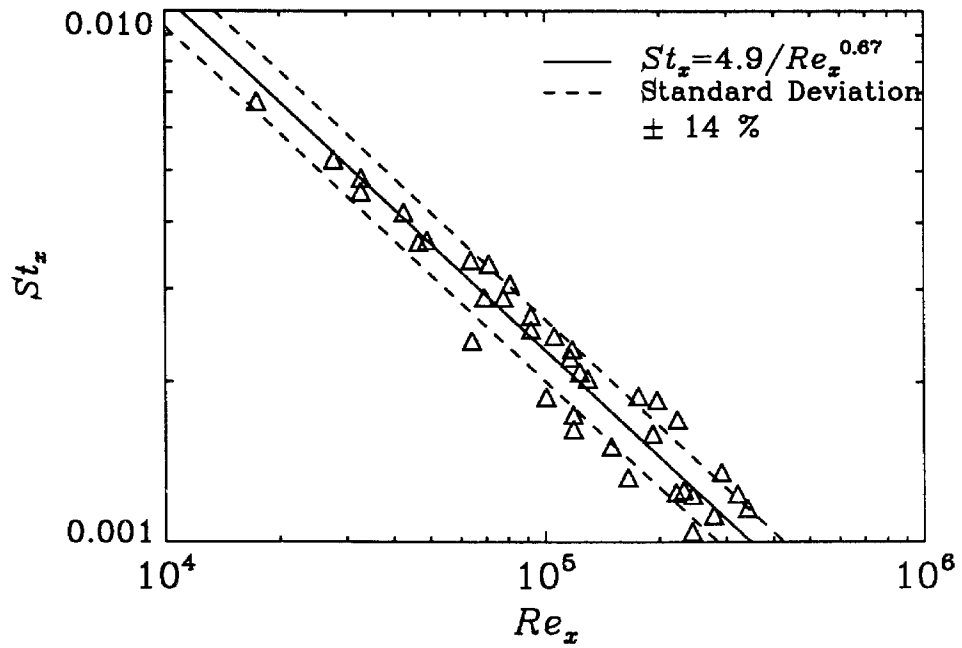
FIG. 4.23. Theoretical heat transfer rates in dimensionless form at 20°, 40°, and 60° for all the experimental conditions for CO_2.

The measured heat transfer rates at 20°, 40°, and 60° were normalized to form the local Stanton numbers, and plots of these against the local Reynolds numbers are shown in Fig. 4.24, Fig. 4.25, and Fig. 4.26 for nitrogen, air, and carbon dioxide, respectively. Also shown in Figs. 4.24 to 4.26 are the correlations of the theoretical predictions. As may be seen, the agreement of the present measurements for nitrogen and air with the approximate correlations of theoretical predictions is reasonably good. Experimental data broadly follow the approximate correlations. But, for carbon dioxide, the data are more scattered and fall clearly above the correlation of theoretical predictions at high Reynolds numbers. Experimental data tend to deviate upwards instead of downwards as in the theoretical predictions (see Fig. 4.20).
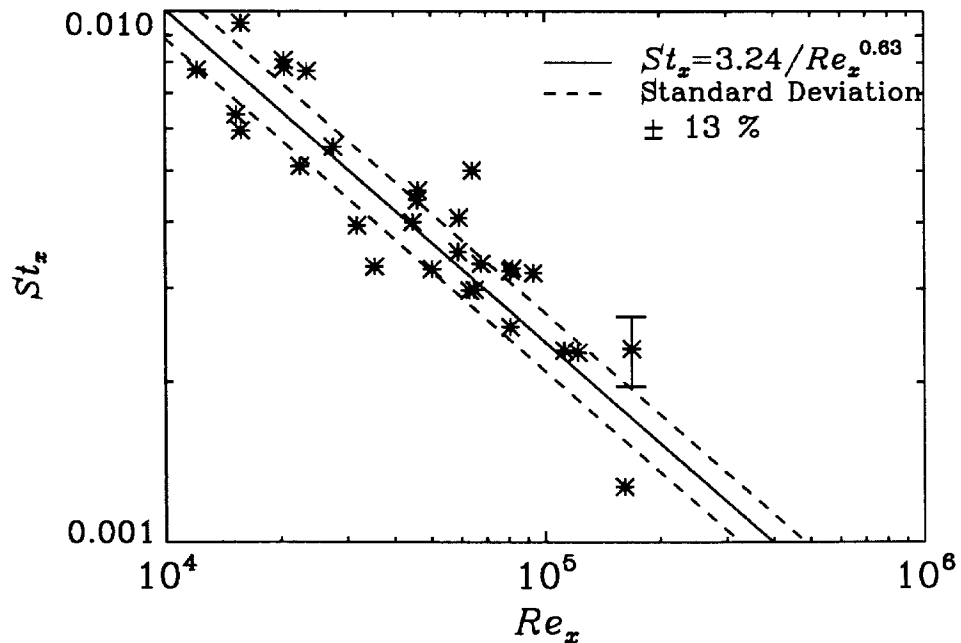
Fig. 4.24. Normalized heat transfer measurements at 20°, 40°, and 60° for all the N_2 shots. The correlation of theoretical predictions in Fig. 4.21 is also plotted.
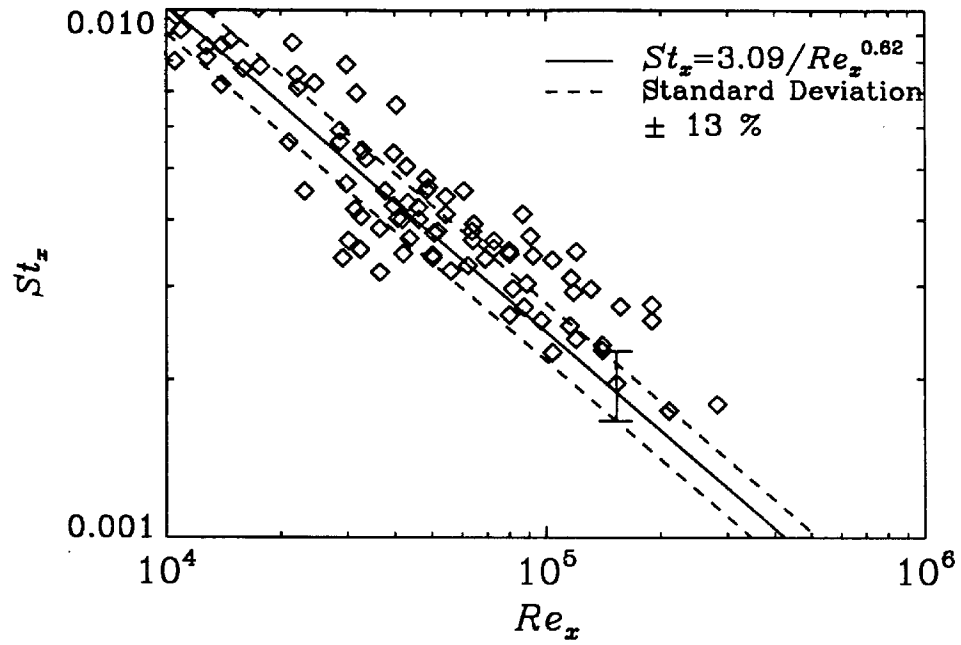
FIG. 4.25. Normalized heat transfer measurements at 20°, 40°, and 60° for all the air shots. The correlation of theoretical predictions in Fig. 4.22 is also plotted.
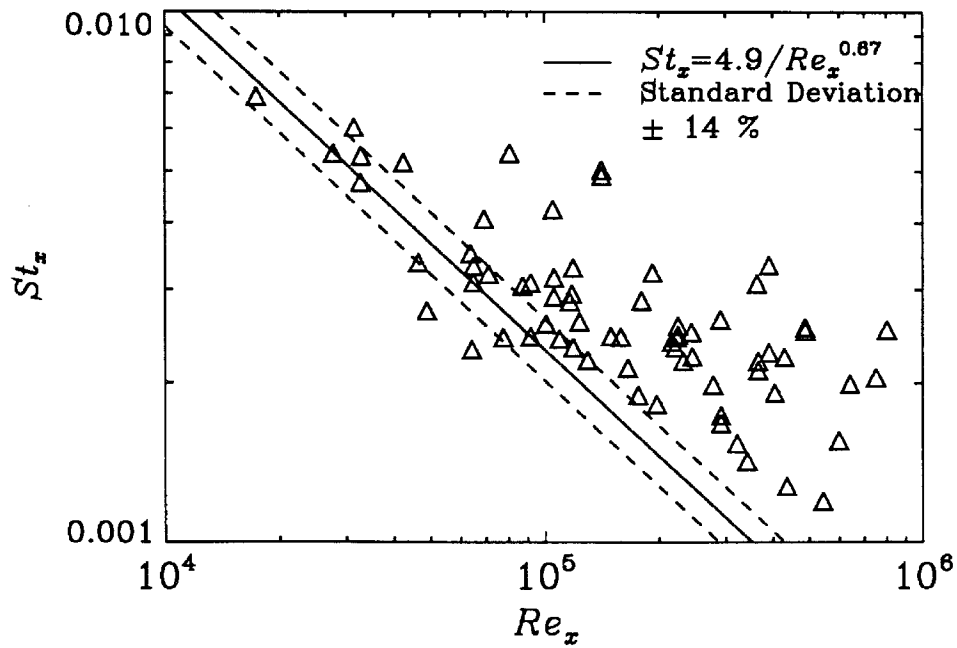
FIG. 4.26. Normalized heat transfer measurements at 20°, 40°, and 60° for all the CO_2 shots. The correlation of theoretical predictions in Fig. 4.23 is also plotted.

Fig. 4.27 shows the comparsion of local Stanton numbers of six carbon dioxide runs with the correlation of theoretical predictions. These six shots were selected because they exhibited different heat flux distributions from Lees' theory in Figs. 4.15 to 4.17. The Reynolds numbers of these shots are relatively high in the present experiment. They are in the order of 10^6. The normalized experimental data in Fig. 4.27 seem to indicate transition to turbulence. It is also interesting to point out that for two close shots with the same model, the transition-like phenomena seem to appear at the same Reynolds number, for example: shot 190 and shot 192 for the 4 in. model, and shot 204 and shot 207 for the 6 in. model.
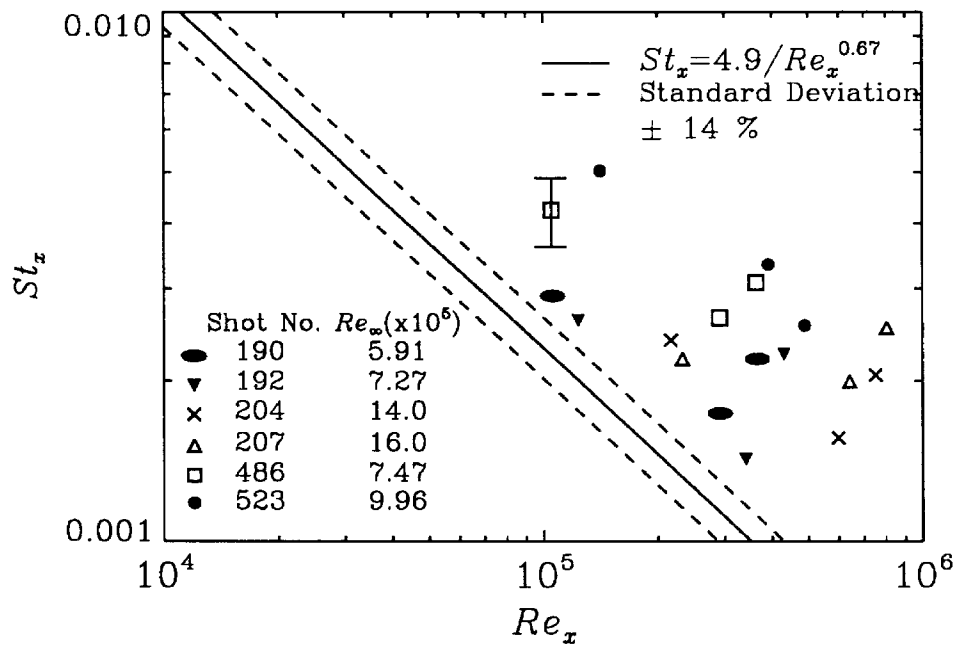
FIG. 4.27. Comparsion of normalized heat transfer measurements at 20°, 40°, and 60° of six carbon dioxide shots with the correlation of theoretical predictions

The computational method was also deployed to compare with experimental heat flux distributions and Lees' theoretical prediction, and to help understand those peculiar heat transfer distributions of carbon dioxide. Examples of this comparsion are shown in Figs. 4.28 to 4.31. These examples represent typical computational results for the test gases. As may be seen, computational results show good agreement with Lees' theory. Therefore, Candler's viscous code with no wall catalysis cannot explain the peculiar heat transfer dis-

tributions of carbon dioxide either. Because of the neglect of the diffusion term in Eq. (4.19), the computational distribution is lower than Lees' theory for most of the after-body.
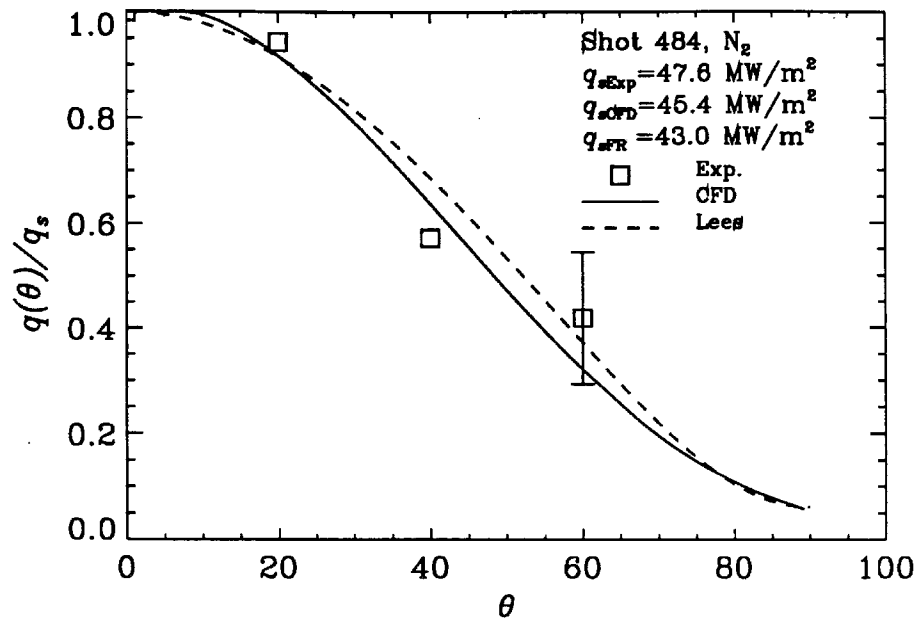
FIG. 4.28. Comparsion of computational heat transfer distribution with Lees' theory and experimental measurements for N_2. FR: Fay and Riddell's equilibrium correlation.
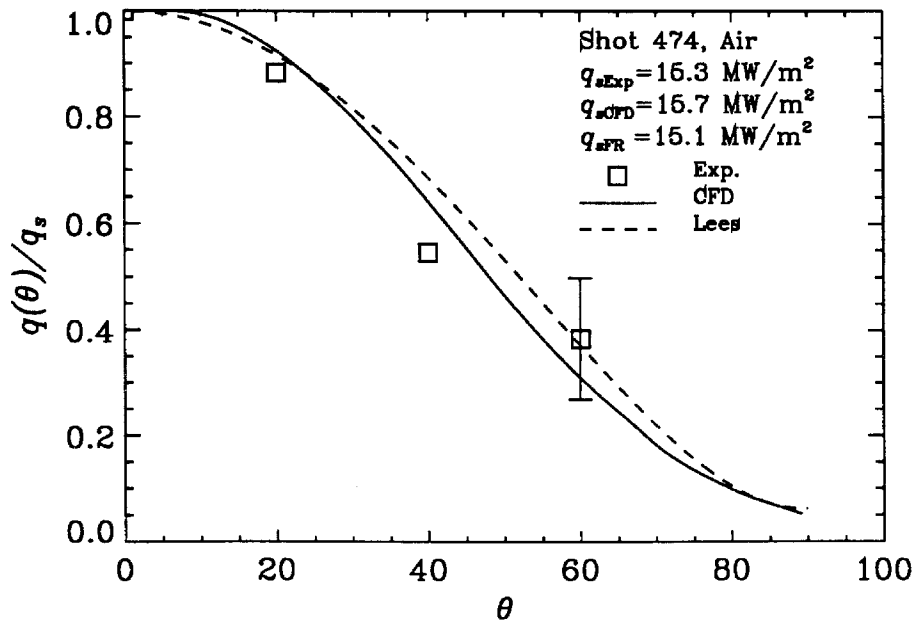
FIG. 4.29. Comparsion of computational heat transfer distribution with Lees' theory and experimental data for air. FR: Fay and Riddell's equilibrium correlation.
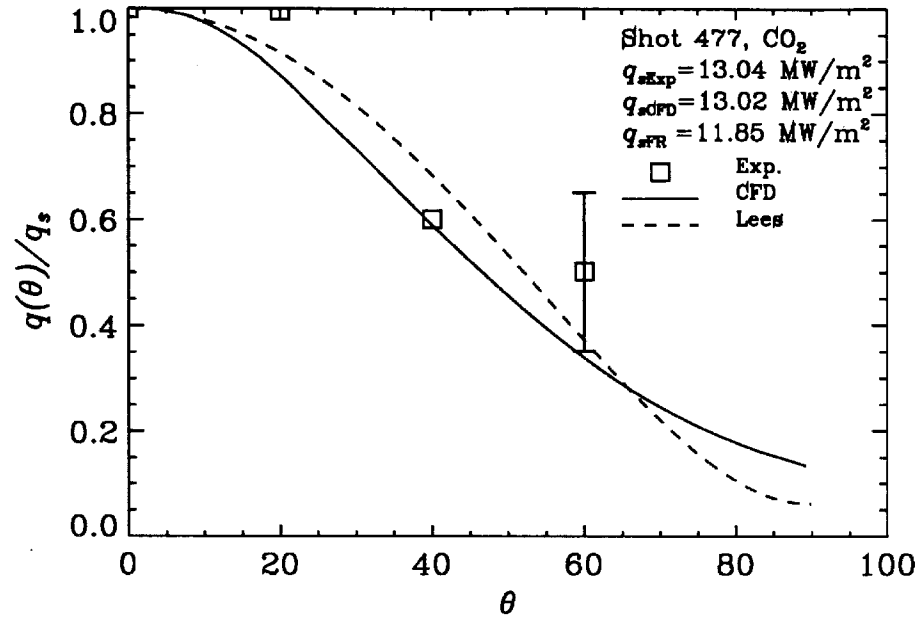
FIG. 4.30. Comparsion of computational heat transfer distribution with Lees' theory and experimental data for CO_2. FR: Fay and Riddell's equilibrium correlation.
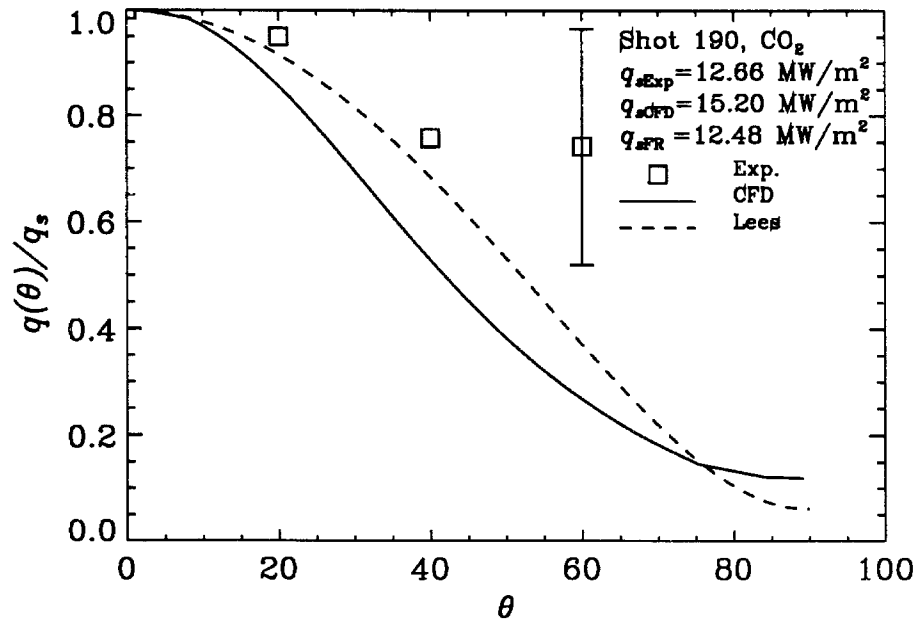
FIG. 4.31. Comparsion of computational heat transfer distribution with Lees' theory and experimental measurements for CO_2. FR: Fay and Riddell's equilibrium correlation.

Although, data seem to indicate the possibility of transition from laminar flow to turbulence because of the surface roughness, a more carefully designed experiment is needed to test this tentative conclusion. A few suggestions to help understand the true mechanism of these interesting heat flux distributions are listed below:

(1) A viscous code which is implemented with the boundary condition of wall catalysis and an adaptive computational grid are needed to investigate the effect on local heat release of the wall catalysis.

(2) Lees' theory has to be reexamined. Lees has dealt with the heat flux distribution on the after-body with an assumption of "local similarity". The real gas properties of air are also implicitly contained. In Lees' approximate solution of similarity differential equations, he took the enthalpy gradient constant around the body, so the non-similar term in the energy equation is identically zero. Since the internal degrees of freedom of carbon dioxide are relatively complex and carbon dioxide consumes larger fraction of energy to equilibrate its thermodynamic states than air, the assumption of "local similarity" needs to be carefully verified.

(3) A more focused experiment has to be designed and accomplished. The experiment must consider the factors of the surface roughness and the wall catalysis. More thermocouples and pressure transducers may also help. Note that the interesting heat flux distributions occurred more obviously in the runs with high freestream Reynolds number, and that the local Reynolds number for the present carbon dioxide experiment can be as high as one million. Togami (1993) investigated the heat flux distributions for flow over a spherically blunted cone in T5 and observed a similar phenomenon for carbon dioxide. He concluded that, by using carbon dioxide, the transition to turbulence can be obtained even with a blunt body. The transition Reynolds number for his experiment is about one million. According to Germain (1993), the transition Reynolds number for a slender cone of 5° half-angle in T5 is also on the order of one million. Matthews (1993) has examined the shuttle Orbiter reentry data and found that the transition data were significantly influenced by disturbances caused by surface roughness of the shuttle tiles. If the Reynolds number based on rough-

ness height is on the order of 100 or greater, the shuttle reentry data showed that transition Reynolds number based on the distance from the stagnation point is dramatically reduced. The Reynolds numbers based on the roughness height of the later shots in the current experiments (see Table 4.3) are on the order of 100. Therefore, the rough surface of the later shots may well have tripped transition.

4.3 Flow Visualization

4.3.1 Experimental Differential Interferograms

Figs. 4.32 to 4.34 present examples of differential interferograms obtained for nitrogen, air and carbon dioxide respectively. These pictures show the continuous variation in density between the bow shock wave and the wall which is expected in relaxing flows.

Differential interferometry measures the gradient of optical path length. Specifically, it measures the component of the gradient in the image plane and in a direction that can be chosen by rotating the Wollaston prism in the setup. The parallel fringes in the undisturbed freestream of the photograph are oriented at right angles to the direction of this component. In order to convert the fringe shift observed in an axisymmetric flow field behind the shock into a refractive index field, from which the density might be inferred, it would be necessary to perform an inversion of the Abel integral equation using the measured fringe shift as input. While this does not present a problem, the result is still ambiguous, since the refractive index may not be interpreted directly as density in a gas whose composition is not uniform. In nitrogen flow, this problem is relatively mild, but if one deals with air, where some 8 species may be expected to be present, the problem is harder. However, the experimental interferograms do provide the important information of the stand-off distance and shock shape. They also provide valuable evidence to validate the numerical code.
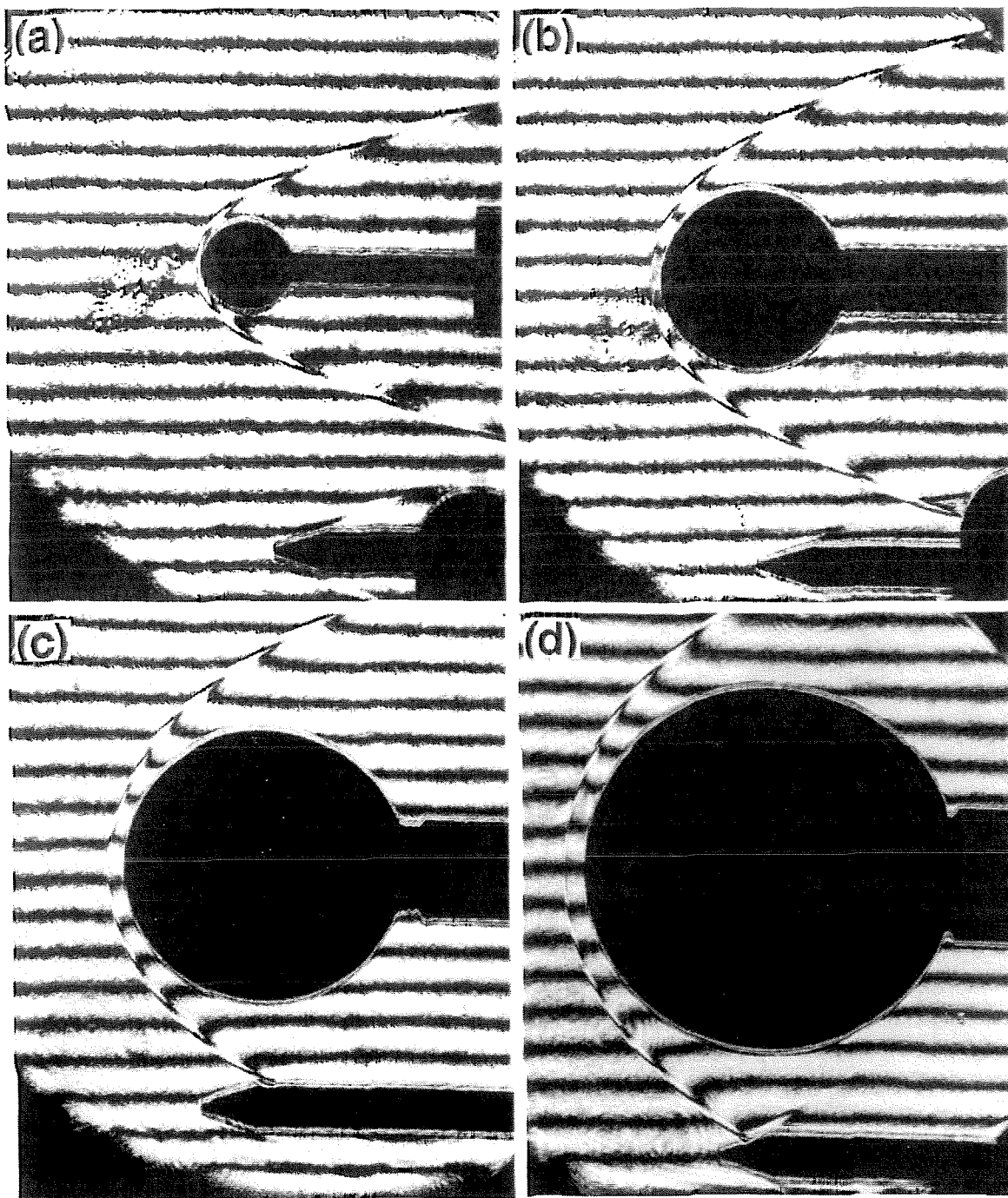
FIG. 4.32. Finite fringe differential interferograms of N_2 flow over sphere. $\lambda = 589$ nm. (a) Shot 518. (b) Shot 514. (c) Shot 475. (d) Shot 594. The blemishes ahead of the bow shock waves in interferograms (a) and (b) are due to a flaw in the optical window.
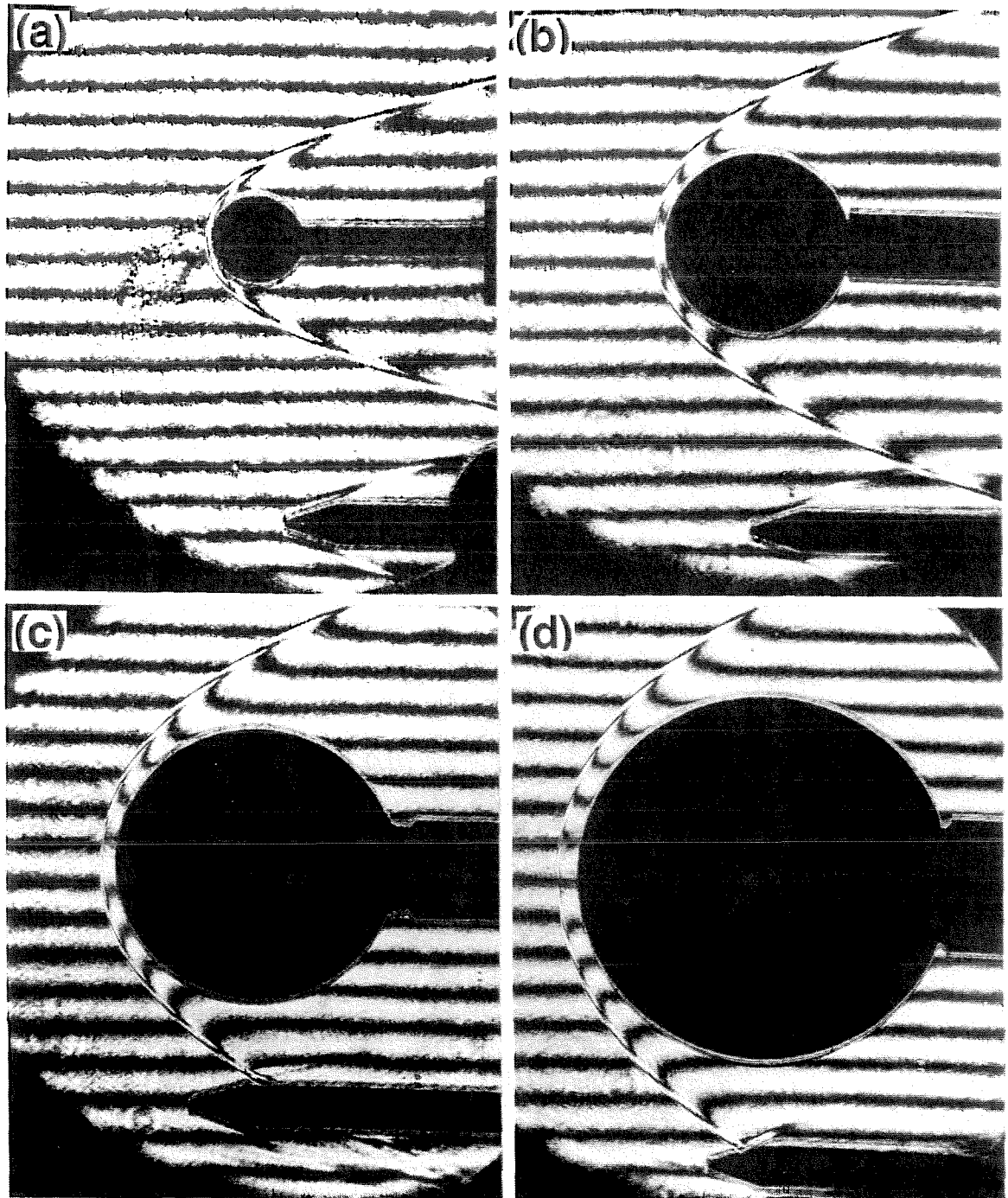
FIG. 4.33. Finite fringe differential interferograms of air flow over sphere. λ = 589 nm.
(a) Shot 519. (b) Shot 497. (c) Shot 472. (d) Shot 491. The blemish ahead of the
bow shock wave in interferogram (a) is due to a flaw in the optical window.
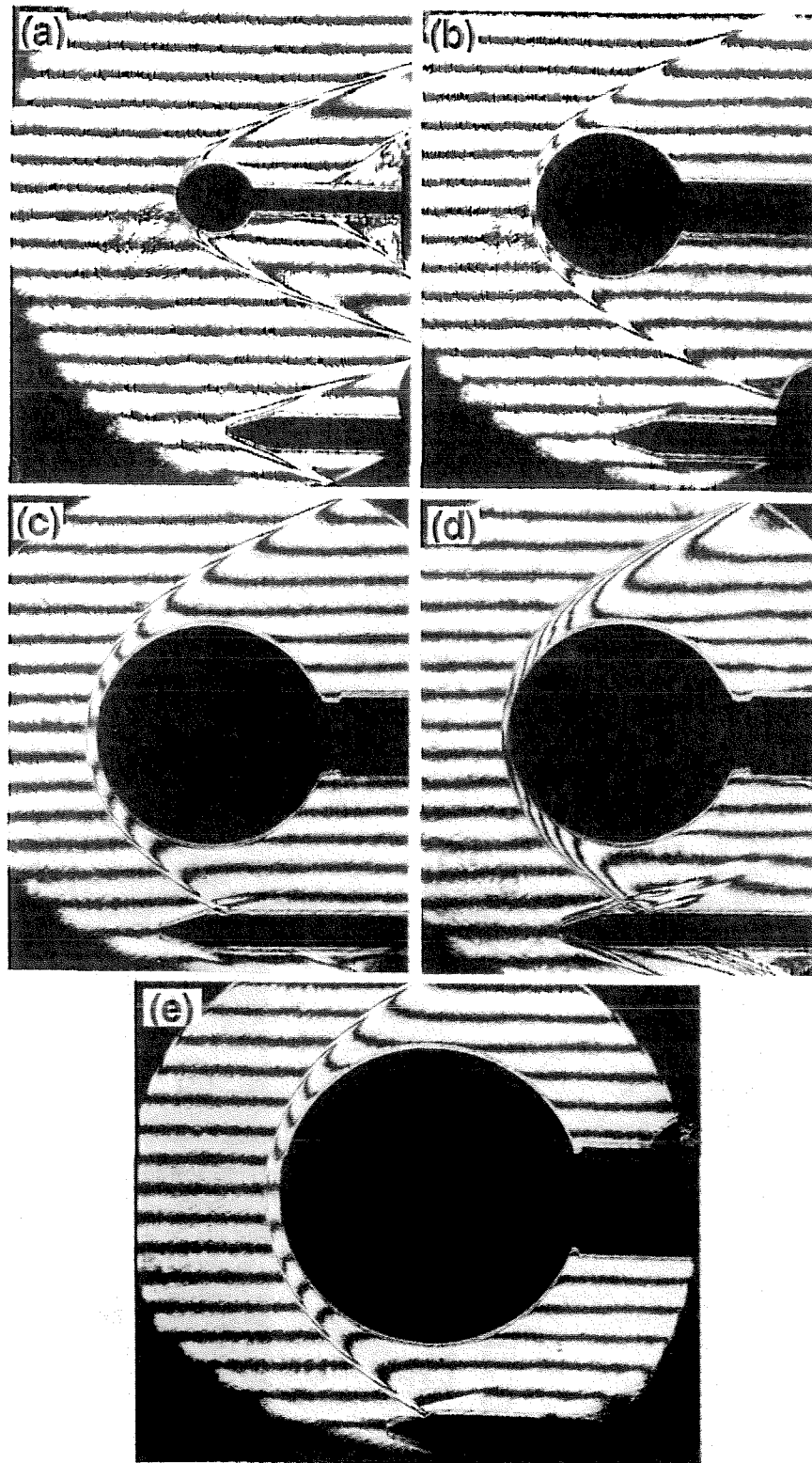
FIG. 4.34. Finite fringe differential interferograms of CO_2 flow over sphere. $\lambda = 589$ nm. (a) Shot 516. (b) Shot 515. (c) Shot 476. (d) Shot 486. (e) Shot 488. The blemishes ahead of the bow shock waves in interferograms (a) and (b) are due to a flaw in the optical window.

4.3.2 Computational Mach-Zehnder Interferograms

A better comparison of the computed result with the experimental one is to construct the differential interferogram from the calculated flow field, using the computed density and composition and the known refractive indices of the components of the gas mixture. As mentioned in section 3.2, the computational differential interferogram is obtained by first calculating the infinite fringe Mach-Zehnder interferogram and subtracting from it a displaced copy of itself which then gives a double image of the boundaries, such as the body, of course, just as in the experimental differential interferogram. Figs. 4.35 to 4.37 show examples of computational infinite fringe Mach-Zehnder interferograms of nitrogen, air, and carbon dioxide, respectively. The density field for each case is also shown by the side of the computational Mach-Zehnder interferogram. As may be seen, a large number of fringes would be observed, so that even a relatively insensitive differential interferogram would give good quantitative resolution of the flow field.
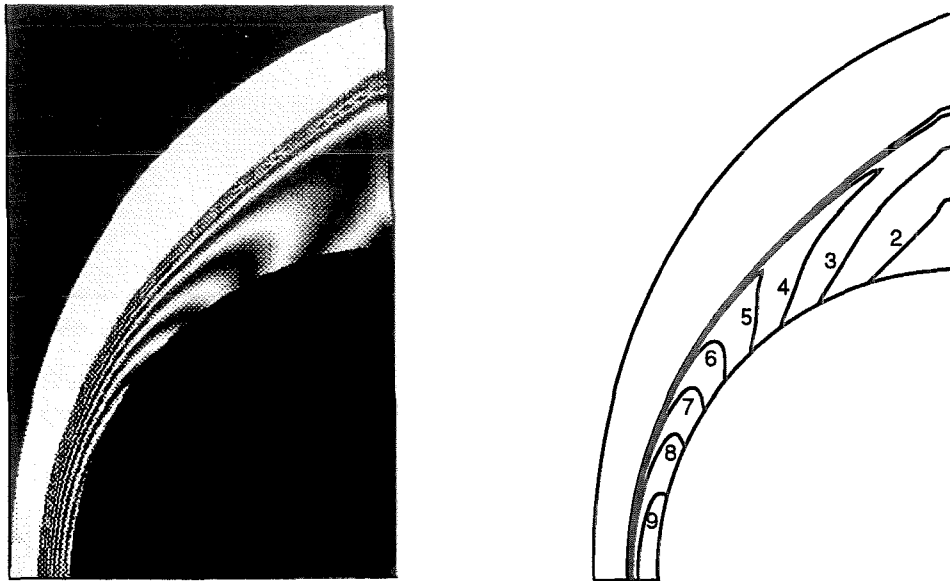
FIG. 4.35. Result of a computation of the flow field over a sphere for N_2. Freestream conditions are the same as Shot 181. LEFT: Infinite fringe Mach-Zehnder interferogram constructed from the numerical solution. RIGHT: Lines of constant density. The numbers on the plot indicate the density values as multiples of the freestream density. The border of the diagram on the right is the edge of the computational domain. The glitch at the right is an artifact of the interpolation routine.
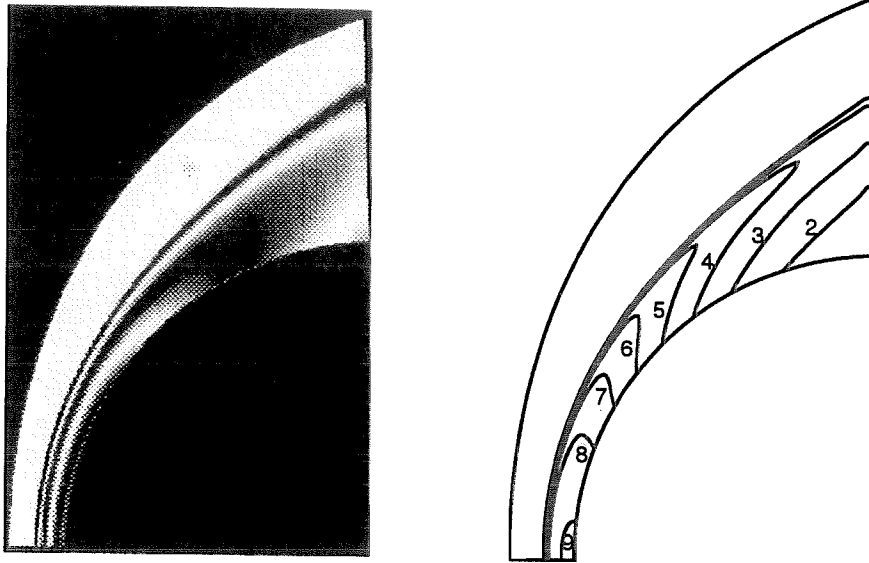
FIG. 4.36. Result of a computation of the flow field over a sphere for air. Freestream conditions are the same as Shot 491.
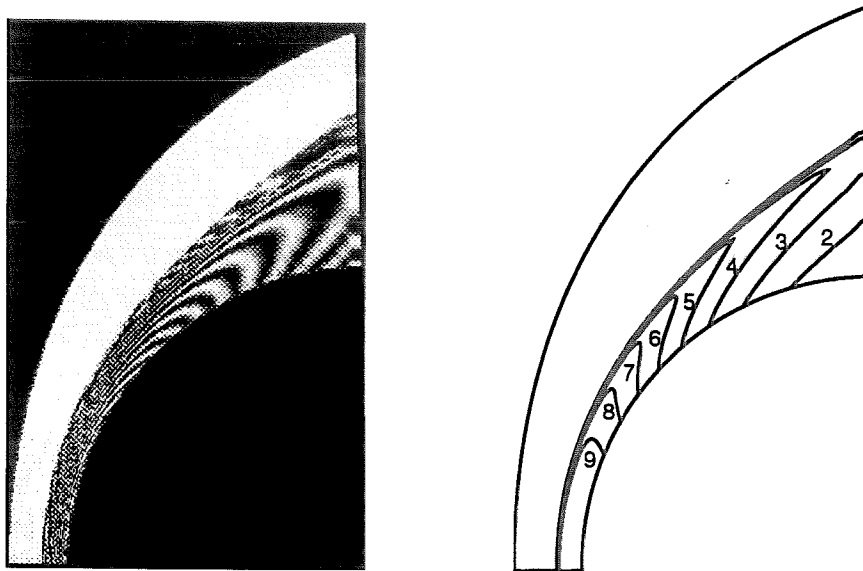
FIG. 4.37. Result of a computation of the flow field over a sphere for CO_2. Freestream conditions are the same as Shot 190.

4.3.3 Comparison of Experimental and Computational Differential Interferograms

Fig. 4.38 shows a computed differential interferogram for comparison with the measured one. As may be seen, the features of the photo are faithfully reproduced by the computation, both qualitatively and quantitatively. It should be noted that if the density of the computation is changed by 10%, this change can be resolved easily in the interferogram.
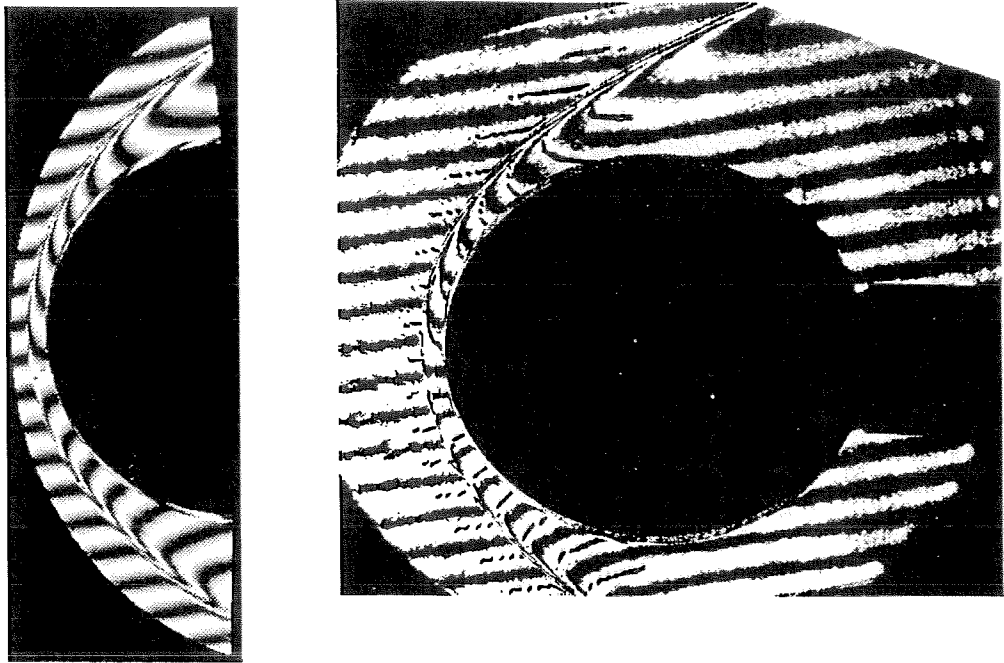
FIG. 4.38. Comparison of experimental and computed differential interferograms of nitrogen flow over a sphere, at the same conditions as those of Fig. 4.35. The photograph on the right is a finite-fringe differential interferogram of nitrogen flow over a sphere. The picture on the left is a corresponding computed interferogram at the same conditions as the experiment. Except for a slight difference in the vicinity of the shock, the two pictures are virtually congruent. To show this, a line along the center of the calculated white fringe is superimposed on the photograph.

To show other examples, Fig. 4.39 and Fig. 4.40 show similar exercises for an air flow and a carbon dioxide flow. Again, the comparison shows excellent agreement. Clearly, viscous effects are not important in the determination of the major features of the flow field.
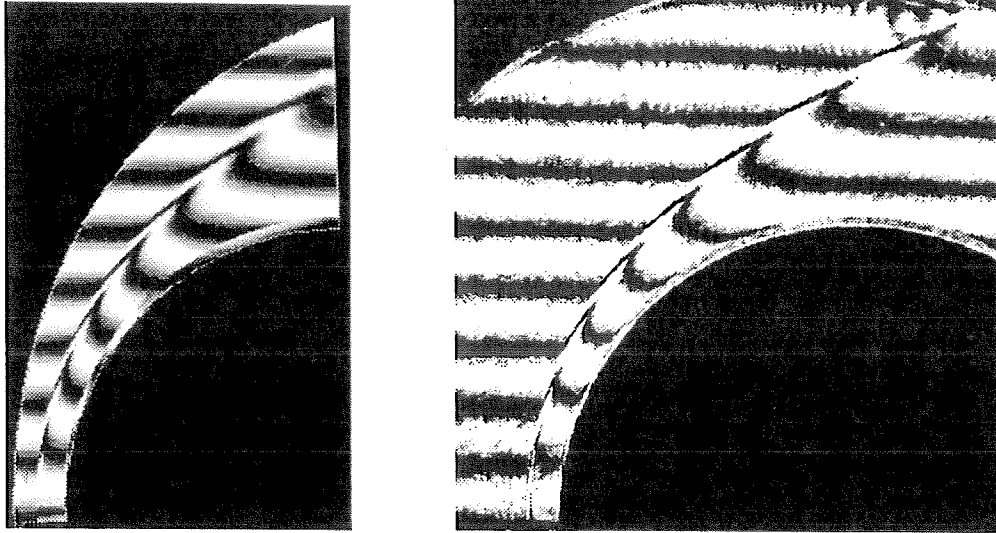
FIG. 4.39. Comparison of differential interferograms in the case of air flow over a sphere, at the same conditions as those of Fig. 4.36.
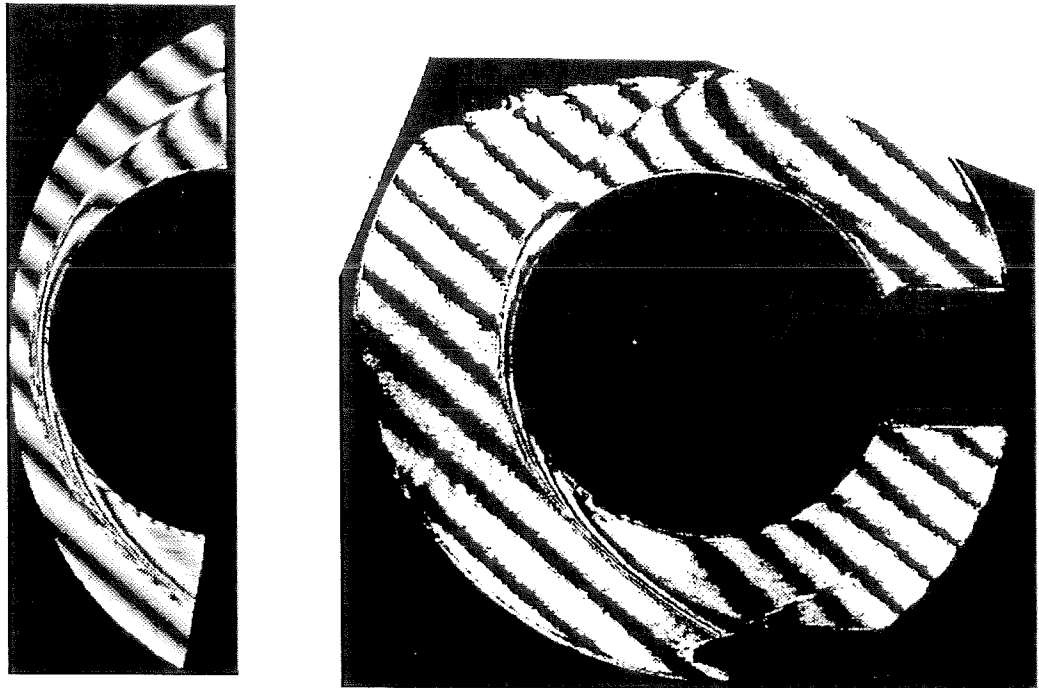
FIG. 4.40. Comparison of differential interferograms in the case of carbon dioxide flow over a sphere, at the same conditions as those of Fig. 4.37. In this case advantage has been taken of the symmetry of the flow to get both components of the gradient measured by the differential interferogram, by setting the angle of the fringes at 45 deg. in the freestream.

4.4 Chapter Summary

The free piston shock tunnel T5 was used to gather new data on hypervelocity dissociating flow and has extended the range of heat transfer measurements to freestream Reynolds number one million and stagnation enthalpy 22 MJ/kg. The experimental measurements of heat transfer rates over spheres for nitrogen, air, and carbon dioxide have been presented. Good agreement was observed among the measured stagnation point heat transfer rates, numerical computation results, and Fay and Riddell's theoretical predictions. This agreement provides another calibration of T5. For the cases of nitrogen and air, the measured heat flux distributions were also in reasonably good agreement with numerical computation results and Lees' theory for laminar flow. For the cases of carbon dioxide, some agreed and some did not. Early transition tripped by surface roughness is possibly responsible for the deviation of heat flux distribution from the theory. However, no definite conclusion can be drawn at this stage. A more carefully designed experiment is suggested to resolve this interesting phenomenon and to gain more knowledge about carbon dioxide dissociating flow.

The experimental results obtained by optical differential interferometry were compared with the images constructed from flowfields computed using the method of Candler. Good agreement of fringe pattern and shock shape was observed, which along with the agreement of heat transfer calculations with experimental data validate the computational method for the study of hypervelocity dissociating flow over blunt bodies. Computational interferometry also proved to be a useful tool to visualize the computational flow field and to have a direct comparsion of the computational flow field with the experimental one.

CHAPTER 5

Correlation between the Reaction Rate Parameter and the Stand-off Distance

In this chapter, an analytical solution is obtained for certain features of inviscid hyperve-
locity dissociating flow over spheres. The solution explains the correlation between the di-
mensionless stand-off distance and the dimensionless reaction rate parameter, Ω, previously
observed by Hornung (1972) for nitrogen. It is shown that the essence of the correlation is
what is known as "binary scaling". To generalize Hornung's correlation for more complex
gases than nitrogen, a new dimensionless reaction rate parameter is defined. Numerical
results based on the method of Candler show that this parameter correlates the stand-off
density product. Experimental results obtained by optical differential interferometry in T5
also confirm the new correlation.

5.1   Review of Hornung's Correlation

Consider steady flow over spheres at high Mach number and at such high velocity that
the ordered kinetic energy of the uniform freestream is comparable with the dissociation
energy of the gas. In the simplest case of dissociation of a single diatomic gas, this means
that a dimensionless number of the form

$$\mu \equiv \frac{M u_\infty^2}{R \theta_d} \tag{5.1}$$

has to be O(1).

In addition, the gas density is assumed to be large, so that the collision frequency be-
tween the molecules produces a dissociation rate that is fast enough to cause significant dis-
sociation over distances that are comparable with the radius of the sphere. In the simplest
case of dissociation of a single diatomic gas, where the composition may be characterized

by a single variable, *e.g.*, the dissociation fraction α, this means that a dimensionless number of the form

$$\Omega \equiv \left(\frac{d\alpha}{dt}\right)_{sh} \left(\frac{a}{u_\infty}\right) \tag{5.2}$$

has to be O(1). Here, the time derivative is the dissociation rate at a representative point, *e.g.*, just after the normal shock wave. High density is required to satisfy this condition because the dissociation rate is directly proportional to density. Clearly, this means that the product of density and body size must be sufficiently large. Hence, the Reynolds number of the flow is also large, and for many purposes the flow may be considered to be inviscid to very good approximation. Infinite Ω corresponds to such a fast reaction that the flow may be considered to be in equilibrium, while zero Ω corresponds to no dissociation, or the frozen limit. For given freestream conditions, the flow can be made to achieve a different degree of nonequilibrium by changing the size of the blunt body. If the radius of the sphere is small, Ω is consequently small and the flow rate is large compared with the chemical reaction rate. The flow is then close to the frozen limit. On the other hand, if the radius of the sphere is large such that the chemical reaction rate is much greater than the flow rate, the flow approaches the equilibrium limit and Ω is much larger than one.

A well-known feature of hypervelocity blunt-body flows is that the shock wave stand-off distance, Δ, is inversely proportional to the average density in the shock layer. This follows from a very simple argument which is presented here because it determines the correct dimensionless numbers to choose for the problem. Consider the control volume shown in Fig. 5.1. Apply continuity to this control volume. At the left, the rate at which mass enters the control volume is $u_\infty \rho_\infty b$ or $\pi u_\infty \rho_\infty b^2$, depending on whether the flow is axisymmetric or plane. For small b, the rate at which mass leaves the control volume is $u_b \bar{\rho} \Delta$ or $2\pi u_b b \bar{\rho} \Delta$, respectively, where $\bar{\rho}$ is the average density in the shock layer. With $u_b \simeq u_\infty \cos\phi$ and $b = r_{sh} \cos\phi$, mass balance gives

$$\frac{1}{2}\frac{\Delta}{r_{sh}}\frac{\bar{\rho}}{\rho_\infty} = \frac{1}{4}, \quad \text{and} = \frac{1}{2}, \tag{5.3}$$
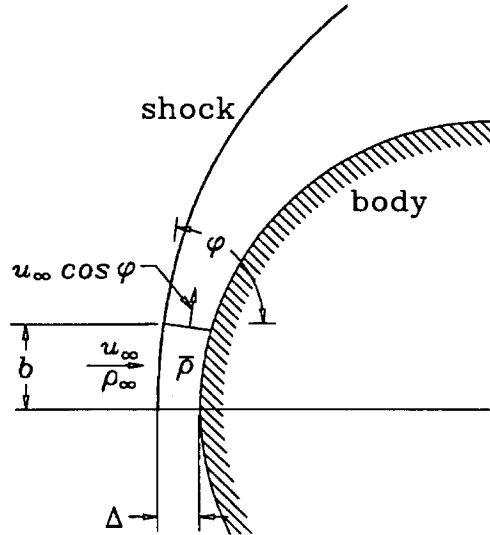
FIG. 5.1. Notation.

respectively, for axisymmetric and plane flow. Here, r_{sh} is the radius of curvature of the shock. Since the stand-off distance is small compared to the body radius, $a \simeq r_{sh}$ and the dimensionless parameter on the left may be formed with the body radius instead of the shock radius. The importance of this simple argument is not in the numbers on the right, but in the fact that it brings out the importance of the average density in the shock layer.

This topic was studied theoretically and experimentally in some detail by Hornung (1972). By examining a large number of numerical computations of dissociating nitrogen flow over cylinders, it was found that the dimensionless stand-off distance, in the form

$$\bar{\Delta} = \frac{1}{2} \frac{\Delta}{a} \frac{\rho_{sh}}{\rho_\infty} \, , \tag{5.4}$$

could be correlated by plotting it against the parameter Ω. Hornung also concluded that the computed density fields in the shock layer were also correlated well by Ω. However, the experimental results of this study did not corroborate the numerical correlation very well.

This earlier study suffered from two main problems. First, the theory was limited to a single diatomic gas, and did not account for the effect of μ (Eq. (5.1)) on $\bar{\Delta}$. No derivation of the correlation of $\bar{\Delta}$ with Ω was given. Second, the unavoidable end-effects in experimental studies of flow over cylinders manifest themselves in just the same manner

as nonequilibrium dissociation effects, so that the latter were obscured by them. Also, the facility employed probably suffered from driver-gas contamination at the highest specific enthalpies.

Therefore in the present study, we have the following three aims: perform a theoretical study to relate the stand-off distance to both Ω and μ; seek a more general reaction rate parameter, that allows the gas to consist of many species with many reactions; and test the results experimentally and numerically. In the experiments, the new facility T5, in which the density is significantly larger than was possible in T3 so that interferograms of flow over spheres give sufficient resolution, permitted the bothersome problems associated with flow over cylinders to be avoided. In the numerical investigation, the code developed by Candler (1988) was employed.

5.2 Theoretical Derivation

5.2.1 Conditions along the Stagnation Streamline

A. Effect of Chemical Reactions

Consider the stagnation streamline along the symmetry axis between the shock and the stagnation point. The momentum and energy equations for inviscid adiabatic flow take the simple forms

$$dp + \rho u\, du = 0 = dh + u\, du \ . \tag{5.5}$$

Thus,

$$dp = \rho\, dh \ . \tag{5.6}$$

This equation does not mean that the entropy is constant along the stagnation streamline, but rather that the only entropy change that occurs is that associated with the chemical reaction:

$$T\, ds = \sum_{i=1}^{n} \hat{\mu}_i\, dc_i \ , \tag{5.7}$$

where $\hat{\mu}_i$ and c_i are the chemical potentials and mass fractions of the constituents. Let the caloric equation of state be given in the form

$$h = h(p, \rho, c_i) .$$ (5.8)

Since the mass fractions must satisfy the identity

$$\sum_{i=1}^{n} c_i = 1 ,$$ (5.9)

the number of mass fractions that are independent is one less than the total number n of components present. It is usually convenient to choose c_1 as a dependent variable and the other c_i's as independent variables. Thus,

$$dh = h_\rho d\rho + h_p dp + \sum_{i=2}^{n} h_{c_i} dc_i = h_\rho d\rho + \rho h_p dh + \sum_{i=2}^{n} h_{c_i} dc_i$$ (5.10)

where the subscripts denote partial differentiation. Solving for $d\rho$,

$$d\rho = \frac{(1 - \rho h_p)}{h_\rho} dh - \frac{1}{h_\rho} \sum_{i=2}^{n} h_{c_i} dc_i .$$ (5.11)

Note that the coefficient of dh is related to the frozen speed of sound a_f , and that dh may be replaced by $-u\,du$. These may be used to rewrite the first term on the right of this equation, so that it becomes

$$\frac{d\rho}{\rho} = -\frac{u^2}{a_f^2} \frac{du}{u} - \frac{1}{\rho h_\rho} \sum_{i=2}^{n} h_{c_i} dc_i ,$$ (5.12)

where

$$a_f^2 = \frac{-h_\rho}{[h_p - 1/\rho]} .$$ (5.13)

The frozen Mach number after the normal shock is typically 0.2. This means that in the absence of dissociation, the density is practically constant along the stagnation streamline, and, with dissociation, the density change along the stagnation streamline is essentially controlled by the chemistry.

The local solution at the point just after the normal shock on the stagnation streamline is considered. Using the equation of contiunity, du/u in Eq. (5.12) may be replaced by $-d\rho/\rho$. This leads to the following simple relation for the density change associated with chemical reaction at the point just after the shock on the stagnation streamline:

$$(d\rho)_{sh} = -\left(\frac{1}{h_\rho[1 - \frac{u^2}{a_f^2}]}\right)_{sh} \left(\sum_{i=2}^{n} h_{c_i} dc_i\right)_{sh} . \qquad (5.14)$$

We now also assume that the gas obeys the ideal-gas thermal equation of state

$$T = T(p, \rho, c_i) = \frac{p}{\rho R \Gamma} , \qquad (5.15)$$

where

$$\Gamma = \sum_{i=1}^{n} \frac{c_i}{M_i} = \frac{1}{M} , \qquad (5.16)$$

and, M_i and M are the molecular weights of species i and the dissociated gas mixture, respectively. Thus,

$$h_\rho = \frac{\partial h(p, T, c_i)}{\partial T} T_\rho = -\frac{c_p p}{\rho^2 R \Gamma} , \qquad (5.17)$$

$$h_p = \frac{\partial h(\rho, T, c_i)}{\partial T} T_p = \frac{c_p}{\rho R \Gamma} , \qquad (5.18)$$

and

$$h_{c_i} = \frac{\partial h(p, \rho, T)}{\partial T} T_{c_i} = (h_i - h_1) - \frac{c_p p}{\rho R \Gamma^2}(\frac{1}{M_i} - \frac{1}{M_1}) . \qquad (5.19)$$

c_p is the specific heat at constant pressure of the gas mixture and is given by

$$c_p = \sum_{i=1}^{n} c_i c_{pi} , \qquad (5.20)$$

where the c_{pi} are the specific heats at constant pressure of the constituents. This yields

$$a_f^2 = \frac{c_p}{c_p - R \Gamma} \frac{p}{\rho} \qquad (5.21)$$

for the frozen speed of sound and Eq. (5.14) can be written as follows:

$$
(d\rho)_{sh} = \left(\frac{\rho \sum_{i=2}^{n} h_{c_i} dc_i}{u^2[1 + \frac{M}{R}(\frac{p}{\rho u^2} - 1)c_p]} \right)_{sh}
$$

$$
= \frac{\rho_{sh}^3 \left(\sum_{i=2}^{n} h_{c_i} dc_i \right)_{sh}}{\rho_{\infty}^2 u_{\infty}^2 \left[1 + \frac{Mc_{p_{sh}}}{R} \left(\frac{\rho_{sh}}{\rho_{\infty}} - 2 \right) \right]} .
$$

(5.22)

The boundary conditions on the shock have been used in Eq. (5.22) and are determined from the conservation of energy, momentum, and mass across the shock:

$$
h_\infty + \frac{1}{2}u_\infty^2 = h_{sh} + \frac{1}{2}u_{sh}^2 ,
$$

$$
p_\infty + \rho_\infty u_{n\infty}^2 = p_{sh} + \rho_{sh}u_{nsh}^2 ,
$$

(5.23)

$$
\rho_\infty u_{n\infty} = \rho_{sh}u_{nsh} ,
$$

where the subscript n refers to components normal to the shock. Since the flow is hypersonic, p_∞ has been neglected in Eq. (5.22).

B. Density Profile

Fig. 5.2 shows seven density profiles along the stagnation streamline obtained using Candler's inviscid code plotted against y/Δ, where y is the distance from the shock. The freestream conditions for these different profiles were the same, and the changes are brought about by successively increasing the sphere diameter. As may be seen, the profile changes in a monotonic fashion from the frozen-flow profile, with virtually constant density, to the equilibrium profile, in which all the dissociation, and therefore all the density change, occurs in the shock, and the density is again virtually constant thereafter.

Recall that the quantity that determines the stand-off distance is the average density, see Eq. (5.3). In fact, numerous correlations of stand-off distance with average density have been made for non-reacting flow. Upon interpretation into our variables, these give

the following result:

$$\frac{1}{2}\frac{\Delta}{a}\frac{\bar{\rho}}{\rho_\infty} = L \, ,$$ (5.24)

where $L = 0.41$ for spheres, see *e.g.*, Ambrosio and Wortmann (1962).
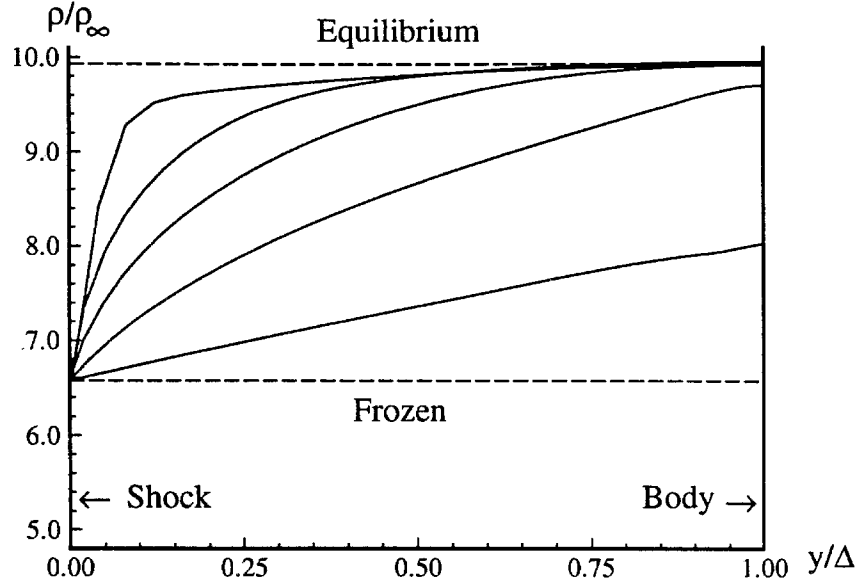
FIG.5.2. Plot of density profiles on stagnation streamlines of spheres for equilibrium, frozen, and nonequilibrium flows. The five intermediate density profiles represent flow over spheres of five different radii of 0.025, 0.25, 1, 3, and 60 in., with the same freestream conditions: u_∞=5.2 km/s, ρ_∞=0.0443 kg/m^3, T_∞=2300 K and α_∞=0.0156.

Because the stand-off distance is related to the average density, the exact details of the density profile are not important and we can proceed in an approximate Kármán-Pohlhausen-type analysis by assuming linear density profiles between the shock and the body, provided that the density on the body ρ_b is smaller than the equilibrium density ρ_e. If the linear profile reaches ρ_e before the stagnation point, the density is taken to be constant thereafter at ρ_e. This clearly requires the equilibrium density to be determined and is evidently the place where the dependence of $\bar{\Delta}$ on μ enters.

To proceed with the analysis, distinguish the cases where $\rho_b < \rho_e$ from those in which the body density is ρ_e. The slope of the density profile at the shock is determined from the dissociation rate just downstream of the shock. Fig. 5.3 shows the simplified linear profiles.
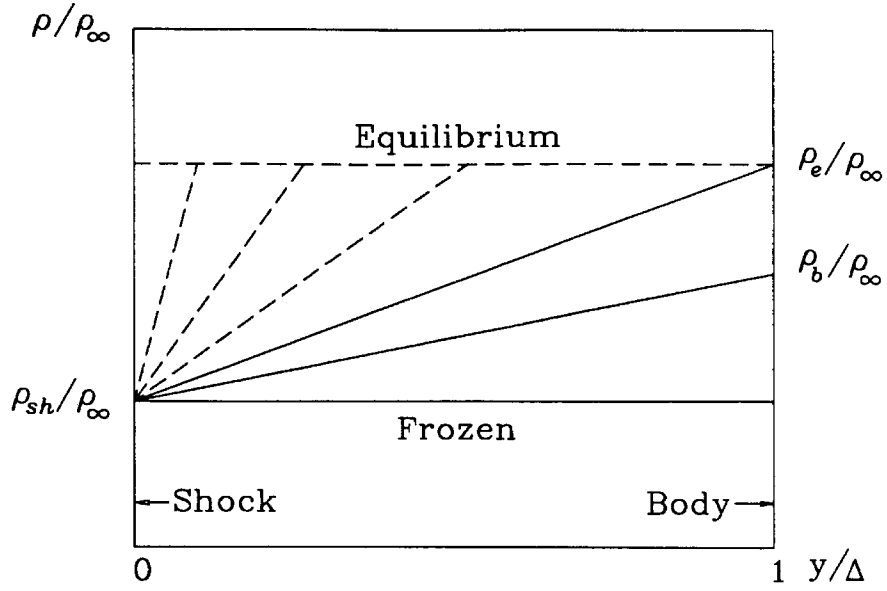
FIG. 5.3. Sketch of modelled linear density profiles on the stagnation streamlines. On the frozen side, $\rho_b < \rho_e$. On the equilibrium side, $\rho_b = \rho_e$ before $y/\Delta = 1$. The dividing case is where $\rho_b = \rho_e$ at $y/\Delta = 1$. ρ_b and ρ_e denote the stagnation point density and the equilibrium density, respectively.

5.2.2 Analytic Solution for the Correlation

A. Frozen-Side Solution

In cases where $\rho_b < \rho_e$, the linear profiles give

$$\left(\frac{d\rho}{dy}\right)_{sh} = \frac{\rho_b - \rho_{sh}}{\Delta} \, , \quad \text{and} \quad \bar{\rho} = \frac{1}{2}(\rho_b + \rho_{sh}) \, , \qquad (5.25)$$

where the subscript sh denotes values just after the shock, as before. $(d\rho/dt)_{sh}$ can then be approximated as

$$\left(\frac{d\rho}{dt}\right)_{sh} = u_{sh}\left(\frac{d\rho}{dy}\right)_{sh} = (\rho_b - \rho_{sh})\left(\frac{\rho_\infty}{\rho_{sh}}\frac{a}{\Delta}\right)\left(\frac{u_\infty}{a}\right) \, . \qquad (5.26)$$

Using Eq. (5.26), Eq. (5.14) can be regrouped as

$$\bar{\Delta} = \frac{\dfrac{\rho_b}{\rho_{sh}} - 1}{K\Omega} \, ,$$ (5.27)

where

$$K = -2\left(\frac{\displaystyle\sum_{i=2}^{n} h_{c_i}}{\rho h_\rho [1 - \dfrac{u^2}{a_f^2}]}\right)_{sh} = \frac{2\rho_{sh}^2 \left(\displaystyle\sum_{i=2}^{n} h_{c_i}\right)_{sh}}{\rho_\infty^2 u_\infty^2 \left[1 + \dfrac{M c_{p_{sh}}}{R}\left(\dfrac{\rho_{sh}}{\rho_\infty} - 2\right)\right]} \, ,$$ (5.28)

and

$$\Omega = \left(\frac{\displaystyle\sum_{i=2}^{n} h_{c_i}\dfrac{dc_i}{dt}}{\displaystyle\sum_{i=2}^{n} h_{c_i}}\right)_{sh}\left(\frac{a}{u_\infty}\right) \, .$$ (5.29)

Note that Eq. (5.22) has also been used to obtain Eq. (5.28) and in the simplest case of dissociation of a single diatomic gas, $e.g.$, nitrogen, where the composition may be characterized by a single variable α, this generalized definition of Ω includes the variable of the same name defined by Hornung (see Eq. (5.2)) as a special case.

Using Eq. (5.24), the stagnation-point density is given by

$$\frac{\rho_b}{\rho_{sh}} = \frac{2L}{\bar{\Delta}} - 1 \, .$$ (5.30)

Substituting Eq. (30) into Eq. (5.27) results in

$$\bar{\Delta}^2 - (L - \bar{\Delta})\frac{2}{K\Omega} = 0 \, .$$ (5.31)

This quadratic equation can be solved for $\bar{\Delta}$:

$$\bar{\Delta} = -\frac{1}{K\Omega} + \left((\frac{1}{K\Omega})^2 + \frac{2L}{K\Omega}\right)^{\frac{1}{2}} \, .$$ (5.32)

The other root of Eq. (5.32) has been discarded because it is negative and is not physically possible. The form of this equation suggests that $K\Omega$ would be a better parameter than Ω to correlate $\bar{\Delta}$.

B. Equilibrium-Side Solution

For equilibrium-side density profiles,

$$\left(\frac{d\rho}{dy}\right)_{sh} = \Upsilon\left(\frac{\rho_e - \rho_{sh}}{\Delta}\right) \quad \text{for } y < y_i < 1 ,$$

and
(5.33)

$$\rho = \rho_e \qquad \text{for } y \geq y_i ,$$

where Υ is a density slope parameter at the shock and y_i is the intersection point of the linear density profile with the uniform density profile. Υ is greater than one and y_i is equal to Δ/Υ. The average density $\bar{\rho}$ for this ramp-like density profile is

$$\bar{\rho} = \frac{1}{2\Upsilon}[(2\Upsilon - 1)\rho_e + \rho_{sh}] .$$
(5.34)

Substituting $\bar{\rho}$ into Eq. (5.24),

$$\bar{\Delta} = \frac{2\Upsilon L}{1 + (2\Upsilon - 1)(\frac{\rho_e}{\rho_{sh}})} .$$
(5.35)

For given freestream conditions, ρ_e/ρ_∞ is a constant and can be obtained by using the equilibrium normal-shock solution. The density slope parameter Υ is the only controlling variable for the problem. The corresponding Ω for a known $\bar{\Delta}$ will be given by Eq. (5.26) as

$$\Omega = \frac{\Upsilon(\frac{\rho_e}{\rho_{sh}} - 1)}{K}\bar{\Delta}^{-1} .$$
(5.36)

Note that in the limit of equilibrium flow, Υ will approach infinity and $\bar{\Delta}$ will have a equilibrium value of $(\rho_{sh}/\rho_e)L$ (see Eq. (5.35)). Again, the appearance of $K\Omega$ together indicates that this rather than Ω is the proper parameter to correlate $\bar{\Delta}$.

C. The Dividing Point

The solution for the dividing case can be obtained by letting Υ be equal to one in the equilibrium-side solution. $\bar{\Delta}$ and Ω for the dividing case become

$$\bar{\Delta}_d = \frac{2L}{1 + \dfrac{\rho_e}{\rho_{sh}}} \quad \text{and} \quad \Omega_d = \frac{(\dfrac{\rho_e}{\rho_{sh}} - 1)}{K} \bar{\Delta}_d^{-1} \ , \tag{5.37}$$

where subscript d denotes the values of the dividing case.

For simplicity, we will proceed in further theoretical analyses with the simplest case of a pure dissociating diatomic gas, $e.g.$, nitrogen. The ideal dissociating gas model introduced by Lighthill (1957) for equilibrium flow and Freeman (1958) for nonequilibrium flow will be employed in this work to represent nitrogen. A brief review of the ideal dissociating gas model will be given in the next section.

5.2.3 Lighthill-Freeman Ideal Dissociating Gas (IDG)

A. Equations of State and Reaction-Rate Equation

According to Lighthill, the law of mass action for the IDG model may be written as

$$\frac{\alpha^2}{1 - \alpha} = \frac{\rho_d}{\rho} \exp\left(-\frac{\theta_d}{T}\right) \ , \tag{5.38}$$

where θ_d and ρ_d are the characteristic temperature and characteristic density. $\theta_d = 113200$ K and $\rho_d = 130 \times 10^3$ kg/m^3 are recommended by Lighthill. ρ_d represents a combination of terms in the partition functions for N and N$_2$ and is taken by Lighthill to be constant. It turns out that the assumption that ρ_d is constant is equivalent to representing the sum of

the equilibrium values of energy of electronic and vibrational excitation by the energy of a single degree of freedom for the diatomic species which is fully excited at all temperatures. In other words, the IDG in the undissociated state is like a diatomic gas, whose vibrational mode is "half-excited".

The equation of state for a mixture of molecular and atomic nitrogen is

$$p = \rho(1+\alpha)\frac{R}{M_{N_2}}T \; . \tag{5.39}$$

The specific enthalpy for IDG is given by

$$h = \frac{4+\alpha}{1+\alpha}\frac{p}{\rho} + \alpha\left(\frac{R\theta_d}{M_{N_2}}\right) \; . \tag{5.40}$$

Eq. (5.40) and Eq. (5.13) then yield a simple expression for the frozen speed of sound:

$$a_f^2 = \frac{4+\alpha}{3}\frac{p}{\rho} \; . \tag{5.41}$$

The effective value of the ratio of specific heats of a frozen IDG is seen to be $(4+\alpha)/3$.

The rate equation giving the combined rate of production of dissociated nitrogen for the reaction in Eq. (3.20) may be written in terms of the degree of dissociation, and is (see Vincenti and Kruger, 1965, p. 232)

$$\frac{d\alpha}{dt} = \frac{\rho}{M_{N_2}}[2\alpha\,k_{f,1} + (1-\alpha)\,k_{f,2}]\left\{(1-\alpha) - \frac{4\rho\alpha^2}{M_{N_2}K_c}\right\} \; , \tag{5.42}$$

where K_c is the equilibrium constant of reaction, and $k_{f,1}$ and $k_{f,2}$ are the forward reaction rate constants for the reaction with the collision partners N and N_2, respectively. From Eq. (5.38), the equilibrium constant for the IDG model based on a molar concentration is defined by

$$K_c = \frac{4\rho_d}{M_{N_2}}\exp\left(-\frac{\theta_d}{T}\right) \; . \tag{5.43}$$

Freeman (1958) described the square bracket in Eq. (5.42) in the following form

$$2\alpha\, k_{f,1} + (1 - \alpha)\, k_{f,2} = M_{N_2}\, C\, T^\eta \exp\left(-\frac{\theta_d}{T}\right) \; ; \tag{5.44}$$

thus incorporating the two components of reaction rate into one constant C. This, however, is not a serious restriction in view of the uncertainty associated with experimental data on reaction rates for nitrogen. The reaction rate for a nonequilibrium IDG flow then becomes

$$\frac{d\alpha}{dt} = C\, \rho\, T^\eta \left\{ (1 - \alpha) \exp\left(\frac{-\theta_d}{T}\right) - \alpha^2\, \frac{\rho}{\rho_d} \right\} \; . \tag{5.45}$$

B. Shock Equations for IDG

Using Eq. (5.23) and Eq. (5.40), the specific enthalpy h at the shock then becomes

$$\frac{M_{N_2} h_s}{R\theta_d} = (4 + \alpha_\infty)\frac{T_\infty}{\theta_d} + \frac{M_{N_2} u_\infty^2}{2R\theta_d} \sin^2\phi + \alpha_\infty \; , \tag{5.46}$$

where ϕ is the angle between the freestream and the shock, and the component of velocity normal to the shock has been neglected. The temperature may now be obtained as an explicit function of α and freestream conditions, for a given streamline defined by the value of ϕ at which the streamline crossed the shock, by using Eq. (5.40) and Eq. (5.46):

$$\frac{T}{\theta_d} = \frac{1}{4 + \alpha} \left[(4 + \alpha_\infty)\frac{T_\infty}{\theta_d} + \frac{\mu}{2}(1 + \alpha)\sin^2\phi - (\alpha - \alpha_\infty) \right] \; , \tag{5.47}$$

where μ is the dimensionless parameter defined in Eq. (5.1).

Eq. (5.47) and Eq. (5.39) then yield a similar expression for the density:

$$\frac{\rho}{\rho_\infty} = \frac{p\mu}{\rho_\infty u_\infty^2} \frac{\theta_d}{T} \; . \tag{5.48}$$

The temperature and density immediately behind the normal shock may now be expressed in terms of the freestream conditions from Eq. (5.47) and Eq. (5.48) with $\phi = \pi/2, \alpha = \alpha_\infty$, and $p_{sh}/\rho_\infty u_\infty^2 = 1$ as

$$\frac{T_{sh}}{\theta_d} = \frac{T_\infty}{\theta_d} + \frac{\mu}{2}\frac{1 + \alpha_\infty}{4 + \alpha_\infty} \; , \quad \text{and} \quad \frac{\rho_{sh}}{\rho_\infty} = \frac{\theta_d}{T_{sh}}\mu \; . \tag{5.49}$$

Thus the dissociation rate Eq. (5.45) at the shock can also be written in terms of freestream conditions directly.

$$\left(\frac{d\alpha}{dt}\right)_{sh} = \Lambda(1 - \alpha_\infty) \left[\frac{T_\infty}{\theta_d} + \frac{\mu}{2}\frac{1 + \alpha_\infty}{4 + \alpha_\infty}\right]^{\eta - 1} \exp\left[\left(-\frac{T_\infty}{\theta_d} - \frac{\mu}{2}\frac{1 + \alpha_\infty}{4 + \alpha_\infty}\right)^{-1}\right] \;,\quad (5.50)$$

where Λ is the dimensionless parameter $aC\rho_\infty\theta_d^\eta/u_\infty$ and the recombination rate has been neglected. It is well known that at the shock where the temperature is high, the dissociation rate dominates the recombination rate. For given freestream conditions, ρ_e/ρ_∞ is also a constant and can be obtained by using the iteration technique of the normal-shock solution described by Freeman (1958) for an ideal dissociating gas.

5.2.4 Analytic Solution for Nitrogen Using IDG Model

As mentioned previously, the dissociation of nitrogen can be characterized by a single variable, i.e., the dissociation fraction α. Thus, $\sum h_{c_i}$ becomes h_α. By substituting the relevant derivatives of h (see Eq. (5.40)) and a_f (Eq.(5.41)) of the IDG into Eq. (5.28), the coefficient K becomes

$$K = \frac{2\left[\dfrac{1}{\mu(1 + \alpha_\infty)}\left(\dfrac{\rho_{sh}}{\rho_\infty}\right)^2 - \dfrac{3}{(1 + \alpha_\infty)^2}\left(\dfrac{\rho_{sh}}{\rho_\infty} - 1\right)\right]}{\left[1 + \left(\dfrac{4 + \alpha_\infty}{1 + \alpha_\infty}\right)\left(\dfrac{\rho_{sh}}{\rho_\infty} - 2\right)\right]} \;.\quad (5.51)$$

The boundary condition for α at the shock is taken to be $\alpha_{sh} = \alpha_\infty$ and K is then a funtion of freestream conditions only.

From Eq. (5.49) and Eq. (5.51), it is clear that K is a strong function of μ, and, for given freestream conditions, the relation between Ω (Eq. (5.2)) and $\bar{\Delta}$ (Eq. (5.4)) can be solved analytically for nitrogen by using Eq. (5.32), Eq. (5.35), and Eq. (5.36).

5.3 Results and Discussion

In this section, the correlation of the numerical results obtained by Candler's inviscid code is compared with the analytic solutions and the experimental data obtained by optical differential interferometry in T5. A more general reaction rate parameter, that allows the gas to consist of many species with many reactions, is also presented.

The stand-off distance Δ and the shock values of the reaction rate $(d\alpha/dt)_{sh}$ and density ρ_{sh} for the numerical calculation are determined from the point where the vibrational temperature reaches a maximum. For the purposes of presenting the experimental results on the stand-off distance, the shock density ratio and the reaction rate at the shock were calculated using Eq. (5.49) and Eq. (5.50) for nitrogen, and Candler's inviscid method for air and carbon dioxide. The stand-off distance was measured from the experimental pictures.

5.3.1 Comparision of Analytical, Numerical, and Experimental Results for Nitrogen

Fig. 5.4 shows the analytic solutions of four different freestream conditions as a plot of the dimensionless stand-off distance $\bar{\Delta}$ and the dimensionless reaction rate Ω. The values of μ, u_∞, T_∞, ρ_∞, α_∞, and h_0 are given in Table 5.1. As may be seen in Fig. 5.4, the four solutions have different equilibrium limits of dimensionless stand-off distance $\bar{\Delta}$ and they tend to reach equilibrium at different values of the reaction rate parameter Ω.

Line type	μ	u_∞(km/s)	T_∞(K)	ρ_∞(kg/m^3)	α_∞	h_0(MJ/kg)
Long dashed	0.5	4.1	950	0.06	0.0007	9.90
dash-dot-dot	0.8	5.2	2300	0.0443	0.0156	16.9
dash-dot	1.0	6.1	3900	0.033	0.082	26.4
solid	1.2	7.0	5260	0.025	0.201	38.2

Table 5.1. Freestream conditions used to calculate the analytic solutions in Fig. 5.4
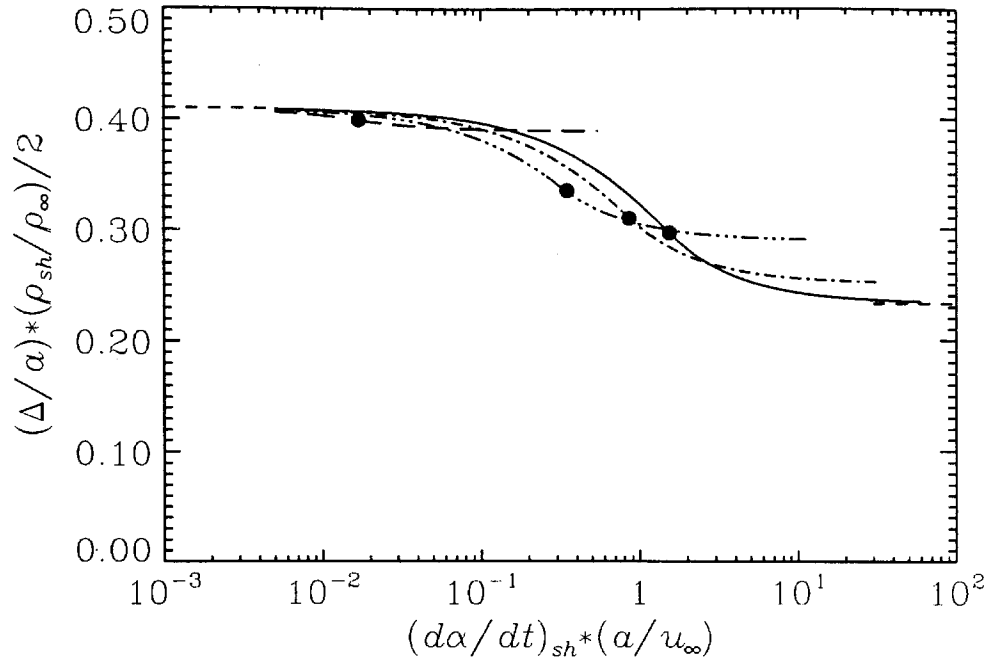
FIG. 5.4. Analytic solutions obtained using Eq. (5.32), Eq. (5.35), Eq. (5.36), and Eq. (5.37) for nitrogen. The freestream conditions for analytical solutions are given in Table 5.1. The abscissa is the reaction rate parameter, defined as the dissociation rate immediately after the shock scaled by sphere radius and flow speed. The ordinate is the dimensionless stand-off distance scaled by the density ratio at the shock. The filled circular symbols on the analytical curves are the points of dividing cases.

Fig. 5.5 shows the results of sixty-five calculations of nitrogen flow over spheres superimposed on Fig. 5.4, the ranges of values of μ, u_∞, α_∞, T_∞, ρ_∞, and a being given in Table 5.2. The only chemical reactions in the flow are those for nitrogen dissociation (Eq. (3.20)). Good correlation between two parameters has been observed as Hornung (1972) has shown with the one-temperature inverse method, and the theoretical curves predict the numerical correlation quite well. Also shown in Fig. 5.5 are the experimental results. The range of values of reservoir and freestream conditions chosen for the experiments is listed in Table 2.3. The experimental data agree well with the correlation of the numerical results. The correlation between the density stand-off product $\bar{\Delta}$ and the dimensionless reaction rate $\bar{\Omega}$ happens to be a collection of nonequilibrium regions for different freestream conditions. $\bar{\Delta}$ starts from the frozen limit, decreases as $\bar{\Omega}$ increases, and eventually approaches the equilibrium limit asymptotically. The reaction rate parameter can be varied at given

freestream conditions by adjusting the radius of the model. As the radius of a sphere increases without changing the freestream conditions, Ω increases. The flow rate becomes smaller and smaller compared to the chemical reaction rate which is a constant for given free stream conditions. The flow will then moves from the frozen limit to the equilibrium limit. Fig. 5.2 demonstrates this feature.

parameter	μ	u_∞(km/s)	T_∞(K)	ρ_∞(kg/m^3)	α_∞	h_0(MJ/kg)	a(m)
from	0.5	4.0	900	0.0036	0.0007	9.85	0.00635
to	1.2	7.0	5260	0.06	0.35	38.1	0.0762

Table 5.2. Range of values of parameters covered in calculation by Candler's method for nitrogen.
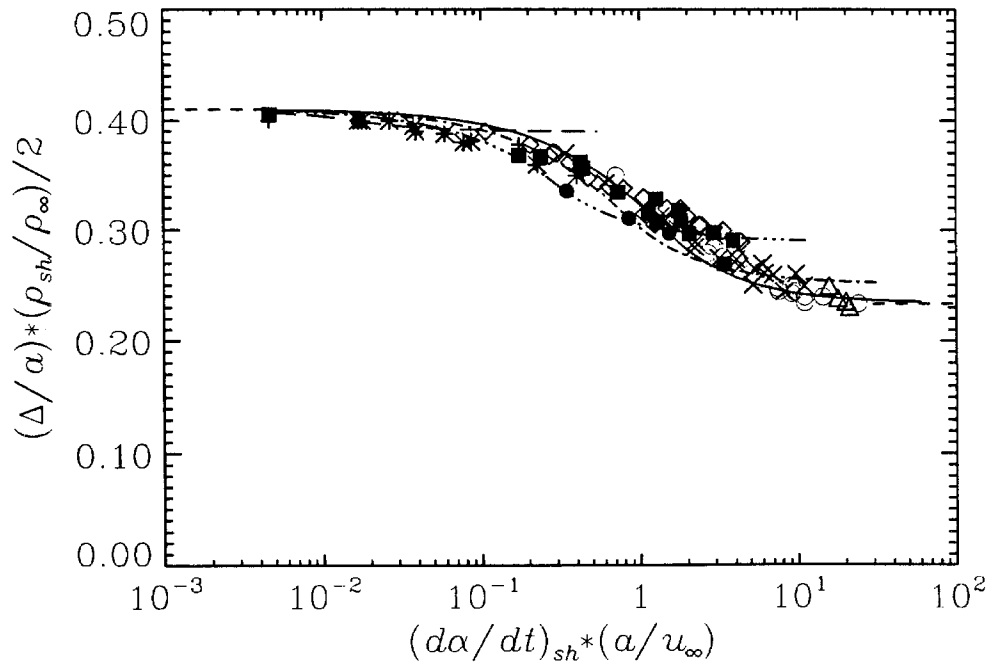
FIG. 5.5. Comparison of the numerical correlation, analytical solutions, and experimental results. The filled square symbols in this diagram represent experimental results in T5, while the open symbols are computational results. The lines shown are for analytic solutions in Fig. 5.4. The filled circles again show the dividing points in the analytic results.

The density patterns of the six selected cases are plotted next to each other in ascending order of Ω in Fig. 5.6. The density pattern is very sensitive to the dissociation rate.

$\Omega=0.00371$ $\qquad$ $\Omega=0.0371$ $\qquad$ $\Omega=0.371$

$\Omega=1.485$ $\qquad$ $\Omega=4.455$ $\qquad$ $\Omega=89.1$
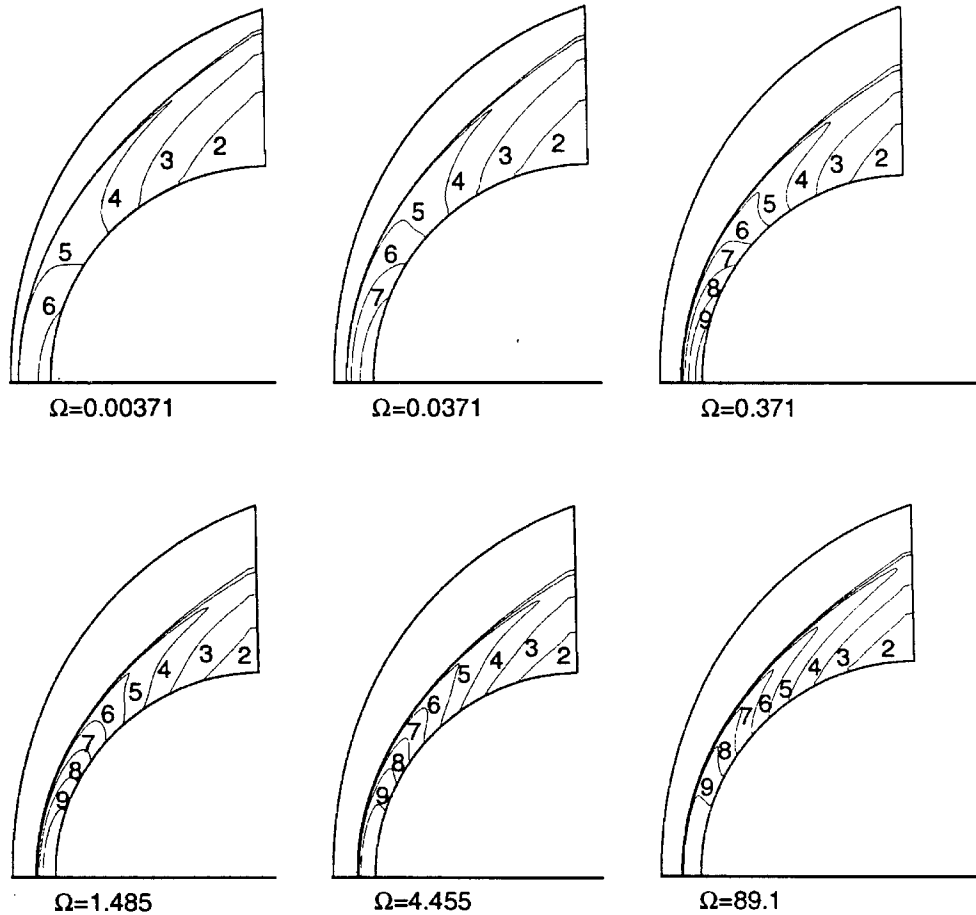
Fig. 5.6. Density fields for flow over a sphere as calculated by Candler's method. Freestream conditions as for Fig. 5.2. The radii of the spheres are 0.0025, 0.025, 0.25, 1, 3, 60 in.

It should be pointed out that the different equilibrium limits of $\bar{\Delta}$ expected for different freestream conditions are not clearly evident in the computational and experimental results shown in Fig. 5.5, because the correlation with Ω moves the curves to the left as the total enthalpy is decreased. The analytical plots of Fig. 5.4 also exhibit this phenomenon which will be discussed further.
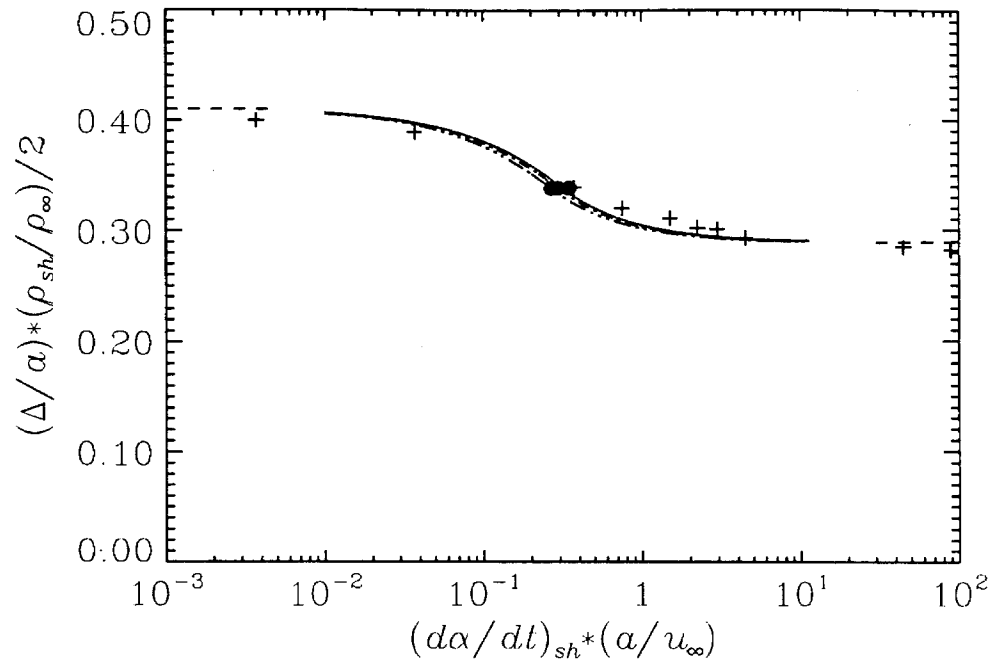
FIG. 5.7. Analytic solutions of three different freestream conditions with the same specific reservoir enthalpy, h_0=16.9 MJ/kg. Freestream conditions as for Table 5.3.. The cross symbols represent computational results using Candler's method of flows over spheres of radii 0.0025, 0.025, 0.25, 1, 1.5, 2, 3, 30, and 60 in. with the same free stream conditions as the first one in Table 5.3.

Fig. 5.7 shows the analytic solutions of three different freestream conditions with the same specific reservoir enthalpy, 16.9 MJ/kg. The freestream conditions are listed in Table 5.3. The three solutions are almost identical. From Eq. (5.49), the shock temperature and shock density ratio are funtions of freestream velocity, temperature, and dissociation fraction only. If the three freestream parameters are fixed, K in Eq. (5.51) will be fixed too. The ratio of equilibrium density to free stream density is also a function of freestream velocity, temperature and dissociation fraction only. So, from Eq. (5.32), Eq. (5.35), and Eq. (5.36), the correlation curves will be exactly identical if the three freestream parameters are kept the same. A closer look at K in Eq. (5.51), indicates that the first term in the numerator is an order of (ρ_{sh}/ρ_∞) higher than the second term. Together with Eq. (5.49), it is clear that K is a strong function of freestream velocity (μ) and a weak function of freestream temperature and dissociation fraction. Note that the freestream temperature term

in the shock temperature equation (Eq. (5.49)) is usually much smaller than the freestream velocity term (μ term) in hypervelocity nonequilibrium flow because the kinetic energy of the freestream is usually much larger than its internal thermal energy. The deviation in Fig. 5.7 between the three freestream conditions is due to the minor influences from the different freestream temperatures and dissociation fractions. Also shown in Fig. 5.7 are the computational results of the six cases in Fig. 5.6, and four more cases of spheres of radii 0.5, 1.5, 2.0 and 30 in. with the same freestream conditions as Fig. 5.6. Note that the first freestream condition in Table 5.3 is the same as that of Fig. 5.6.

parameter	μ	u_∞(km/s)	T_∞(K)	ρ_∞(kg/m^3)	α_∞	h_0(MJ/kg)
solid	0.80	5.2	2300	0.0443	0.0156	16.9
dash-dot	0.75	5.1	2100	0.019	0.0315	16.9
dash-dot-dot	0.70	5.0	1690	0.0065	0.0627	16.9

Table 5.3. Freestream conditions used to calculate the analytical solutions in Fig. 5.7.

Fig. 5.8 shows another example of three different freestream conditions with the same specific reservoir enthalpy, 38.1 MJ/kg. The freestream conditions are listed in Table 5.4. Again, the agreement is good. The larger freestream temperature difference between the three cases causes a larger deviation of the correlation curves than the previous example in Fig. 5.7.

parameter	μ	u_∞(km/s)	T_∞(K)	ρ_∞(kg/m³)	α_∞	h_0(MJ/kg)
solid	1.2	7.0	5260	0.025	0.201	38.1
dash-dot	1.1	6.9	4110	0.011	0.265	38.1
dash-dot-dot	1.0	6.7	2780	0.0036	0.35	38.1

Table 5.4. Freestream conditions used to calculate the analytical solutions in Fig. 5.8
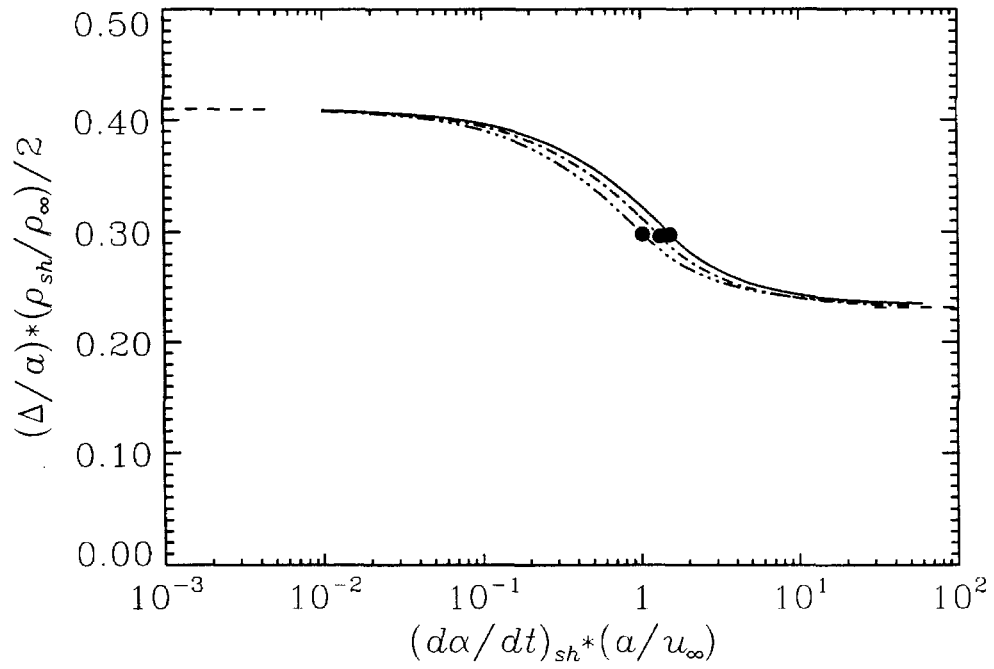
FIG. 5.8. Analytic solutions of three different freestream conditions with the same specific reservoir enthalpy, h_0=38.1 MJ/kg. Freestream conditions as for Table 5.4.

Gibson and Marrone (1964) have introduced the concept of binary scaling for nonequilibrium flows involving reactions with two-body molecular collisions. Binary scaling means that, for two different flows with the same freestream velocity, temperature, and dissociation fraction but different values of the freestream density and body radius, the nonequilibrium flowfields with x and y scaled by the radius a will be the same if the product $\rho_\infty a$ is the same between the two flows. It has been shown that the forward reaction rate (the dissociation rate) dominates the backward reaction rate (the recombination rate) at the shock and the forward reaction rate is proportional to the freestream density ρ_∞. Ω is then proportional to the binary scaling parameter $(\rho_\infty a / u_\infty)$ implicitly. The essence of the correlation between the dimensionless stand-off distance $\bar{\Delta}$ and the dimensionless reaction rate Ω is clearly recognized to be the binary scaling from Figs. 5.7 and 5.8.

One other interesting feature in Fig. 5.4 that should be pointed out is that for the two high enthalpy cases (h_0=26.4 and 38.1 MJ/kg), the two correlation curves are very similar to each other. This similarity may be the reason that the density pattern of nonequilibrium dissociating flow can be correlated in terms of Ω in Hornung's (1972) previous conclusion. Note, however, that the three pairs of cases used by Hornung (1972) to test the effectiveness of Ω as a correlating parameter are all very high enthalpy flows (u_∞=6.56 and 8.2 km/s), so that they do not bring out the influence ρ_e / ρ_{sh} or the sideways shifts of the curves with changing h_0. At Ω=1, the first case with specific reservoir enthalpy, 9.9 MJ/kg in Fig. 5.4, will already be close to equilibrium. However, for the fourth case with specific reservoir enthalpy, 38.2 MJ/kg in Fig. 5.4, the effect of nonequilibrium chemistry might be most marked at Ω=1. The flow patterns of the two cases are not expected to be similar, even with the same Ω.

5.3.2 Generalized Reaction Rate Parameter $\tilde{\Omega}$

To generalize the idea of a correlation between the dimensionless stand-off distance and dimensionless reaction rate parameter for more complex gases than nitrogen, in which many species are formed by many different reactions, a new dimensionless reaction rate parameter $\tilde{\Omega}$ will be defined. As was pointed out in section (5.2.2), $K\Omega$ is a more appropriate reaction rate parameter than Ω. By combining K in Eq. (5.28) and Ω in Eq. (5.29), a new generalized reaction rate parameter is then defined as

$$\tilde{\Omega} = K\Omega = -\left(\frac{\displaystyle\sum_{i=2}^{n} h_{c_i} \frac{dc_i}{dt}}{\frac{1}{2}\rho h_\rho [1 - \frac{u^2}{a_f^2}]} \right)_{sh} \left(\frac{a}{u_\infty} \right)$$

$$= \left(\frac{\displaystyle\sum_{i=2}^{n} h_{c_i} \frac{dc_i}{dt}}{\frac{1}{2}\left(\frac{\rho_\infty}{\rho}\right)^2 u_\infty^2 \left[1 + \frac{Mc_p}{R}\left(\frac{\rho}{\rho_\infty} - 2\right) \right]} \right)_{sh} \left(\frac{a}{u_\infty} \right) , \tag{5.52}$$

where h_{c_i} can be obtained using Eq. (5.19). Note that the dissociation rate of species i has been weighted with h_{c_i}, which is the energy needed to form species i equivalently, and $\tilde{\Omega}$ has incorporated the effect of the freestream velocity (or the dimensionless freestream kinetic energy μ). Since the ρ_{sh}/ρ_∞ term in the square bracket in the denominator is dominant compared to the other two terms, $\tilde{\Omega}$ can be approximated as

$$\tilde{\Omega} \sim \frac{\rho_{sh} \left(\displaystyle\sum_{i=2}^{n} h_{c_i} \frac{dc_i}{dt} \right)_{sh}}{\rho_\infty u_\infty^3 / 2a} \tag{5.53}$$

$$= \frac{\text{Energy absorption rate by chemical reactions just after the normal shock}}{\text{Input rate of free stream kinetic energy}} .$$

The physical meaning of $\tilde{\Omega}$ is then recognized as the ratio of the energy absorption rate by chemical reactions just after the normal shock to the input rate of freestream kinetic energy.

Fig. 5.9 shows the analytic solution of nitrogen flows of four different freestream conditions as a plot of the dimensionless stand-off distance $\bar{\Delta}$ and the newly defined reaction

rate $\tilde{\Omega}$, using the IDG model. The freestream conditions are as for Fig. 5.4. As expected from Eq. (5.32), Eq. (5.35), and Eq. (5.36), the frozen-side solutions for different freestream conditons have collapsed onto a single curve and the equilibrium-side solutions will depart from the main nonequilibrium curve at different dividing points to approach their own equilibrium limits of $\bar{\Delta}$ asymptotically. The dividing point and the equilibrium limit of $\bar{\Delta}$ are determined by the ratio of the equilibrium density to the shock density, ρ_e/ρ_{sh}, and constant L only. As may be seen, $\tilde{\Omega}$ has resolved the dispersion nature embedded in the solutions obtained using Ω as the dependent variable (see Fig. 5.4).
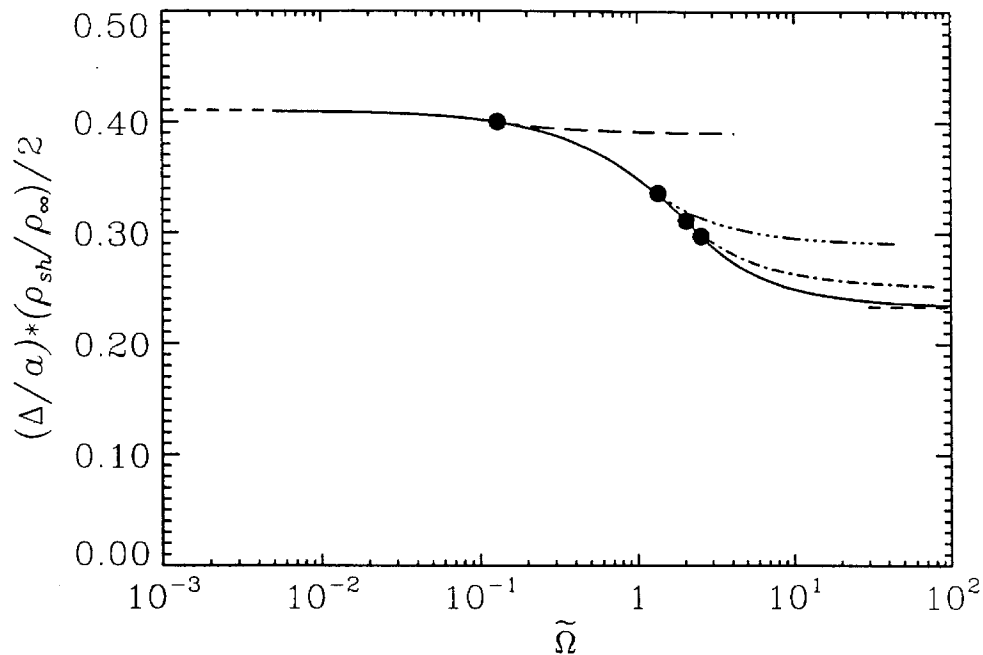
FIG. 5.9. Analytic solutions of stand-off distance variation with new reaction rate parameter. Freestream conditions as for Fig. 5.4. The filled circular symbols on the analytical curves are the points of dividing cases.

Similar solutions can be obtained for the nitrogen cases in Fig. 5.7 and Fig. 5.8. The solutions are shown in Fig. 5.10 and Fig. 5.11. The slight dispersion in Fig. 5.7 and Fig. 5.8 has disappeared. Also, the solutions of three different freestream conditions with the same h_0, in both Fig. 5.7 and Fig. 5.8, are almost identical. These analytic results for nitrogen clearly demonstrate that $\tilde{\Omega}$ is the reaction rate parameter that should be used.
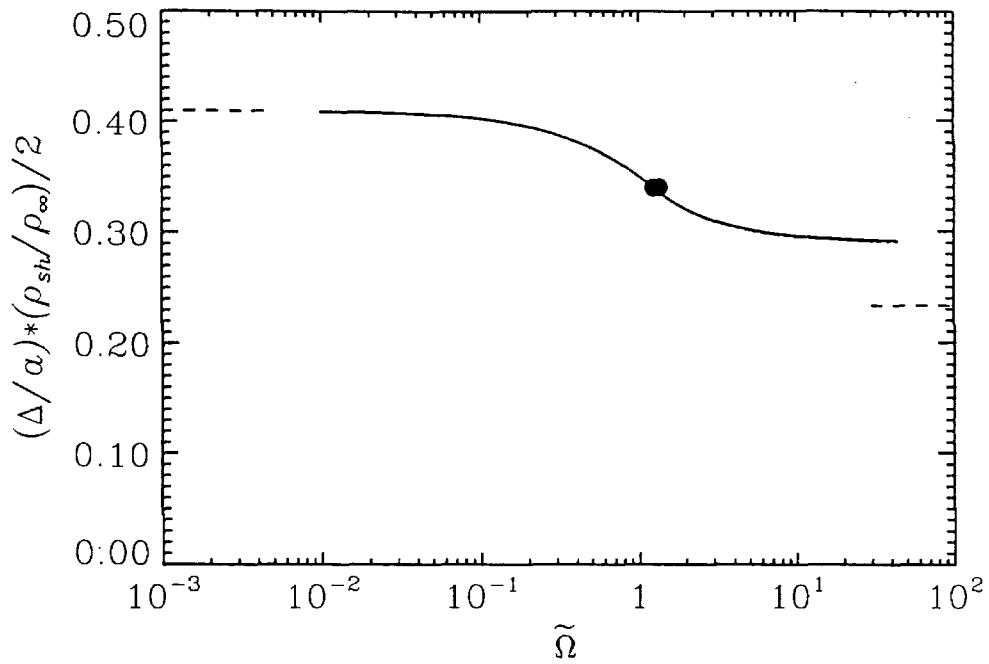
FIG. 5.10. Analytic solutions of stand-off distance variation with new reaction rate parameter. Freestream conditions as for Fig. 5.7. The filled circular symbols on the analytical curves are the points of dividing cases.
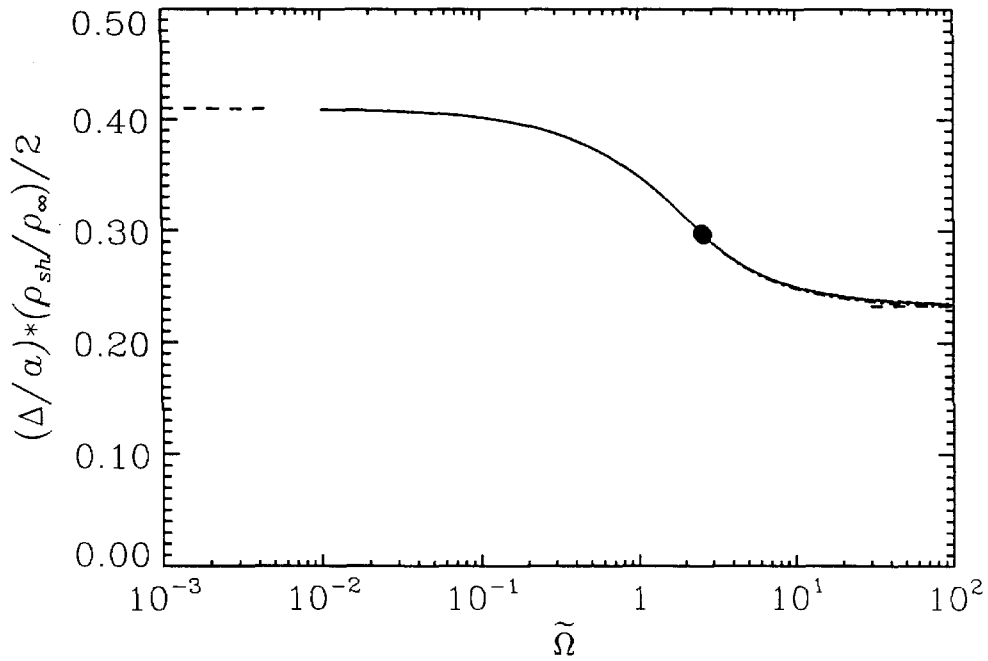
FIG. 5.11. Analytic solutions of stand-off distance variation with new reaction rate parameter. Freestream conditions as for Fig. 5.8. The filled circular symbols on the analytical curves are the points of dividing cases.

The compuational results of the dimensionless shock stand-off distance $\bar{\Delta}$ against $\tilde{\Omega}$ for nitrogen, air, and carbon dioxide are shown in Fig. 5.12, Fig. 5.13, and Fig. 5.14. The chemical reactions for nitrogen are as Eq. (3.20), and the freestream conditions used in calculation are as Table 5.2. For air and carbon dioxide, five primary chemical reactions between five species were used in the computation. The chemical reactions for air and carbon dioxide are as Eq. (3.21) and Eq. (3.22), respectively. The freestream conditions used in the numerical method are listed in Table 5.5. It may be seen that $\tilde{\Omega}$ correlates the stand-off density product $\bar{\Delta}$ quite well, and $\tilde{\Omega}$ has made the equilibrium tail emerge more evidently. Note that each type of symbol in Figs. (5.12) to (5.14) represents computational results of freestream conditions with the same specific total enthalpy h_0.
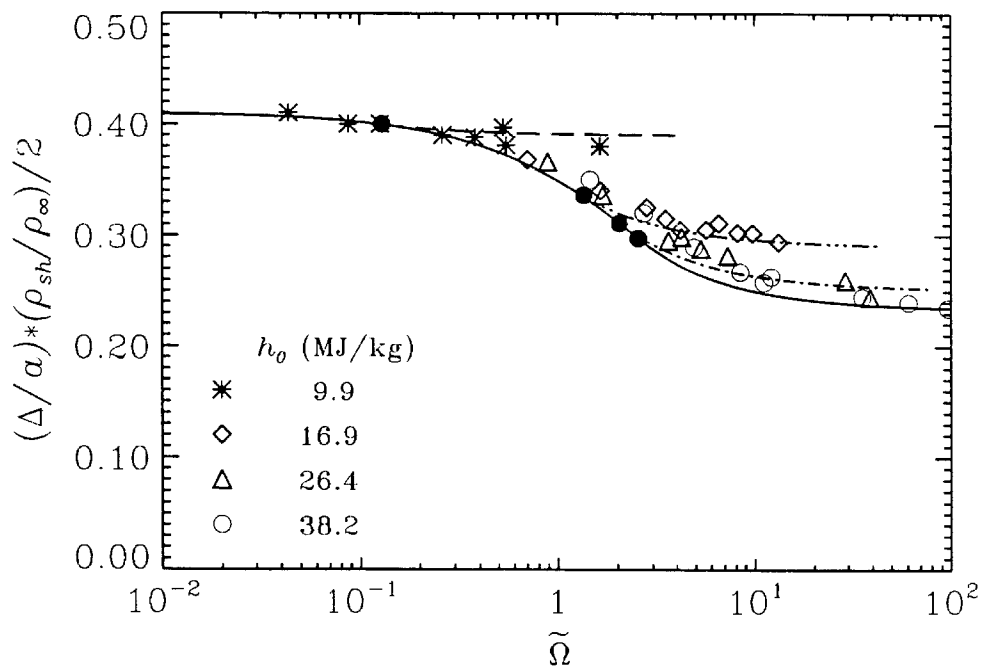
FIG. 5.12. Stand-off distance variation with the new reaction rate parameter for nitrogen. The symbols represent computational results using the freestream conditions listed in Table 5.2. The lines shown are for analytic solutions obtained using freestream conditions listed in Table 5.1
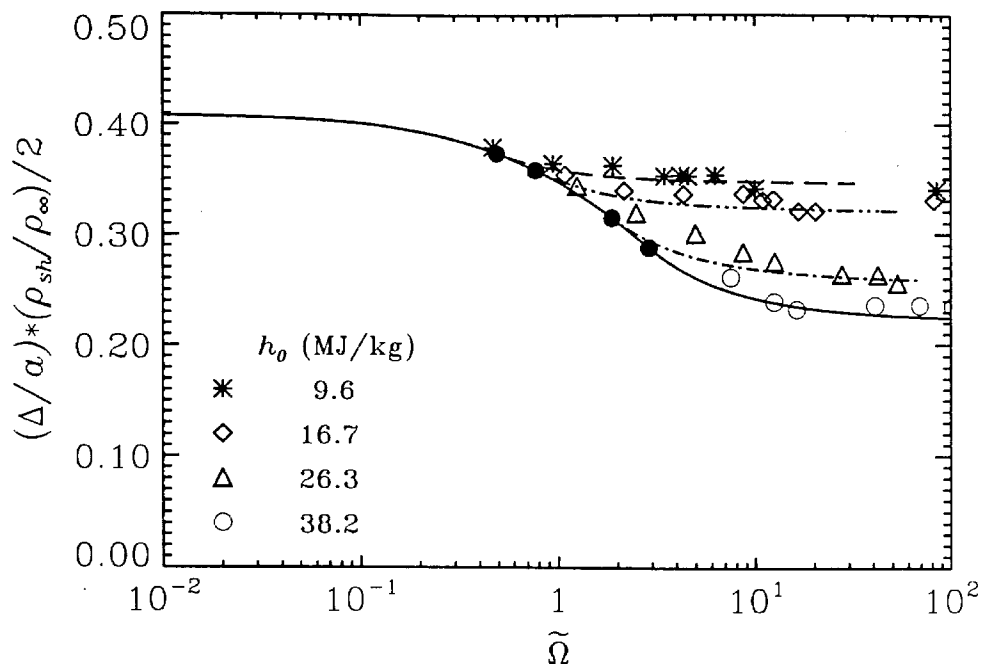
FIG. 5.13. Stand-off distance variation with the new reaction rate parameter for air. The symbols represent computational results using the freestream conditions listed in Table 5.5. The lines shown are for analytic solutions obtained using freestream conditions listed in Table 5.6
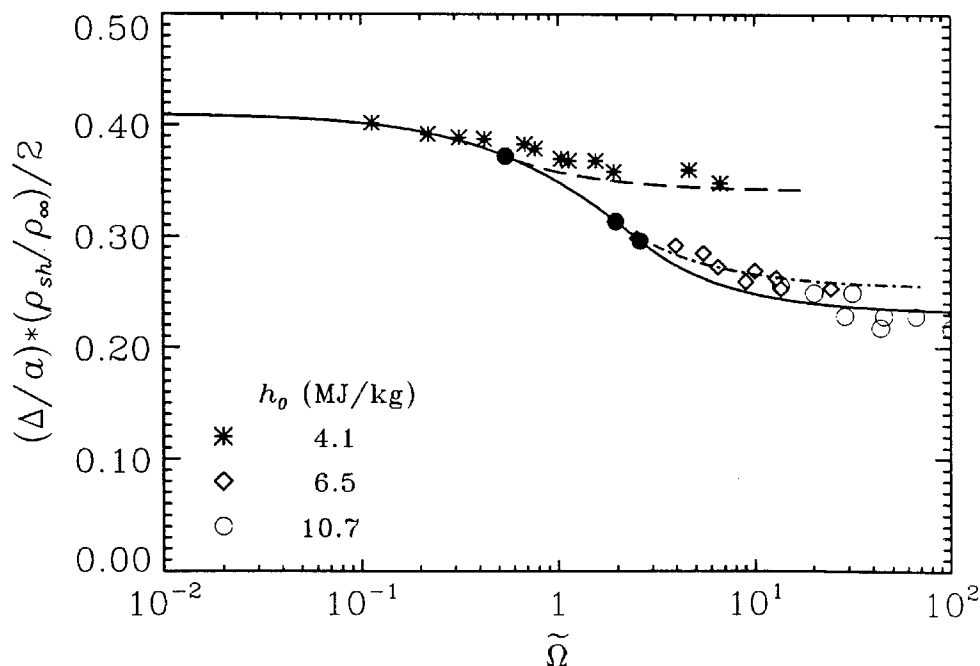
FIG. 5.14. Stand-off distance variation with the new reaction rate parameter for carbon dioxide. The symbols represent computational results using the freestream conditions listed in Table 5.5. The lines shown are for analytic solutions obtained using freestream conditions listed in Table 5.7

parameter	u_∞(km/s)	T_∞(K)	ρ_∞(kg/m^3)	h_0(MJ/kg)	a(m)
air					
from	3.89	1350	0.00379	9.53	0.0254
to	7.08	5370	0.0778	38.3	0.0762
carbon dioxide					
from	2.45	1070	0.0451	4.11	0.0254
to	3.49	2280	0.202	10.76	0.0762

Table 5.5. Range of values of parameters covered in calculation by Candler's method for air and carbon dioxide.

Also shown in Figs. (5.12) to (5.14) are the analytic solutions of different freestream conditions. For air and carbon dioxide, the freestream conditions used in obtaining the analytic solutions are listed in Table 5.6 and Table 5.7. For nitrogen, the values are as Fig. 5.9. Again, Eq. (5.32), Eq. (5.35), Eq. (5.36), and Eq. (5.37) are used to obtain the analytic solutions. One interesting feature that should be pointed out is that the frozen-side solutions are all the same for nitrogen, air, and carbon dioxide, provided the same value of L is used. The values of dividing points and equilibrium limits of $\bar{\Delta}$ for air and carbon dioxide are determined from the values of ρ_e/ρ_{sh} obtained using equilibrium normal-shock solutions. As may be seen, the computational correlation is in good agreement with the analytic solutions for all the test gases. The feature that the solution moves from the frozen limit to the equilibrium limit of $\bar{\Delta}$, as $\tilde{\Omega}$ increases, is clearly demonstrated for each test gas.

Line type	u_∞ km/s	T_∞ K	ρ_∞ kg/m³	h_0 MJ/kg	$c_{N_2,\infty}$	$c_{O_2,\infty}$	$c_{NO,\infty}$	$c_{N,\infty}$	$c_{O,\infty}$
Long dashed	3.9	1410	0.078	9.60	0.723	0.190	0.065	2.6×10^{-9}	8.2×10^{-3}
dash-dot-dot	5.0	2490	0.048	16.7	0.731	0.133	0.0504	6.2×10^{-6}	0.072
dash-dot	6.1	3660	0.033	26.3	0.74	0.022	0.0306	6.7×10^{-4}	0.194
solid	7.1	5270	0.024	38.3	0.68	2.3×10^{-4}	0.0072	0.081	0.230

Table 5.6. Freestream conditions used to calculate the analytic solutions in Fig. 5.13 for air.

Line type	u_∞ km/s	T_∞ K	ρ_∞ kg/m³	h_0 MJ/kg	$c_{CO_2,\infty}$	$c_{O_2,\infty}$	$c_{CO,\infty}$	$c_{C,\infty}$	$c_{O,\infty}$
Long dashed	2.5	1150	0.202	4.1	0.946	0.0196	0.0343	1.8×10^{-18}	1.1×10^{-11}
dash-dot	2.9	1770	0.213	6.5	0.866	0.0487	0.0854	7.7×10^{-15}	2.4×10^{-5}
solid	3.5	2280	0.102	10.8	0.593	0.141	0.259	2.1×10^{-13}	6.9×10^{-3}

Table 5.7. Freestream conditions used to calculate the analytic solutions in Fig. 5.14 for CO_2.

Figs. (5.15) to (5.17) show the comparsion of the normalized experimental data with analytic solutions of three different freestream conditions for nitrogen, air, and carbon dioxide. Each type of symbol in the figures represents experimental results of runs with the specific total enthalpy h_0 within a small range. Each analytic solution is obtained using the freestream conditons of one of the shots in that range of h_0. The shot numbers for the analytic solutions in Figs. (5.15) to (5.17) are shown in Table 5.8, and detailed freestream conditons for each shot are listed in Appendix A. The experimental data agree reasonably well with the analytic solutions for all the test gases. In the range of the present experiments, the flows tested are close to equilibrium, especially for the cases of nitrogen and air.

Line type	N_2 Shot No.	Air Shot No.	CO_2 Shot No.
Long dashed	198	201	523
dash-dot	181	481	203
solid	182	470	524

Table 5.8. Run numbers chosen to calculate the analytic solutions in Figs. 5.12 to 5.14.
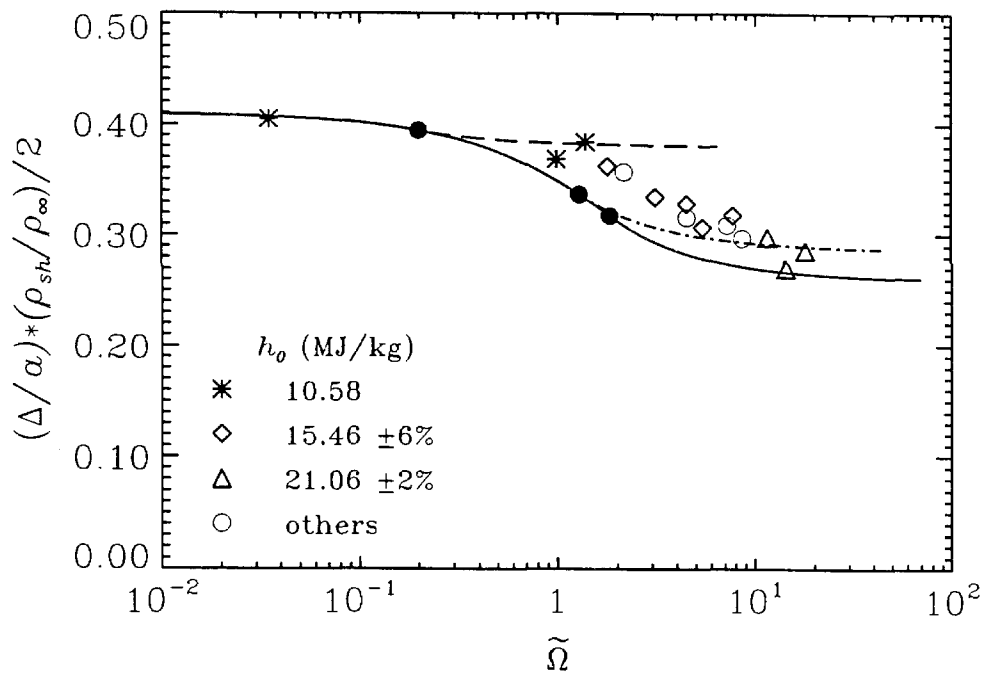
FIG. 5.15. Comparsion of normalized experimental stand-off distance and analytical solutions for N_2. The lines shown are for analytic solutions obtained using the freestream conditions in Table 5.8
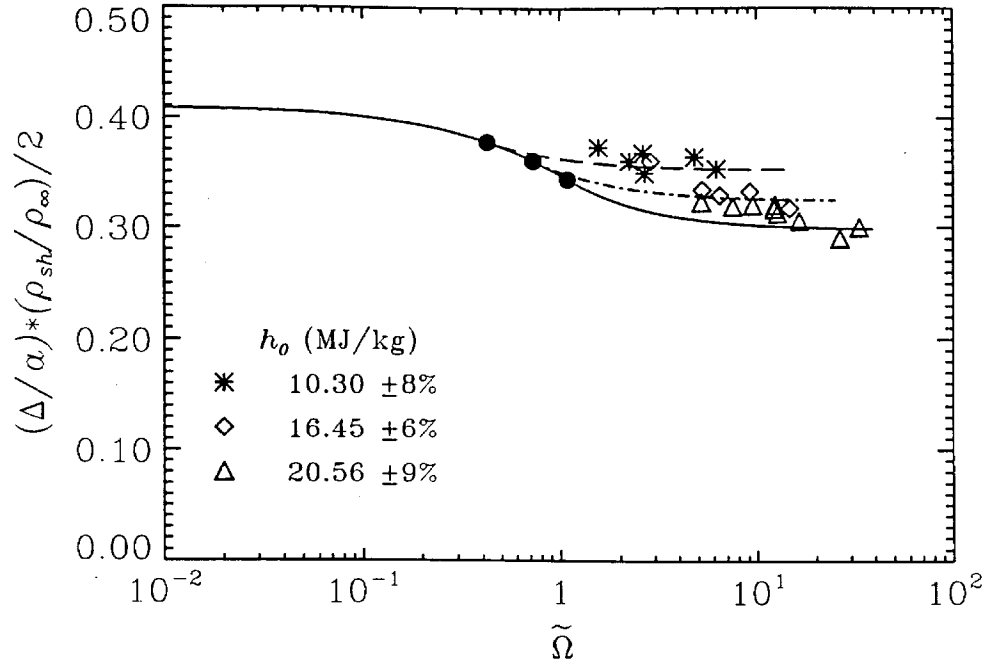
FIG. 5.16. Comparsion of normalized experimental stand-off distance and analytical solutions for air. The lines shown are for analytic solutions obtained using the freestream conditions in Table 5.8
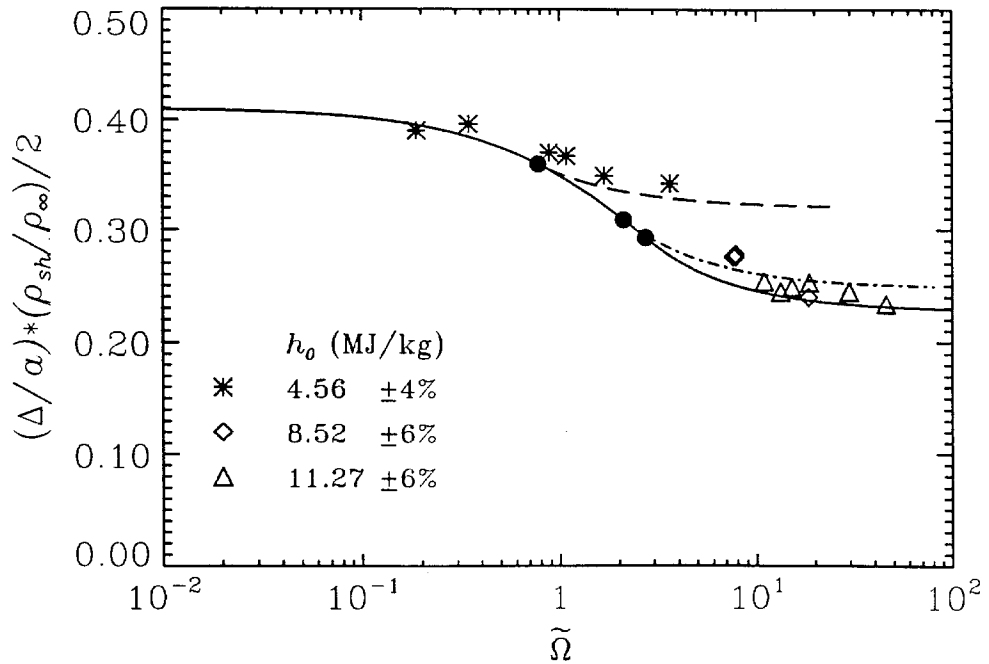
FIG. 5.17. Comparsion of normalized experimental stand-off distance and analytical solutions for CO_2. The lines shown are for analytic solutions obtained using the freestream conditions in Table 5.8

5.4 Chapter Summary

An analytic attempt to understand the physics of the correlation between the dimension-less stand-off distance and the dimensionless reaction rate parameter Ω previously observed by Hornung (1972) for nitrogen has been presented in this chapter. The results of the theoretical derivation agree well with the numerical computations. The analytic solutions show that the correlation of numerical results of nitrogen between the dimensionless stand-off distance and the reaction rate parameter Ω is a collection of nonequilibrium regions for different freestream conditions. As has been observed before, the frozen limit of the dimensionless stand-off distance is fixed for a constant freestream Mach number. When the freestream kinetic energy is large enough to dissociate the gas, the reaction rate parameter Ω can be varied at given freestream conditions by adjusting the radius of the model. Different equilibrium limits are expected for flows with different freestream enthalpies. These limits will be clearly observed when the radius of a sphere is sufficiently large, for example, in the full-scale real flight situation. For nitrogen flows with the same freestream velocity, temperature, and dissociation fraction, the reaction rate parameter Ω represents the binary scaling parameter $\rho_\infty a$. The physics of the correlation can be understood as the binary scaling. The analysis indicates that a more appropriate correlation parameter would be the product of Ω with a freestream parameter K which is essentially inversely proportional to the total enthalpy.

The nonequilibrium dissociating flow of a complex gas, like air or carbon dioxide, over a sphere can be approximately correlated in terms of a new reaction rate parameter, $\tilde{\Omega}$, which incorporates the factor K, based on the analytic solutions. The correlation applies to the stand-off distance and represents the main nonequilibrium region of different freestream enthalpies. Numerical results also show that this parameter correlates the stand-off density product more satisfactorily than Ω for all the test gases studied.

The experimental results illustrated clearly that nonequilibrium reacting flows of nitrogen, air, and carbon dioxide can be obtained in the free-piston shock tunnel. The results agree well with the numerical computations and theoretical predictions. With the current

running conditions in T5, the results indicate that the flows are close to equilibrium, especially for cases of nitrogen and air.

CHAPTER 6

Nonequilibrium Recombination after a Curved Shock Wave

In this chapter, two-dimensional flow will be considered instead of axisymmetric flow. This choice makes the analysis somewhat simpler without losing the physical features to be discussed. The following work extends the prior analysis of Hornung (1976) for nonequilibrium dissociation after a curved two-dimensional shock wave in a hypervelocity dissociating flow of an inviscid Lighthill-Freeman ideal dissociating gas (IDG) to nonequilibrium recombination. Analytic solutions are obtained with the effective shock values derived by Hornung (1976) and the assumption that the flow is "quasi-frozen" after a thin dissociating layer near the shock. The solution gives the expression of dissociation fraction as a function of temperature on a streamline. The solution then provides a rule of thumb to check the validity of binary scaling for the experimental conditions and a tool to determine the limiting streamline which delineates the validity zone of binary scaling. The effects upon the nonequilibrium chemical reaction of the large difference in freestream temperature between free-piston shock tunnels and equivalent flight conditions are discussed. Numerical examples are presented and the results are compared with solutions obtained with two-dimensional Euler equations using Candler's code.

6.1 Nonequilibrium Dissociation after a Curved Shock Wave

Hornung (1976) performed an approximate analysis of the nonequilibrium IDG flow behind a curved two-dimensional shock wave, under the assumption that the flow is far from equilibrium and that the backward (recombination) reaction of Eq. (3.20) can be neglected in comparison with the forward (dissociation) reaction. He concluded that the flow could be conveniently divided into a thin layer of intense dissociation near the shock followed by

a large region of chemically frozen flow. The method of matched asymptotic expansions was used, with the product of shock curvature and reaction length as the small parameter. The expressions for the frozen dissociation level and effective shock values of the frozen flow were given by Hornung's solutions as functions of freestream, gas and shock parameters. Hornung (1988) and Stalker (1989) have referred to this freezing of the dissociation reaction as "quenching". Macrossan (1990) has shown that the recombination reaction is not negligible at the higher values of the density in the test section of the free-piston shock tunnel, although further downstream, the flow is frozen again. The aim of the work described here is to relax Hornung's binary reaction assumption and to understand the mechanism which 'freezes' the recombination.

6.2 Theoretical Derivation

The work is concerned with inviscid, adiabatic, hypersonic flow of a diatomic gas after a curved shock wave under conditions where the freestream speed u_∞ is sufficiently high to dissociate the gas. An IDG is considered, for which the reaction rate is given by Freeman (1958) as Eq. (5.44). A further simplification of the rate equation is afforded by the fact that, for situations where dissociation is important in gases such as nitrogen or oxgen, T is much smaller than θ_d, so that the temperature dependence of the dissociation near the shock is very strongly dominated by the exponential function, and the factor $C\rho T^\eta(1 - \alpha)$ may be considered constant (Freeman, 1958). With the above approximations, the reaction-rate equation is written as

$$\frac{d\alpha}{dt} = \frac{u_\infty \kappa_0}{\epsilon} \left\{ \exp\left(\frac{-\theta_d}{T}\right) - \frac{\alpha^2}{1 - \alpha} \frac{\rho}{\rho_d} \right\} , \tag{6.1}$$

where ϵ is a small constant parameter ($\epsilon \simeq 10^{-5}$) and $1/\kappa_0$ is a typical length scale, e.g., the radius of curvature of the shock.

6.2.1 Equations of Motion on a Streamline
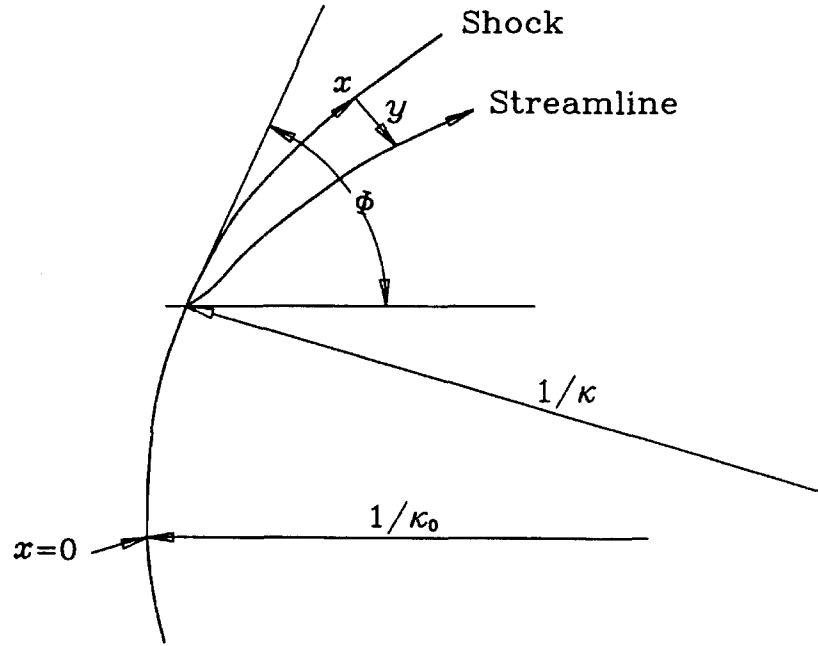
FIG. 6.1. Notation

To make the context clear, in this section, the equations of motion on a streamline derived by Hornung (1976) will be reiterated concisely. The coordinate system is illustrated in Fig. 6.1 , where x and y are coordinates parallel and perpendicular to a shock of curvature $\kappa(x)$, and $\phi(x)$ is the incident angle to the shock of the uniform freestream of velocity u_∞. κ is taken to be positive if the shock is convex towards the upstream direction. Let u and v be the components of velocity in x and y directions, respectively. The variables are nondimensionized according to

$$h^* = h/u_\infty{}^2 \ , \quad T^* = TR/M_{N_2}u_\infty{}^2 \ , \quad p^* = p/\rho_\infty u_\infty{}^2 \ ,$$

$$v^* = v/u_\infty \ , \quad u^* = u/u_\infty \ , \quad \rho^* = \rho/\rho_\infty \ , \tag{6.2}$$

$$x^* = x\,\kappa_0 \ , \quad y^* = y\,\kappa_0 \ , \quad \kappa^* = \kappa/\kappa_0 \ ,$$

where *s indicate dimensionless quantities.

An ideal dissociating gas is considered (see section (5.2.3)), for which the equations of state (Eq. (5.39) and Eq. (5.40)) and the reaction-rate equation (Eq. (6.1)) become

$$h^\star = \frac{4+\alpha}{1+\alpha}\frac{p^\star}{\rho^\star} + \alpha\theta_d^\star \quad, T^\star = \frac{p^\star}{\rho^\star(1+\alpha)} \quad.$$

$$\frac{d\alpha}{dt^\star} = \frac{1}{\epsilon}\left\{\exp\left(\frac{-\theta_d^\star}{T^\star}\right) - \frac{\alpha^2}{1-\alpha}\frac{\rho^\star}{\rho_d^\star}\right\} \quad.$$

(6.3)

$\theta_d^\star$ is the dimensionless dissociation energy per unit mass and is equal to $R\theta_d/M_{N_2}u_\infty^2$. $\theta_d^\star$ is $O(1)$ for situations where dissociation becomes important.

The conservation equations for momentum, energy, and mass are (see Hayes & Probstein 1966, p. 168)

$$u^\star u_{x^\star}^\star + (1 - \kappa^\star y^\star)v^\star u_{y^\star}^\star - \kappa^\star u^\star v^\star + p_{x^\star}^\star/\rho^\star = 0 \quad,$$

$$u^\star v_{x^\star}^\star + (1 - \kappa^\star y^\star)v^\star v_{y^\star}^\star + \kappa^\star u^{\star 2} + (1 - \kappa^\star y^\star)p_{y^\star}^\star/\rho^\star = 0 \quad,$$

$$h_{p^\star}^\star p_{y^\star}^\star + h_{\rho^\star}^\star \rho_{y^\star}^\star + h_\alpha^\star \alpha_{y^\star} + v^\star v_{y^\star}^\star + u^\star u_{y^\star}^\star = 0 \quad,$$

and

$$(\rho^\star u^\star)_{x^\star} - \kappa^\star \rho^\star v^\star + (1 - \kappa^\star y^\star)(\rho^\star v^\star)_{y^\star} = 0 \quad.$$

(6.4)

The subscripts denote partial differentiation.

The boundary conditions at the shock are (see Eq. (5.23))

$$p_{sh}^\star - p_\infty^\star = m^2(1 - \rho_{sh}^{\star -1}) \quad, \quad \alpha_{sh} = \alpha_\infty \quad, \quad v_{sh}^\star = m/\rho_{sh}^\star \quad,$$

$$h_{sh}^\star - h_\infty^\star = \frac{1}{2}m^2(1 - \rho_{sh}^{\star -2}) \quad, \quad u_{sh}^{\star 2} = 1 - m^2 \quad,$$

(6.5)

where $m = \sin\phi$ and the subscript sh denotes values just downstream of the shock. Boundary conditions are specified only on the shock because experience with inverse numerical techniques applied to blunt-body problems shows that, over a distance which is small compared with the radius of curvature of the shock, the shock boundary conditions are sufficient to specify the problem. By combining $x^\star$ and $y^\star$ derivatives (see Hornung 1976), the time derivatives of $p^\star$, $\rho^\star$, and $u^\star$ become

$$F^\star \frac{\mathrm{d}p^\star}{\mathrm{d}t^\star} = \rho^\star h_\alpha^\star \frac{\mathrm{d}\alpha}{\mathrm{d}t^\star} + \kappa^\star \frac{\rho^{\star2} h_{\rho^\star}^\star}{v^\star} G^\star ,$$

$$F^\star \frac{\mathrm{d}\rho^\star}{\mathrm{d}t^\star} = \frac{\rho^\star}{v^{\star2}} h_\alpha^\star \frac{\mathrm{d}\alpha}{\mathrm{d}t^\star} - \kappa^\star \frac{\rho^{\star2}}{v^\star}(h_{p^\star}^\star - \frac{1}{\rho^\star}) G^\star , \quad \text{and} \tag{6.6}$$

$$V^\star \frac{\mathrm{d}V^\star}{\mathrm{d}t^\star} = -\frac{1}{\rho^\star} \frac{\mathrm{d}p^\star}{\mathrm{d}t^\star} ,$$

where $V^\star = (u^{\star2} + v^{\star2})^{\frac{1}{2}}$ is the flow speed, $h^\star$ is considered as $h^\star(p^\star, \rho^\star, \alpha)$, and

$$F^\star = 1 - \rho^\star(\frac{h_{\rho^\star}^\star}{v^{\star2}} + h_{p^\star}^\star) ,$$

$$G^\star = \left\{ v^{\star2} + u^{\star2} + \frac{u^\star v_{x^\star}^\star}{\kappa^\star} - \frac{u^\star}{v^\star} \frac{1}{\rho^\star} \frac{p_{x^\star}^\star}{\kappa^\star} - v^\star \frac{u_{x^\star}^\star}{\kappa^\star} \right\} \Big/ (1 - \kappa^\star y^\star) . \tag{6.7}$$

6.2.2 The Differential Equation for $\alpha(T)$ along a Streamline

We now proceed as in Hornung (1976) but extend the analysis to include the recombination reaction rate. Differentiating $T^\star(p^\star, \rho^\star, \alpha)$ with respect to $t^\star$, substituting for the time derivatives of $p^\star$ and $\rho^\star$ from Eq. (6.6), and dividing by $\mathrm{d}\alpha/\mathrm{d}t^\star$ results in the following equations:

$$F^\star \frac{\mathrm{d}T^\star}{\mathrm{d}\alpha} = \left(\frac{T_{\rho^\star}^\star}{v^{\star2}} + T_{p^\star}^\star \right) \rho^\star h_\alpha^\star + F^\star T_\alpha^\star + \frac{\kappa^\star \rho^{\star2} G^\star}{v^\star} \left[T_{p^\star}^\star h_{\rho^\star}^\star - T_{\rho^\star}^\star (h_{p^\star}^\star - \frac{1}{\rho^\star}) \right] \frac{\mathrm{d}t^\star}{\mathrm{d}\alpha} . \tag{6.8}$$

The relevant derivatives of $T^\star$ and $h^\star$, and $\mathrm{d}\alpha/\mathrm{d}t^\star$ in Eq. (6.3) may now be substituted into Eq. (6.8), which becomes

$$\frac{\mathrm{d}T^\star}{\mathrm{d}\alpha} = -\frac{(1 - \rho^\star v^{\star2}/p^\star)\theta_d^\star + T^\star + \epsilon\kappa^\star v^\star G^\star e^{\theta_d^\star/T^\star}/(1 - A)}{(4 + \alpha)\left(1 - \frac{3}{4 + \alpha} \frac{\rho^\star v^{\star2}}{p^\star}\right)} , \tag{6.9}$$

where

$$A = \frac{\alpha^2}{1-\alpha}\frac{\rho^*}{\rho_d^*}e^{\theta_d^*/T^*} = B\,e^{\theta_d^*/T^*}\,,$$

and (6.10)

$$B = \frac{\alpha^2}{1-\alpha}\frac{\rho^*}{\rho_d^*}\,.$$

By estimating the order of magnitude of all the terms of Eq. (6.9), as in Hornung (1976), and retaining only the first-order terms, one gets

$$\frac{dT^*}{d\alpha} = -\frac{\theta_d^* - T^*\{(1+\alpha)\theta_d^*/m^2 - 1\} + b\epsilon(1+\alpha)T^*e^{\theta_d^*/T^*}/(1-A)}{(4+\alpha)\left\{1 - \frac{3(1+\alpha)}{4+\alpha}\frac{T^*}{m^2}\right\}}\,,$$ (6.11)

where

$$b = 3(1-m^2)\kappa^* m^{-1}\,.$$ (6.12)

To demonstrate all the features of the solution with less complexity and good accuracy, we neglect α in the two terms in curly brackets in Eq. (6.11), assuming α is negligible compared with 1 (see Hornung (1976)). Eq. (6.11) then becomes

$$\frac{d\alpha}{d\xi} = -\frac{(4+\alpha)(1-\lambda\xi)}{1 - \sigma\xi + \epsilon b\xi(1+\alpha)e^{1/\xi}/(1-A)}\,,$$ (6.13)

where $\xi = T^*/\theta_d^*$ and

$$\sigma = (\theta_d^* - m^2)/m^2\,,\quad \lambda = \frac{3}{4}\theta_d^*/m^2\,.$$ (6.14)

This model equation Eq. (6.13) differs from the one Hornung derived (1976) only in the factor A, which is the ratio of recombination rate to dissociation rate of an ideal dissociating gas. A is $o(1)$ right behind the shock, but may become important further downstream.

6.2.3 Solution for $\alpha(T)$ along a Streamline

Near the shock, where T^* or ξ is relatively large, the term in ϵ in Eq. (6.13) is small. As the temperature falls with proceeding dissociation, the ϵ term, which is due to the negative pressure gradient accompanying the curved shock, becomes important and finally dominates. The factor A will expedite the speed with which $d\alpha/d\xi$ approaches zero as the temperatures falls away from the shock. Three cases are then discussed.

Case 1: $A \ll 1$ for all ξ of interest.

Hornung's model equation is recovered from Eq. (6.13) and binary scaling is appropriate. All the solutions obtained by Hornung (1976) with the method of matched asymptotic expansions hold. The flow is then divided into a thin region of intense reaction close to the shock followed by a large region of chemically frozen flow. The thin reacting layer can then be considered to be part of the shock and effective shock conditions can be defined on each streamline by extrapolating the frozen-flow solution back to the shock . The frozen dissociation level and effective shock values of the frozen flow are given by Hornung as follows:

$$\alpha_{eff} = 4A_1\{1 - A_1^{-1} - \delta - \delta^2\log\delta - \delta^2[\frac{1}{6}\lambda - 1 + \log(4A_1 - 3)]\} + o(\delta^2), \quad (6.15)$$

$$\xi_{eff} = \delta\{1 + \delta\log\delta + \delta\log(4A_1 - 3)\} + o(\delta^2) , \quad (6.16)$$

$$p^*_{eff} = p^*_{sh} + (4A_1 - 3)\theta^*_d[B_1 - \delta] , \quad (6.17)$$

and

$$\rho^*_{eff} = p^*_{eff}/[\theta^*_d \xi_{eff}(1 + \alpha_{eff})] , \quad (6.18)$$

where subscripts eff and sh denote effective shock conditions and values just downstream of the shock as before,

$$A_1 = \{\exp(\lambda\sigma^{-1}\xi)(1 - \sigma\xi)^{-\sigma^{-1}(1-\lambda/\sigma)}\}_{sh} , \quad (6.19)$$

and

$$B_1 = \frac{\nu}{\sigma}\xi_{sh} - \frac{1 - \nu/\sigma}{\sigma}\log(1 - \sigma\xi_{sh}) . \quad (6.20)$$

δ and ν are defined by

$$\delta = 1/\log{(b\epsilon)^{-1}},$$ (6.21)

and

$$\nu = 3/(4A_1 - 3).$$ (6.22)

Case 2: $A = O(1)$ before $\epsilon b\xi(1 + \alpha)e^{1/\xi}$ becomes $O(1)$

The effective shock conditions were used to estimate the order of magnitude of A. From Eq. (6.10), $A = O(1)$ when $\xi_r = O(1/\log(B_r)^{-1})$, where

$$B_r = \frac{\alpha_{eff}^2}{1 - \alpha_{eff}} \frac{\rho_{eff}^\star}{\rho_d^\star},$$ (6.23)

and the subscript r denotes values at which recombination becomes important. In this case, recombination is always important and $\xi_r > \xi_{eff}$.

Case 3: $A = O(1)$ after $\epsilon b\xi(1 + \alpha)e^{1/\xi}$ becomes $O(1)$ $(\xi_r < \xi_{eff}$ or $\xi_r \simeq \xi_{eff})$

This case is the one of most interest. The flow will tend to reach and maintain the effective frozen dissociation level α_{eff} and further downstream, recombination will bring α_{eff} down again. One can simplify the model equation, Eq. (6.13), even further by observing that $A \gg 1$ and $\epsilon b\xi(1 + \alpha)/B \gg 1$ in the region further downstream of the dissociating layer. If we neglect the terms $\lambda\xi$ and $(1 - \sigma\xi)$, Eq. (6.13) becomes

$$\frac{d\alpha}{d\xi} = \frac{4 + \alpha}{\epsilon b\xi(1 + \alpha)/B}.$$ (6.24)

Notice that the sign of $d\alpha/d\xi$ has changed from negative ($\sim$ -4) near the shock (see Eq. (6.13)) to positive in Eq. (6.24). To solve Eq. (6.24) the assumption that the flow is "quasi-frozen" in the region downstream of the dissociating layer was made. The assumption was made based on observations from Macrossan's (1990) and Hornung *et al.* (1994) results that the dissociation fraction varied less than 20% from the maximum value in the free-piston shock tunnel conditions. The assumption gives

$$\rho \sim \rho_{eff}\,(\frac{\xi}{\xi_{eff}})^{\frac{1}{\gamma-1}} \;, \quad \text{and,} \quad \gamma = \frac{4+\alpha_{eff}}{3}\;, \tag{6.25}$$

where γ is the ratio of specific heats for the IDG (see Eq. 5.41)). Eq. (6.24) then becomes

$$\frac{d\alpha}{d\xi} = K_r\,\alpha^2\,\xi^{\frac{2-\gamma}{\gamma-1}} \;, \tag{6.26}$$

where

$$K_r = \frac{4\rho_{eff}^{\star}}{\epsilon b \rho_d^{\star}\,\xi_{eff}^{\frac{1}{\gamma-1}}} \;, \tag{6.27}$$

assuming that α is small compared to one. Eq. (6.26) may be integated to give the "quasi-frozen" flow solution

$$\alpha = \left[\frac{1}{\alpha_r} - K_r(\gamma-1)(\xi^{\frac{1}{\gamma-1}} - \xi_r^{\frac{1}{\gamma-1}})\right]^{-1} \;, \tag{6.28}$$

where $\xi_r = 1/log(B_r)^{-1}$ and α_r is taken to be α_{eff}. It is assumed that the initial condition is $\alpha = \alpha_{eff}$ at $\xi = \xi_r$ which is the premise of Case 3. The assumption that recombination becomes dominant at $\xi = \xi_r$ in Case 2 and Case 3 will be justified later with a numerical example.

6.3 Results and Discussion

One set of typical flow conditions in the shock tunnel T5 was chosen to illustrate the nature of the solutions obtained in section (6.2.3). A nitrogen flow over a circular cylinder of diameter D = 4 in. with freestream conditions u_∞ = 5.08 km/s, ρ_∞ = 0.04 kg/m³, h_0 = 16.0 MJ/kg, T_∞ = 2260 K and α_∞ = 0.029 was considered. The particle-tracking technique introduced in section (3.3) was used to obtain the values of the dissociation rate, recombination rate, and dissociation fraction along a streamline from the calculated flow field using Candler's inviscid method.

6.3.1 Comparsion of Analytic and Numerical Results

Fig. 6.2 shows the dissociation rate, recombination rate, and dissociation fraction along three streamlines in the example shock tunnel flow. Clearly, the recombination rate is not negligible compared to the dissociation rate, especially for the streamlines that cross the shock close to the axis. This feature essentially violates the binary scaling. It is interesting that, while the recombination rate becomes dominant in the downstream region, the flow seems to be frozen again because of the slow recombination rate.

In Table 6.1, the assumption that recombination becomes dominant at $\xi = \xi_r$ in Case 2 and 3 is justified. Close to the axis (ϕ = 89° and 82°), $\xi_{eff} < \xi_r$ and the solutions belong to Case 2. From streamline (a) (ϕ = 89°) in Fig. 6.2, it is clear that recombination becomes important immediately behind the shock. For the other streamlines in Table 1 where $\xi_{eff} > \xi_r$, the solutions are classified into Case 3. The good agreement between α_{eff} and $\alpha_{r,num}$ seems to support the assumption of the initial condition of Eq. (6.28). The dissociation fraction along streamlines (b) (ϕ = 72°) and (c) (ϕ = 67.5°) in Fig. 6.2 also suggests that the flow tends to reach and maintain Hornung's frozen dissociation level α_{eff} before recombination brings α_{eff} down again.
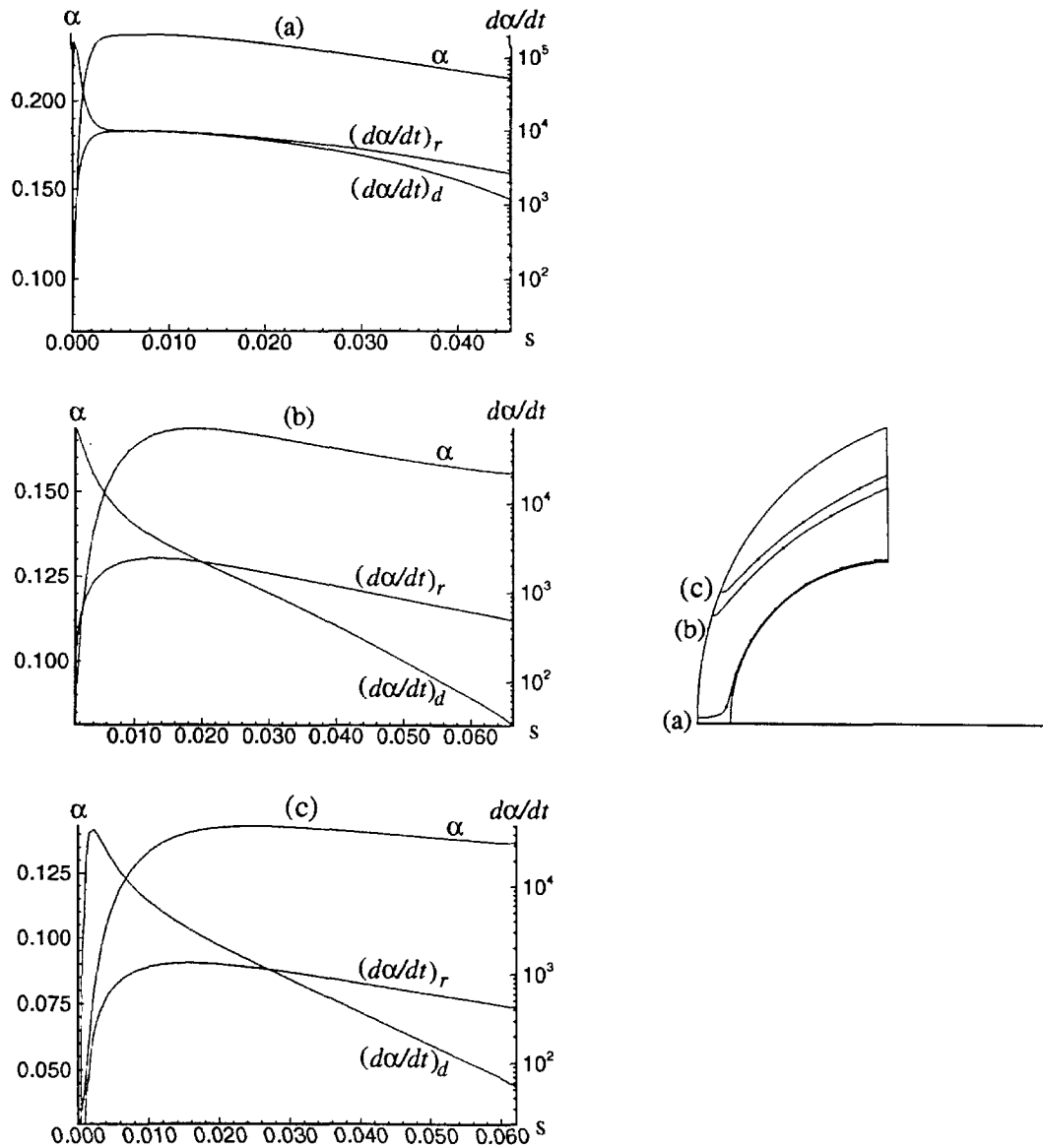
FIG. 6.2. Reaction rate and dissociation fraction variation along three selected streamlines in the example shock tunnel flow. The streamlines are labelled a, b, c in the diagram on the right. $(d\alpha/dt)_d$ and $(d\alpha/dt)_r$ are dissociation rate and recombination rate respectively. As may be seen, the recombination rate is not negligible for the inner streamlines.

ϕ	ξ_{eff}	α_{eff}	ξ_r	$\xi_{r,num}$	$\alpha_{r,num}$
89.0	0.0470	0.270	0.0669	0.0643	0.240
82.0	0.0589	0.217	0.0637	0.0634	0.222
76.0	0.0628	0.188	0.0621	0.0621	0.199
72.0	0.0644	0.169	0.0610	0.0600	0.168
67.5	0.0652	0.147	0.0597	0.0590	0.137
62.0	0.0662	0.116	0.0577	0.0573	0.110
56.5	0.0662	0.085	0.0553	0.0556	0.085

Table 6.1. The justification of the assumption that recombination becomes dominant at $\xi = \xi_r$ in Case 2 and 3. ϕ is the shock angle. ξ_{eff} and α_{eff} are Hornung's effective shock temperature and dissociation fraction. ξ_r is defined in section (6.2.3). $\alpha_{r,num}$ is the maximum value of the dissociation fraction extracted from the numerical calculation and $\xi_{r,num}$ is the corresponding temperature at $\alpha = \alpha_{r,num}$.

One can also transfer the coordinate system of Fig. 6.2 into (α, ξ) coordinate system. Fig. 6.3 shows the comparsion of the solution, Eq. (6.28), and the numerical results from Candler's code, where streamlines (a) and (b) correspond to the streamlines (b) and (c) in Fig. 6.2, respectively. It may be seen that the solutions starting at $\xi = \xi_r$ are in good agreement with numerical results.
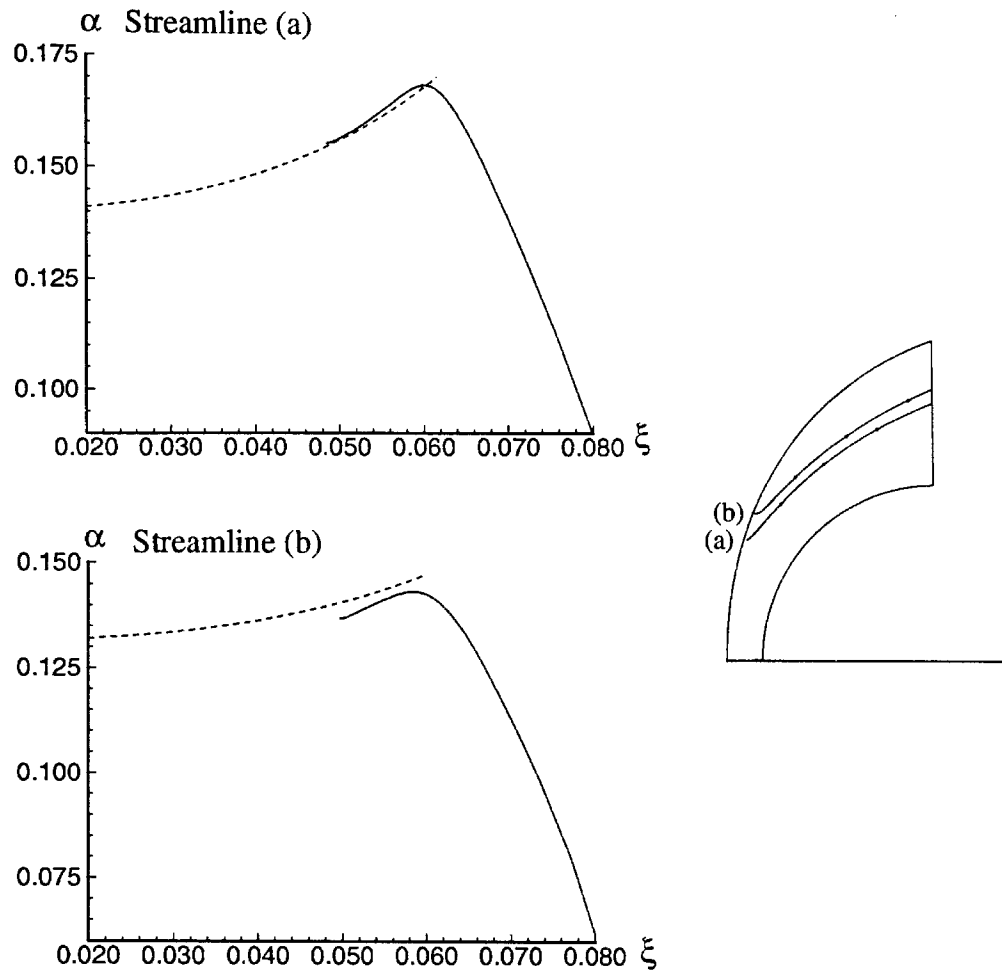
FIG. 6.3. Plots of dissociation fraction α versus dimensionless temperature ξ along two streamlines (a) and (b) over a circular cylinder (see inset on right). Freestream conditions: 5.08 km/s, nitrogen, 0.04 kg/m^3, 16.0 MJ/kg. Full line: numerical solution of Euler equations using Candler's code (α_∞ = 0.029). Dashed line: analytical solution of Eq. (6.28).

6.3.2 A Rule of Thumb for Binary Scaling

With the above results in mind, one is able to use Eq. (6.28) to derive a rule of thumb for validity of binary scaling. Eq. (6.28) can be rewritten in the form

$$\alpha = \alpha_{eff}\left[1 + \alpha_{eff}K_r(\gamma - 1)\xi_r^{\frac{1}{\gamma-1}}\left(1 - \left(\frac{\xi}{\xi_r}\right)^{\frac{1}{\gamma-1}}\right)\right]^{-1} . \qquad (6.29)$$

Binary scaling will work if

$$\alpha_{eff}K_r(\gamma - 1)\xi_r^{\frac{1}{\gamma-1}} \ll 1 . \qquad (6.30)$$

The flow will be "quenched" and $\alpha \rightarrow \alpha_{eff}$. The Case 3 degenerates into Case 1.

Substituting for K_r from Eq. (6.27), Eq. (6.30) becomes

$$\frac{\alpha_{eff}\rho_{eff}}{b\,\epsilon\,\rho_d^\star}\,\frac{4(1 + \alpha_{eff})}{3}\left(\frac{\xi_r}{\xi_{eff}}\right)^{\frac{3}{1+\alpha_{eff}}} \ll 1 . \qquad (6.31)$$

Note that

$$\frac{4(1 + \alpha_{eff})}{3}\left(\frac{\xi_r}{\xi_{eff}}\right)^{\frac{3}{1+\alpha_{eff}}} \sim O(1) , \qquad (6.32)$$

$$\rho_{eff} \sim O(10) .$$

Eq. (6.31) may then be simplified into

$$S \equiv \frac{\alpha_{eff}}{b\,\epsilon\,\rho_d^\star} \ll 0.1 . \qquad (6.33)$$

Eq. (6.33) then presents a rule of thumb to check the validity of binary scaling. Note that $\rho_d^\star = \rho_d\,/\,\rho_\infty$. Again freestream density has to be low to use binary scaling.

Take streamline (a) in Fig. 6.3 as an example. The shock shape for a flow over a circular cylinder is well approximated by the catenary $\kappa^* = m^2$, so that $b = 3 (1 - m^2) m$. For streamline (a) $\phi = 72°$, $b = 0.272$, $\epsilon = 8.88 \times 10^{-6}$, and $\alpha_{eff} = 0.169$. Recall from section (5.2.3) that $\rho_d = 130 \times 10^3$ kg/m^3 for nitrogen. Therefore, $S = 0.021$, which is not much smaller than 0.1. In fact, it implies that as $\xi \rightarrow 0$, $\alpha \sim \alpha_{eff}/(1 + 10S) = 0.14$, which is consistent with the result of streamline (a) in Fig. 6.3. About 20 % of the atoms will recombine. If one sets the criterion that the mass fractions should agree to within 5 % on the $\phi = 72°$ streamline between the free flight conditions and the shock tunnel environment, the above test conditions with $\rho_\infty = 0.04$ kg/m^3 are certainly not appropriate to simulate the free flight conditions where density is much lower and the flow will freeze at α_{eff}.

The analytic Eq. (6.28) can also provide a tool to determine the limiting streamline which delineates the validity zone of binary scaling. If one sets the same 5 % discrepancy of the mass fractions as the criterion for the limiting streamline and "guesses" that $\xi \sim 0.05$ at the vertical mid-plane of the circular cylinder, Eq. (6.28) will provide $\alpha(\xi = 0.05) = 0.14$ for the streamline of $\phi = 67.5°$. Compared to $\alpha_{eff} = 0.147$, the discrepancy of the mass fraction is about 4.75 %. The numerical method (see streamline (b) in Fig. 6.3) gives us $\alpha_{num}(\xi = 0.05) = 0.132$ and $\alpha_{r,num} = 0.137$. The discrepancy of the mass fraction is about 3.65 %. The analytic solution (4.3.4) predicts the limiting streamline at $\phi = 67.5°$ which is very close to the numerical prediction. For streamlines outside the limiting streamline, binary scaling is valid. For those inside the limiting streamline, three body recombination can not be neglected.

6.3.3 The Effect of Large Temperature Difference

The final point to be addressed is the large Mach number difference between the free flight conditions and the shock tunnel flows, pointed out by Macrossan (1990). In order to achieve sufficiently high density in the shock tunnel flow for the simulation of dissociative real-gas effects, the nozzle is operated at an area ratio that is too small to achieve the high Mach number of flight. Apart from the partially dissociated freestream, the shock tunnel flow therefore differs from flight conditions also in having too high a freestream temperature. Typical flight freestream conditions with the same circular cylinder and freestream density (ρ_∞ = 0.04 kg/ m^3) as in the experiments were considered. This density corresponds to that in the Earth's atmosphere at an altitude of about 25 km. The freestream temperature was taken as 217 K, which is about the atmospheric temperature for that altitude, and the freestream velocity was chosen to give the same stagnation enthalpy (h_0 = 16.0 MJ/kg) as in the experiments. The corresponding velocity is 5.6 km/s. The freestream Mach number was then 18.6 as opposed to 5.5 in the experiments.

The effective dissociation fraction α_{eff} on streamlines that have crossed the shock at ϕ, for the shock tunnel and the equivalent flight conditions, as a function of ϕ, are compared in Fig. 6.4. The agreement is good for the streamlines with a large incident angle and gets worse as the curved shock gets weaker. The shock tunnel flow has a higher frozen dissociation fraction than the equivalent flight flow for streamlines that cross the shock away from the axis, because of the two different flow velocities which have been chosen. Although the stagnation enthalpy has been chosen to match the simulation parameter of the ratio of the dissociation energy and the energy of the flow, the binary scaling parameter $\rho_\infty a / u_\infty$ which is the ratio of the dissociation rate and the flow rate, will not be the same. The shock tunnel flow with the slower speed will have more "time" to dissociate than the equivalent flight flow does before the expansion causes the "quenching" of the flow. Note that only results with ϕ smaller than 80° were shown because the theory of effective shock values is not valid for ϕ larger than 80° where the recombination is important. Also shown in Fig. 6.4 is the other flow condition with u_∞ = 5.08 km/s, ρ_∞ = 0.04 kg/m^3, h_0 = 13.0 MJ/kg, and T_∞ = 217 K. As may be seen, the dissociation fraction of the flow is well below the other

two cases. In this case, the binary scaling parameter is the same as in the shock tunnel flow and the time scale is matched. However, the energy parameters are not the same. The stagnation enthalpy of the flow is too low to produce the same degree of dissociation of the shock tunnel flow. This suggests that, if one is interested in simulating the chemical nonequilibrium flow over a blunt body with the free-piston shock tunnel facility, it is desirable that the shock tunnel flow has the same stagnation enthalpy as the real flight conditions, although the freestream temperatures will not be the same. Matching the binary scaling ρa and h_0 is more suitable than matching ρa and u_∞.
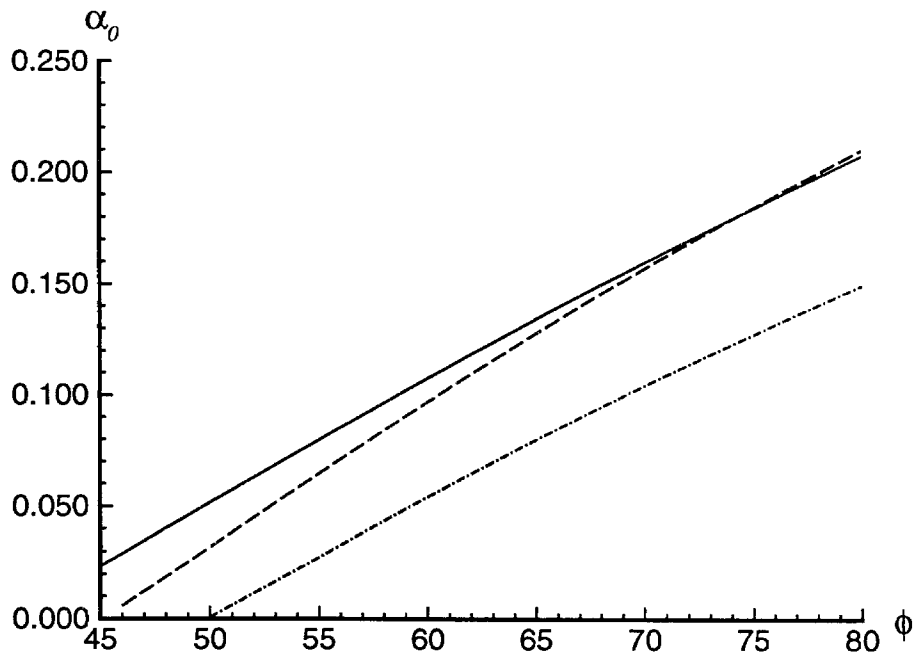
FIG. 6.4. Comparsion of effective frozen dissociation fraction α_0 for the free-piston shock tunnel and equivalent flight conditions. ϕ is the incident angle to the shock of the uniform freestream. Freestream conditions: N_2, α_∞ = 0.0, D=4 in. Full line: shock tunnel flow with conditions 16.0 MJ/kg, 5.08 km/s, 0.04 kg/m^3, 2260 K; Dashed line: equivalent flight flow with conditions 16.0 MJ/kg, 5.6 km/s, 0.04 kg/m^3, 217 K; Dash-dot line: 13.0 MJ/kg, 5.08 km/s, 0.04 kg/m^3, 217 K.

Fig. 6.5 (a) and Fig. 6.5 (b) show the comparsion of frozen dissociation fraction and the solution of Eq. (6.28) at ξ = 0.05 of the shock tunnel and equivalent flight conditions. The solution of Eq. (6.26) reaches a maximum at about ϕ = 75° for both flows and gradually merges into the frozen dissociation fractions. Compared to Table 6.1, one will easily realize that the solution of Eq. (6.28) is not appropriate for ϕ larger than 75°. The solution of Eq. (6.28) manifests itself as the dividing point between the Case 2 and Case 3. The limiting streamline can also be easily estimated from Fig. 6.5 (a) and Fig. 6.5 (b). From Fig. 6.5 (a) for the shock tunnel flow, one can see that the discrepancy of dissociation fractions will be smaller than 5 % for streamlines with the incident angle smaller than 67.5°, which has been mentioned above.

Fig. 6.6 shows a comparsion of the solutions of Eq. (6.28) at ξ = 0.05 of shock tunnel and equivalent flight conditions. The dissociation fraction of the equivalent flight condition is lower than that of the shock tunnel flow. Close to the plane of symmetry, the discrepancy is small and approximately constant. The solutions starting to diverge from each other away from the plane of symmetry. Compared to Fig. 6.4 and Fig. 6.5, it is clear that the difference between the two dissociation fractions at ξ = 0.05 is just the difference between the two effective frozen solutions in the weak portion of the curved shock wave. Near the stagnation streamline, although the effective frozen dissociation fractions are almost the same for the two flows (see Fig. 6.4), the solution of Eq. (6.28) at ξ = 0.05 of the equivalent flight conditions is lower than that of the shock tunnel flow, because the higher density behind the shock, corresponding to the higher Mach number for the equivalent flight conditions, enhances the recombination rate. Note that the recombination rate is proportional to the square of the density, while the dissociation rate is proportional only to the density. This difference in the dissociation fractions may result from the large difference in the Mach number. In the strong shock portion, the influence seems to be small. In the weak shock portion, it may become a problem.
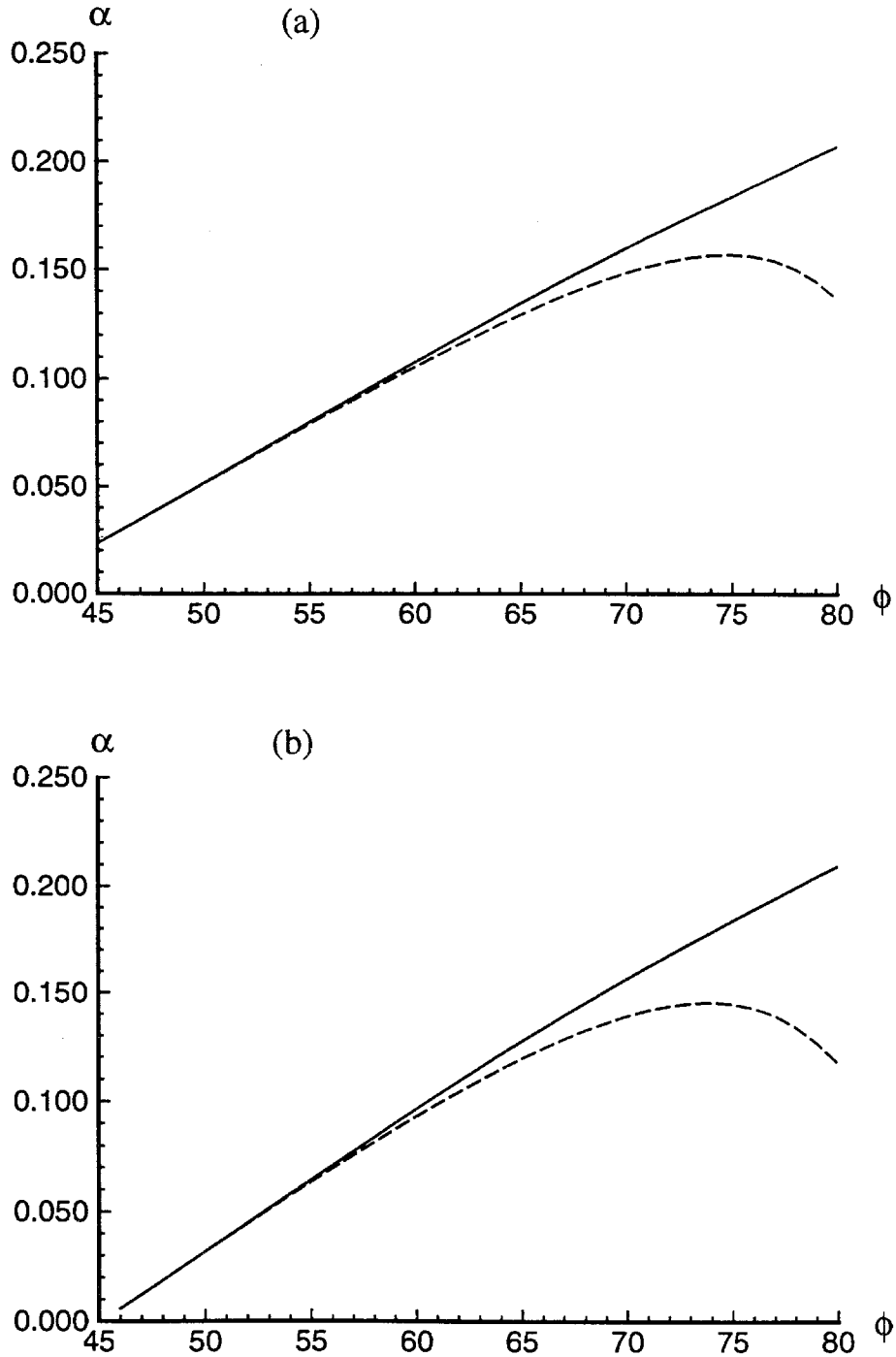
FIG. 6.5. Plots of effective frozen dissociation fraction α_{eff} and the solution of Eq. (6.28) at $\xi = 0.05$ versus incident angle ϕ for shock tunnel and equivalent flight conditions. Fig. 6.5 (a): shock tunnel flow; Fig. 6.5 (b): equivalent flight flow. Full line: effective frozen dissociation fraction α_{eff}. Dashed line: analytic solution of Eq. (6.28) at $\xi = 0.05$.
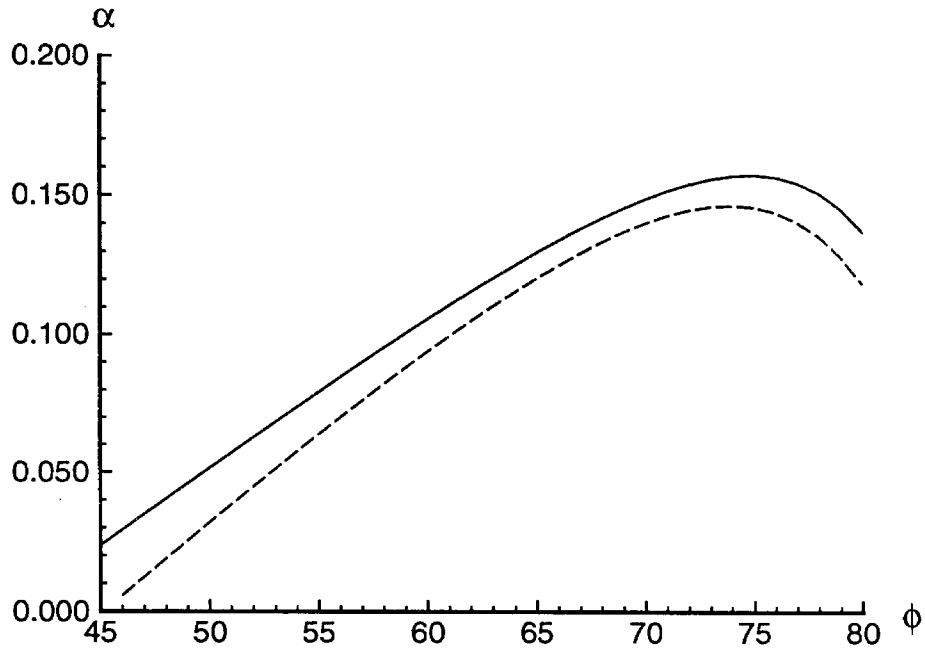
Fig. 6.6. Plot of solutions of Eq. (6.28) at ξ = 0.05 versus incident angle ϕ for shock tunnel and equivalent flight conditions. Full line: shock tunnel flow. Dashed line: equivalent flight flow.

6.4   Chapter Summary

The flows considered here were for the case of the hypersonic flow after a two-dimensional curved shock with Lighthill-Freeman ideal dissociating gas under circumstances that the recombination rate is not negligible.

Analytic solutions are obtained for a streamline with the assumptions that the flow is "quasi-frozen" in the region downstream of a thin dissociating layer near the shock. The theory gives an explicit expression for the dissociation fraction as a function of temperature. The analytic solutions are shown to agree quite well with the results obtained with

two-dimensional Euler equations using Candler's method. The dissociation fraction seems to be "frozen" again in the downstream region of the flow in the free-piston shock tunnel, although the recombination rate dominates the dissociation rate. The freezing of the flow occurs because of the strong exponential temperature dependence of the dissociation reaction rate and the effect of the negative pressure gradient associated with the shock curvature upon temperature and density for both dissociation and recombination reaction rates.

An important result is that the analytic solutions offer the engineer a simple expression as a rule of thumb to check the validity of binary scaling for the experimental conditions before doing any extensive and expensive numerical calculations and experiments. The analytic solutions can also be used to determine the limiting streamline which delineates the validity zone of binary scaling.

The effects upon the chemical nonequilibrium processes of the large difference in freestream temperature (or Mach number) between free-piston shock tunnels and equivalent flight conditions are discussed. The results indicate that, for the strong shock portion, it is not a serious issue, while away from the stagnation point, it may become important. The results support Macrossan's conclusion about the Mach number effect. In many cases, one can decouple this effect from the simulation of hypersonic chemical nonequilibrium flow. If one cannot remove the effect of large freestream temperature difference, the results suggest the stagnation enthalpy h_0 is a more important parameter to match than u_∞.

CHAPTER 7

Future Work

There are still many interesting features of hypervelocity dissociating flow over blunt bodies that need to be explored and the research is far from complete. Among them, three problems will be addressed in this chapter, namely, the vorticity concentration associated with the edge of the high-entropy layer generated in the nose region by the strongly curved shock, the evaluation of vibration-dissociation coupling models, and transition in the blunt body boundary layer and the effects of wall catalysis. Certain features of these three problems may have been observed during the course of the present experiments. These encourage further studies in the future.

7.1 Vorticity Interaction

It is known that there are strong entropy gradients generated in the nose region of a blunt body in hypervelocity flows. The high-entropy layer essentially wets the body as it flows downstream. For some distance downstream of the blunt nose, the thin boundary layer will grow inside this entropy layer, and then the boundary layer will eventually "swallow" the entropy layer far enough downstream. According to Crocco's theorem, the edge of the entropy layer is also a region of strong vorticity so that this interaction is sometimes called a "vorticity interaction".

Fig. 7.1 shows computational vorticity contours of a typical carbon dioxide run. Strong vorticity gradients are observed. Fig. 7.2 shows a resonantly-enhanced shadowgraph of the carbon dioxide flow with the same conditions as Fig. 7.1. (Resonantly-enhanced shadowgraphy has been described in section (2.5).) Streamlines are marked by the sodium seeding and are starting to roll up at the side of the sphere. Fig. 7.3 shows these vortical structures on

a larger scale. These vortical structures may be the by-product of the entropy layer. If they are, to our knowledge, this resonantly-enhanced shadowgraph is the first visualization of the vorticity interaction in hypervelocity blunt-body flows. Further experiments are needed before definite conclusions may be reached. Nevertheless, the resonantly-enhanced shadowgraphic technique may provide a promising tool for studying the vorticity-interaction problem in hypervelocity blunt-body flows.

Vorticity	
10	-60000
9	-70000
8	-80000
7	-90000
6	-100000
5	-110000
4	-120000
3	-130000
2	-140000
1	-150000
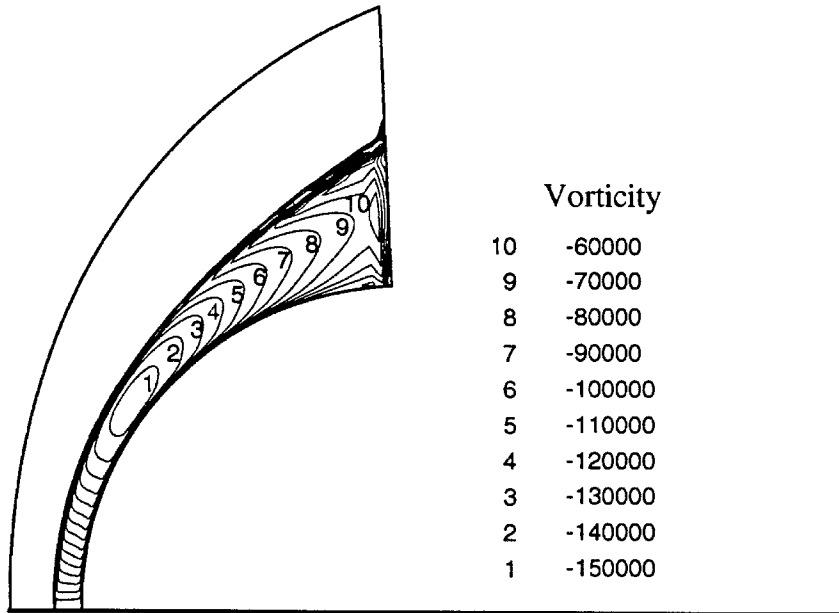
FIG. 7.1. Result of a computation of the vorticity field of over a sphere of 4 in diameter. Free stream conditions: CO_2, 3.55 km/s, 0.081 kg/m^3, 11.27 MJ/kg (shot 524).
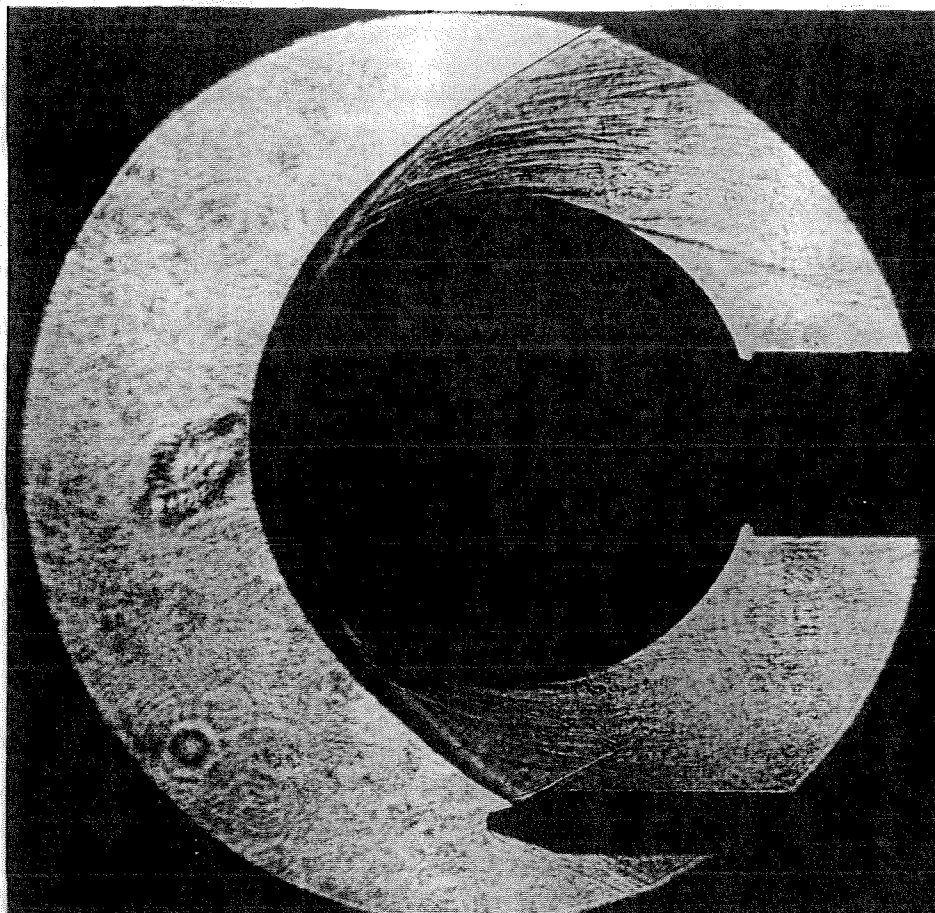
FIG. 7.2. Resonantly-enhanced shadowgraph of CO_2 flow over a sphere, at the same conditions as those of Fig. 7.1. The blemish ahead of the bow shock wave is due to a flaw in the optical window.
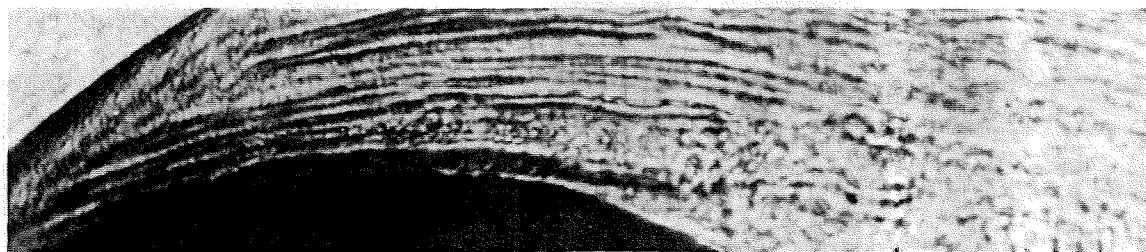
FIG. 7.3. Enlargement of the vortical structures in Fig. 7.2.

The interaction of the entropy layer and the boundary layer has been a challenging aerodynamic problem for years. The effect of the shock-generated free-stream vorticity on hypersonic boundary layer needs to be understood. Also, experimental and numerical investigations of the real-gas effects in this important feature, both with respect to the amount of vorticity produced by the bow shock, and with respect to the additional amount produced by dissociation downstream of the bow shock (see Eq. (5.7)) are essential to improve the understanding of the fundamental physics in nonequilibrium flow.

7.2 Evaluation of Vibration-Dissociation Coupling Models

Computational fluid dynamics has proved to be a useful method for studying hypervelocity dissociating flow over blunt bodies. To accurately predict these flow fields, the coupling between the dissociation process and the vibrational state of the gas must be correctly modeled.

Landau and Teller (1936) originally derived an expression for vibrational relaxation in gases considering only transitions between neighboring vibrational energy levels of a simple harmonic oscillator. By using expressions for vibrational relaxation times based on experimental data as given by Millikan and White (1963), it is possible to extend this expression to anharmonic oscillators. This model, however, fails to take into account the coupling between dissociation and the vibrational state of the gas. Namely, in regions where the vibrational temperature lags the translational temperature, molecules have less internal energy than if they were at thermal equilibrium, thus inhibiting the dissociation process.

In the present research, Park's (1988, 1989) semi-imperical two-temperature model is implemented in Candler's code to account for this coupling. This model uses the Landau-Teller expression for vibrational relaxation but also assumes that the dissociation rate is governed by the average temperature $T_{ave} = \sqrt{TT_v}$ instead of the translational temperature T. While this method can be extended to take into account that dissociating molecules have

higher than average vibrational energy, currently only the average vibrational energy is removed during dissociation.

Previously, the coupled-vibration-dissociation (CVD) model of Hammerling *et al.* (1959) and the coupled-vibration-dissociation-vibration (CVDV) model with preferential removal of Marrone and Treanor (1963) account for this effect. The CVDV model, under the assumption that the relaxation of vibrational energy occurs through a series of Boltzmann distributions, includes expressions in the vibrational relaxation equation that account for the higher than average energies of the dissociating molecules and the different energy at which new molecules are formed. The effect of vibration on dissociation is accounted for by a coupling factor which modifies the dissociation rate. Additionally, the fact that molecules in higher vibrational energy levels are more likely to dissociate is accounted for by a preferential removal parameter.

The research on the evaluation of these models is currently under way with the joint efforts of experimenters in T5 and the computation group at the University of Minnesota led by Professor Candler. The research was motivated by the comparsion of the experimental and computational interferograms shown in Fig. 4.38. Recall that the features of the experimental photograph are faithfully reproduced by the computation, except for a slight difference in the vicinity of the shock, where the vibrational and translational temperatures are not at thermal equilibrium and the correct modelling of the vibration-dissociation coupling is most needed.

It is hoped that the combination of experimental and numerical efforts will shed light on the mechanism of the vibration-dissociation coupling and make it possible to not only assess the validity of these models, but also to determine the actual amount of vibrational energy removal during dissociation.

7.3   Transition in the Blunt-Body Flow and Effects of Wall Catalysis

In chapter 4, the interesting phenomenon that occurred in the measured heat transfer distributions for carbon dioxide needs to be further studied. The effect of roughness on transition to turbulence in the nose region and the effect of nose bluntness on the transition on the after-body of a blunt cone are both interesting subjects.

For understanding the effects of the surface catalysis, the numerical code implemented with the boundary condition of wall catalysis will be a useful tool. The fabrication of a model with quantitatively measurable surface catalysis is also important. The diagnostic technique for the chemical species concentration is, of course, essential for this study.

CHAPTER 8

Conclusions

In the present research, three aspects of the fundamental physics of chemical nonequilibrium flow over spheres were investigated through theoretical derivations and a series of computations and experiments, using nitrogen, air, and carbon dioxide as test gases. The three aspects and the conclusions of each aspect are summarized as follows:

1. Aerodynamic Heating in Hypervelocity Flow

a. The free-piston shock tunnel T5 was used to gather new data on hypervelocity dissociating flow and has extended the range of heat transfer measurements to freestream Reynolds number one million and stagnation enthalpy 22 MJ/kg.

b. Good agreement was observed among the measured stagnation point heat transfer rates, numerical computation results, and Fay and Riddell's theoretical predictions for all the test gases. This agreement provides another calibration of T5.

c. The measured heat flux distributions were also in reasonably good agreement with numerical computation results and Lees' theory for nitrogen and air.

d. Surface roughness may have caused early transition from laminar flow to turbulence for some cases of carbon dioxide. A more carefully designed experiment was suggested to resolve this interesting phenomenon and to gain more knowledge about carbon dioxide dissociating flow.

2. Correlation between the Reaction Rate Parameter and the Stand-off Distance

a. An analytical solution is obtained for inviscid hypervelocity dissociating flow over spheres, using an approximate Kármán-Pohlhausen-type analysis.

b. The solution explains the correlation between the dimensionless stand-off distance and the dimensionless reaction rate parameter Ω previously observed by Hornung (1972) for nitrogen, and agrees well with the correlation of numerical results. The physics of the correlation is shown as the binary scaling.

c. The analysis indicates that a more appropriate correlation parameter is the product of Ω with a freestream parameter K which is essentially inversely proportional to the total enthalpy. This new dimensionless reaction rate parameter can be extended to more complex gases than nitrogen, in which many species are formed by many different reactions, and generalizes Hornung's correlation. Both experimental and numerical results confirm the new correlation.

d. The experimental results clearly illustrated the capability of producing nonequilibrium reacting flows of nitrogen, air, and carbon dioxide, in the free-piston shock tunnel. With the current running conditions in T5, the results indicate that the flows are close to equilibrium, especially for cases of nitrogen and air.

3. Effect of Nonequilibrium Recombination in Hypervelocity Dissociating Flow

a. An analytical solution is obtained for inviscid hypervelocity dissociating flow after a curved two-dimensional shock with Lighthill-Freeman ideal dissociating gas under circumstances in which the recombination rate is not negligible. The solution gives an explicit expression for the dissociation fraction as a function of temperature along a streamline and agrees well with the numerical computation result extracted using the particle-tracking technique.

b. The solution provides a rule of thumb to check the validity of binary scaling for the experimental conditions and can be used to determine the limiting streamline which delineates the validity zone of binary scaling.

c. The effects upon the chemical nonequilibrium processes of the large difference in freestream temperature (or Mach number) between free-piston shock tunnels and equivalent flight conditions are discussed. The results indicate that, for the strong shock portion, it is not a serious issue, while away from the stagnation point, it may become important. The results support Macrossan's conclusion about the Mach number effect. In many cases, one can decouple this effect from the simulation of hypersonic chemical nonequilibrium flow. If one can not remove the effect of large freestream temperature difference, the results suggest the stagnation enthalpy h_0 is a more important parameter to match than u_∞.

The difficulties associated with the experimental investigation of hypervelocity flow over spheres made the application of numerical simulation an important complement to the experimental effort. During the course of this research, the computational method has strongly enhanced the understanding provided by the experimental data and stimulated the theoretical derivations.

Optical differential interferometry proved to be very valuable in providing the evidence to validate the numerical code and the important information of the stand-off distance and shock shape. Computational interferometry also proved to be a useful tool to visualize the computational flow fields and to have a direct comparsion of the computational flow field with the experimental one.

References

Alpher, R. A. and White, D. R. (1959) "Optical refractivity of high-temperature gases. I. Effects resulting from dissociation of diatomic gases," *Physics of Fluids*, **2** (2) 153-161.

Ambrosio, A. and Wortman, A. (1962) "Stagnation point shock detachment distance for flow around spheres and cylinders," *ARS J.*, **32**, 281.

Anderson, J. D. (1989) *"Hypersonic and high temperature gas dynamics,"* McGraw-Hill, New York.

Avallone, Eugene A., and Theodore Bannierster III (1987) *"Standard Handbook for Mechanical Engineers,"* McGraw-Hill, Ninth Edition.

Blenstrup, G., Bershader, D. and Langhoff, P. (1979) "Recent results of resonan t refractivity studies for improved flow visualization," *Proceedings of the 12th International Symposium on shock tubes and waves, Jerusalem, Israel.*

Blottner, F. G., Johnson, M., and Ellis, M. (1971) "Chemically reacting viscous flow program for multi-component gas mixtures," Sandia Laboratories, Albuquerque, NM, Rept. SC-RR-70-754, Dec.

Candler, G. V. (1988) "The computation of weakly ionized hypersonic flows in thermo-chemical nonequilibrium," Ph.D. Thesis, Stanford University.

Candler, G. V. and MacCormack, R. W. (1988) "The computation of hypersonic ionized flows in chemical and thermal nonequilibrium," AIAA 87-1546.

Cumming, E. (1993) "Design and operation of the T5 diaphragm indenter system," GALCIT Report FM 93-3.

Fay, J. A. and Riddell, F. R. (1958) "Theory of stagnation point heat transfer in dissociated air," *J. Aero. Sci.*, **25** (2), 73-85.

Freeman, N. C. (1958) "Nonequilibrium flow of an ideal dissociating gas," *J. Fluid Mech.* **3**, 407-425.

Gai, S. L. and Joe, W. S. (1992) "Laminar heat transfer to blunt cones in high-enthalpy hypervelocity flows", *J. Thermophysics and Heat Transfer*, **6** (3), 433-438.

Germain, P., Cummings, E. and Hornung H. G. (1993) "Transition on a sharp cone at high enthalpy; new measurements in the shock tunnel T5 at GALCIT," AIAA 93-0343, Reno.

Germain, P. (1993) "The boundary layer on a sharp cone in high-enthalpy flow," Ph.D. Thesis, California Institute of Technology.

Gibson, W. E. and Marrone, P. V. (1964) "A similitude for nonequilibrium phenomena in hypersonic flight," *AGARDograph* **68**, 105-132.

Hall, J. G., Eschenroeder, A. A. and Marrone, P. V. (1962) "Blunt-nose inviscid airflows with coupled nonequilibrium processes," *J. Aero. Sci.*, **29** (9), 1038-1051.

Hammerling, P., Teare, J. D., and Kivel, B. (1959) "Theory of radiation from luminous shock waves in nitrogen," *Physics of Fluids*, **2** (4), 422-426.

Hayes, W. D. and Probstein, R. F. (1966) *"Hypersonic flow theory,"* Academic.

Hornung, H. G. (1972) "Nonequilibrium dissociating nitrogen flows over spheres and circular cylinders," *J. Fluid Mech.*, **53**, 149-176.

Hornung, H. G. (1976) "Nonequilibrium ideal-gas dissociation after a curved shock wave," *J. Fluid Mech.*, **74**, 143-159.

Hornung, H. G. (1988) "Experimental real-gas hypersonics," *Aero. J.*, **92**, 379.

Hornung, H. G. and Bélanger, J. (1990) "Role and techniques of ground testing for simulation of flows up to orbital speed," AIAA 90-1377, Seattle.

Hornung, H. G. (1992) "Performance data of the new free-piston shock tunnel at GALCIT," AIAA 92-3943, Nashville.

Hornung, H. G., Wen C. and Candler, G. V. (1994) "Hypervelocity flow over spheres," *Acta Mechanica* [Suppl], **4**, 163-170.

Kaye, G. W. C. and Laby, T. H. (1986) *"Tables of Physical and Chemical Constants and Some Mathematical Functions,"* Longman, New York.

Kemp, N. H., Rose, P. H. and Detra, R. W. (1959) "Laminar heat transfer around blunt bodies in dissociated air," *J. Aero. Sci.*, **26** (7), 421-430.

Koppenwallner, G. (1984) "Fundamental of hypersonics: Aerodynamics and heat transfer," *Hypersonic Aerothermodynamics*, Von Kármán Institute for Fluid Dynamics, Belgium, Feb.

Landau, L. and Teller, E. (1936) "Theory of sound dispersion," *Physikalische Zeitschrift der Sowjetunion*, **10**, 34-43.

Lee, J. H. (1985) "Basic governing equations for the flight regimes of aeroassisted orbital transfer vehicles," *Progress in Aeronautics and Astronautics: Thermal Design of Aeroassisted Orbital Transfer Vehicles*, **96**, 3-53, edited by H. F. Nelson.

Lees, L. (1956) "Laminar heat transfer over blunt bodies at hypersonic flight speeds," *Jet Propulsion*, **26** (4), 259-269.

Lighthill, M. J. (1957) "Dynamics of a dissociating gas, Part I Equilibrium flow," *J. Fluid Mech.*, **2**, 1-32.

Lordi, J. A., Mates, R. E. and Mosella, J. R. (1965) "Computer program for the numerical solution of nonequilibrium expansions of reacting gas mixtures," Contract No. NASr-109, Cornell Aeronautical Laboratory, Inc., Buffalo, N.Y.

Macrossan, M. N. (1990) "Hypervelocity flow of dissociating nitrogen downstream of a blunt nose," *J. Fluid Mech.*, **217**, 167-202.

Marrone, P. V. and Treanor, C. E. (1963) "Chemical relaxation with preferential dissociation from excited vibrational levels," *Physics of Fluids*, **6** (9), 1215-1221.

Maus, J. R., Griffith, B. J. and Szema, K. Y. (1984) "Hypersonic Mach number and real gas effects on space shuttle orbiter aerodynamics," *J. Spacecraft*, **21**, 136.

Matthews, R. K. (1993) "Boundary-layer transition," *Methodology of Hypersonic Testing*, Von Kármán Institute for Fluid Dynamics, Belgium, Feb., 16.1-16.9.

McIntosh, M. K. (1970) "A computer program for the numerical calculation of equilibrium and perfect gas conditions in shock tunnels," Australian Defence Scientific Service, Technical Note CPD 169, Salisbury, South Australia.

Merzkirch, W. (1987) *"Flow visualization,"* Academic Press Inc., New York.

Millikan, R. C. and White, D. R. (1963) "Systematics of vibrational relaxation," *J. Chemical Physics*, **39**, 3209-3213.

Omega Engineering, Inc. (1992) *"The temperature handbook,"* 28th edition, Stamford, Connecticut.

Park, C. (1985) "On convergence of computation of chemically reacting flows," AIAA 85-0247.

Park, C. (1988) "Assessment of a two-temperature kinetic model for dissociating and weakly ionizing nitrogen," *J. Thermophysics and Heat Transfer*, **2** (1), 8-16.

Park, C. (1989) "Assessment of a two-temperature kinetic model for ionizing air," *J. Thermophysics and Heat Transfer*, **3** (3), 233-244.

Park, C., Jaffe, J., Howe, J. and Candler, G. V. (1991) "Chemical kinetic problems of future NASA missions," AIAA 91-0464.

Rein, M. (1989) "SURF: A program for calculating inviscid supersonic reacting l ows in nozzles," GALCIT Report FM 89-1.

Rock, S. G., Candler, G. V. and Hornung, H. G. (1992) "Analysis of thermo-chemical nonequilibrium models for carbon dioxide flows," AIAA 92-2852.

Schultz, D. L. and Jones, T. V. (1973) "Heat transfer measurements in short duration facilities," AGARD Report 165.

Stalker, R. J. (1989) "Approximation for nonequilibrium hypervelocity aerodynamics," *AIAA J.* **27** (12), 1761-1769.

Sutton, K. and Graves, A. R. (1971) "A general stagnation-point convective-heating equation for arbitrary gas mixtures," NASA TR R-376, November.

Taylor, R. L., Camac, M., and Feinberg, R. M. (1967) "Measurements of vibration-vibration coupling in gas mixtures," *Proceedings of the Eleventh Symposium on Combustion*, The Combustion Institute, Pittsburgh, PA, 1967, 49-65.

Togami, K. (1993) "Hypervelocity dissociating flow over a spherically blunted cone," Aeronautical Engineer Thesis, California Institute of Technology.

Vincenti, W. G. and Kruger, C. H. (1965) *"Introduction to physical Gasdynamics,"* Wiley.

Wen, C. and Hornung, H. G. (1993) "Experiments on hypervelocity dissociating flow over spheres," *Proceedings of the 19th International Symposium on Shock Waves*, Marseille, France, to appear.

Wen, C. and Hornung H. G. (1993) "Nonequilibrium recombination after a curved shock wave," *Proceedings of 1st Pacific International Conference on Aerospace Science and Technology*, Tainan, Taiwan, **2**, 639-647.

Wilke, C. R. (1950) "A viscosity equation for gas mixtures," *J. Chem. Phys.*, **18** (4), 517.

Yee, L., Bailey, H. E. and Woodward H. T. (1961) "Ballistic range measurements of stagnation-point heat transfer in air and in carbon dioxide at velocities up to 18,000 feet per second," NASA TN D-777, March

Appendix A

Shot No.	h_0 MJ/kg	p_0 MPa	ρ_∞ g/m³	u_∞ km/s	T_∞ K	Ma_∞	Re_∞ $\times 10^{-5}$	$c_{s,\infty}$ kg/kg
198	10.58	60.0	56.1	4.23	1390	5.75	7.29	N 0.0034
199	10.58	60.0	56.1	4.23	1390	5.75	7.29	N 0.0034
200	21.06	60.0	33.9	5.55	2760	5.34	3.51	N 0.070
205	21.18	30.0	17.5	5.44	2420	5.51	2.02	N 0.103
206	12.83	30.0	24.6	4.54	1670	5.65	3.01	N 0.019

Table A.1 Reservoir and freestream conditions for experiments using test gas nitrogen and a sphere of 6 in. diameter.

Shot No.	h_0 MJ/kg	p_0 MPa	ρ_∞ g/m³	u_∞ km/s	T_∞ K	Ma_∞	Re_∞ $\times 10^{-5}$	$c_{s,\infty}$ kg/kg
180	10.58	60.0	56.1	4.23	1390	5.75	7.29	N 0.0034
181	16.46	60.0	40.2	5.07	2260	5.45	2.92	N 0.029
182	21.06	60.0	33.9	5.55	2760	5.34	2.34	N 0.070
187	10.58	60.0	56.1	4.23	1390	5.75	4.86	N 0.0034
494	20.15	30.0	18.1	5.35	2350	5.52	1.35	N 0.090
495	15.46	27.5	19.8	4.86	1950	5.59	1.55	N 0.041

Table A.2 Reservoir and freestream conditions for experiments using test gas nitrogen and a sphere of 4 in. diameter.

Shot No.	h_0 MJ/kg	p_0 MPa	ρ_∞ g/m³	u_∞ km/s	T_∞ K	Ma_∞	Re_∞ ×10⁻⁵	$c_{s,\infty}$ kg/kg
475	18.01	30.0	19.5	5.14	2200	5.53	1.10	N 0.064
478	18.01	30.0	19.5	5.14	2200	5.53	1.10	N 0.064
483	17.77	60.0	38.1	5.21	2420	5.41	2.05	N 0.039
484	20.68	56.0	32.2	4.99	2690	5.36	1.68	N 0.069

Table A.3 Reservoir and freestream conditions for experiments using test gas nitrogen and a sphere of 3 in. diameter.

Shot No.	h_0 MJ/kg	p_0 MPa	ρ_∞ g/m³	u_∞ km/s	T_∞ K	Ma_∞	Re_∞ ×10⁻⁵	$c_{s,\infty}$ kg/kg
507	15.70	75.0	51.6	5.00	2200	5.46	1.90	N 0.019
508	16.00	57.5	39.4	5.01	2190	5.47	1.46	N 0.026
514	15.46	27.5	19.8	4.86	1950	5.59	0.78	N 0.041

Table A.4 Reservoir and freestream conditions for experiments using test gas nitrogen and a sphere of 2 in. diameter.

Shot No.	h_0 MJ/kg	p_0 MPa	ρ_∞ g/m³	u_∞ km/s	T_∞ K	Ma_∞	Re_∞ ×10⁻⁵	$c_{s,\infty}$ kg/kg
518	17.23	57.5	37.4	5.15	2340	5.43	0.69	N 0.036

Table A.5 Reservoir and freestream conditions for experiments using test gas nitrogen and a sphere of 1 in. diameter.

Shot No.	h_0 MJ/kg	p_0 MPa	ρ_∞ g/m^3	u_∞ km/s	T_∞ K	Ma_∞	Re_∞ $\times 10^{-5}$	$c_{s,\infty}$ kg/kg		
201	10.30	60.0	62.7	4.05	1540	5.33	7.01	N$_2$	0.723	
								O$_2$	0.183	
								NO	0.064	
								N	1.27×10^{-8}	
								O	0.014	
202	20.87	60.0	34.2	5.51	2930	5.17	3.31	N$_2$	0.737	
								O$_2$	0.076	
								NO	0.038	
								N	4.75×10^{-5}	
								O	0.014	

Table A.6 Reservoir and freestream conditions for experiments using test gas air and a sphere of 6 in. diameter.

Shot No.	h_0 MJ/kg	p_0 MPa	ρ_∞ g/m³	u_∞ km/s	T_∞ K	Ma_∞	Re_∞ ×10⁻⁵	$c_{s,\infty}$ kg/kg	
183 197	10.30	60.0	62.7	4.05	1540	5.33	4.68	N_2 0.723 O_2 0.183 NO 0.0643 N 1.27×10^{-8} O 0.0140	
184	16.30	60.0	41.9	4.95	2390	5.20	2.81	N_2 0.731 O_2 0.131 NO 0.0508 N 4.81×10^{-6} O 0.0740	
185 186	20.87	60.0	34.2	5.51	2930	5.17	2.20	N_2 0.737 O_2 0.0763 NO 0.0382 N 4.75×10^{-5} O 0.0135	
195 196	21.54	60.0	49.4	5.61	3160	5.18	3.50	N_2 0.734 O_2 0.0858 NO 0.0436 N 7.05×10^{-5} O 0.123	
491	16.01	27.5	19.9	4.86	2070	5.33	1.45	N_2 0.733 O_2 0.0982 NO 0.0474 N 2.49×10^{-6} O 0.108	

Table A.7 Reservoir and freestream conditions for experiments using test gas air and a sphere of 4 in. diameter.

Shot No.	h_0 MJ/kg	p_0 MPa	ρ_∞ g/m³	u_∞ km/s	T_∞ K	Ma_∞	Re_∞ $\times 10^{-5}$	$c_{s,\infty}$ kg/kg
492	21.5	27.5	15.8	5.56	2620	5.25	1.12	N₂ 0.743 O₂ 0.0341 NO 0.0252 N 3.97×10^{-5} O 0.184
493	9.53	27.5	31.2	3.89	1340	5.43	2.45	N₂ 0.723 O₂ 0.176 NO 0.0654 N 3.58×10^{-9} O 0.0214
496	20.59	27.5	16.1	5.45	2620	5.20	1.15	N₂ 0.743 O₂ 0.0341 NO 0.0252 N 3.97×10^{-5} O 0.184
525	17.38	60.0	39.7	5.08	2530	5.19	2.63	N₂ 0.733 O₂ 0.118 NO 0.0478 N 9.04×10^{-6} O 0.0885
526	20.51	60.0	34.6	5.47	2870	5.20	2.25	N₂ 0.737 O₂ 0.0804 NO 0.0393 N 3.84×10^{-5} O 0.130

Table A.7(continued) Reservoir and freestream conditions for experiments using test gas air and a sphere of 4 in. diameter.

Shot No.	h_0 MJ/kg	p_0 MPa	ρ_∞ g/m³	u_∞ km/s	T_∞ K	Ma_∞	Re_∞ ×10⁻⁵	$c_{s,\infty}$ kg/kg
466	19.36	27.5	16.9	5.30	2360	5.34	0.92	N_2 0.739 O_2 0.0569 NO 0.0339 N 1.26×10^{-5} O 0.157
467	17.46	27.5	18.5	5.05	2200	5.33	1.01	N_2 0.736 O_2 0.0794 NO 0.0414 N 5.33×10^{-6} O 0.130
468	16.45	30.0	21.1	4.92	2140	5.31	1.14	N_2 0.733 O_2 0.0968 NO 0.0462 N 3.47×10^{-6} O 0.110
469	22.15	27.5	15.2	5.63	2710	5.21	0.79	N_2 0.744 O_2 0.0271 NO 0.0223 N 5.83×10^{-5} O 0.193

Table A.8 Reservoir and freestream conditions for experiments using test gas air and a sphere of 3 in. diameter.

Shot No.	h_0 MJ/kg	p_0 MPa	ρ_∞ g/m³	u_∞ km/s	T_∞ K	Ma_∞	Re_∞ $\times 10^{-5}$	$c_{s,\infty}$ kg/kg
470	20.59	27.5	16.1	5.45	2500	5.30	0.87	N_2 0.742 O_2 0.0428 NO 0.0287 N 2.38×10^{-5} O 0.174
471	10.98	27.5	27.6	4.13	1540	5.36	1.57	N_2 0.725 O_2 0.161 NO 0.0630 N 3.78×10^{-6} O 0.0370
472	9.99	27.5	30.0	3.96	1410	5.40	1.74	N_2 0.724 O_2 0.171 NO 0.0648 N 8.33×10^{-9} O 0.0259
473	16.01	27.5	19.9	4.86	2070	5.33	1.14	N_2 0.733 O_2 0.0982 NO 0.0474 N 2.49×10^{-6} O 0.108

Table A.8(continued) Reservoir and freestream conditions for experiments using test gas air and a sphere of 3 in. diameter.

Shot No.	h_0 MJ/kg	p_0 MPa	ρ_∞ g/m³	u_∞ km/s	T_∞ K	Ma_∞	Re_∞ ×10⁻⁵	$c_{s,\infty}$ kg/kg
474	18.97	27.5	17.2	5.25	2320	5.35	0.94	N_2 0.739 O_2 0.0615 NO 0.0355 N 1.04×10⁻⁵ O 0.151
479	11.09	60.0	58.8	4.18	1670	5.29	3.21	N_2 0.724 O_2 0.178 NO 0.0635 N 4.61×10⁻⁸ O 0.0195
481	16.45	60.0	41.6	4.97	2410	5.20	2.09	N_2 0.731 O_2 0.129 NO 0.0504 N 5.22×10⁻⁶ O 0.0759
482	19.73	60.0	35.8	5.37	2790	5.20	1.75	N_2 0.736 O_2 0.0897 NO 0.0414 N 2.75×10⁻⁵ O 0.120

Table A.8(continued) Reservoir and freestream conditions for experiments using test gas air and a sphere of 3 in. diameter.

Shot No.	h_0 MJ/kg	p_0 MPa	ρ_∞ g/m³	u_∞ km/s	T_∞ K	Ma_∞	Re_∞ ×10⁻⁵	$c_{s,\infty}$ kg/kg	
497	9.81	25.0	27.8	3.93	1370	5.42	1.08	N_2	0.724
								O_2	0.171
								NO	0.0650
								N	5.91×10^{-9}
								O	0.0262
498	16.01	27.5	19.9	4.86	2070	5.33	0.73	N_2	0.733
								O_2	0.0982
								NO	0.0474
								N	2.49×10^{-6}
								O	0.108
499	19.36	27.5	16.9	5.30	2360	5.34	0.61	N_2	0.739
								O_2	0.0569
								NO	0.0339
								N	1.26×10^{-5}
								O	0.157
504	10.39	75.0	77.5	4.08	1570	5.32	2.87	N_2	0.724
								O_2	0.186
								NO	0.0640
								N	1.30×10^{-8}
								O	0.0114

Table A.9 Reservoir and freestream conditions for experiments using test gas air and a sphere of 2 in. diameter.

Shot No.	h_0 MJ/kg	p_0 MPa	ρ_∞ g/m³	u_∞ km/s	T_∞ K	Ma_∞	Re_∞ ×10⁻⁵	$c_{s,\infty}$ kg/kg
505	14.98	75.0	56.0	4.78	2290	5.18	1.87	N_2 0.729 O_2 0.153 NO 0.0552 N 2.16×10^{-6} O 0.0495
506	21.30	75.0	41.8	5.57	3060	5.18	1.32	N_2 0.736 O_2 0.0809 NO 0.0408 N 6.17×10^{-5} O 0.129
511	10.85	57.5	57.5	4.14	1620	5.30	2.11	N_2 0.724 O_2 0.179 NO 0.0638 N 3.24×10^{-8} O 0.0185
512	17.07	55.0	37.0	5.04	2460	5.20	1.24	N_2 0.733 O_2 0.118 NO 0.0481 N 7.45×10^{-6} O 0.0886

Table A.9(continued) Reservoir and freestream conditions for experiments using test gas air and a sphere of 2 in. diameter.

Shot No.	h_0 MJ/kg	p_0 MPa	ρ_∞ g/m^3	u_∞ km/s	T_∞ K	Ma_∞	Re_∞ $\times 10^{-5}$	$c_{s,\infty}$ kg/kg
513	20.56	55.0	31.8	5.47	2840	5.20	1.04	N_2 0.738 O_2 0.0756 NO 0.0379 N 3.78×10^{-5} O 0.136

Table A.9(continued) Reservoir and freestream conditions for experiments using test gas air and a sphere of 2 in. diameter.

Shot No.	h_0 MJ/kg	p_0 MPa	ρ_∞ g/m^3	u_∞ km/s	T_∞ K	Ma_∞	Re_∞ $\times 10^{-5}$	$c_{s,\infty}$ kg/kg
519	10.66	57.5	58.4	4.11	1590	5.31	1.10	N_2 0.724 O_2 0.180 NO 0.0640 N 2.39×10^{-8} O 0.0171
520	17.27	57.5	38.3	5.07	2500	5.19	0.65	N_2 0.733 O_2 0.117 NO 0.0479 N 8.43×10^{-6} O 0.0892
521	20.87	60.0	34.2	5.51	2930	5.17	0.57	N_2 0.737 O_2 0.0763 NO 0.0382 N 4.75×10^{-5} O 0.135

Table A.10 Reservoir and freestream conditions for experiments using test gas air and a sphere of 1 in. diameter.

Shot No.	h_0 MJ/kg	p_0 MPa	ρ_∞ g/m³	u_∞ km/s	T_∞ K	Ma_∞	Re_∞ $\times 10^{-5}$	$c_{s,\infty}$ kg/kg
203	8.52	60.0	106	3.18	2030	4.60	8.87	CO_2 0.722 O_2 0.0996 CO 0.177 C 8.64×10^{-14} O 1.52×10^{-3}
204	5.30	60.0	148	2.70	1410	4.62	14.0	CO_2 0.893 O_2 0.0388 CO 0.0678 C 1.63×10^{-16} O 3.93×10^{-8}
207	4.62	60.0	162	2.58	1260	4.69	16.0	CO_2 0.923 O_2 0.0279 CO 0.0488 C 1.77×10^{-17} O 5.52×10^{-10}

Table A.11 Reservoir and freestream conditions for experiments using test gas carbon dioxide and a sphere of 6 in. diameter.

Shot No.	h_0 MJ/kg	p_0 MPa	ρ_∞ g/m³	u_∞ km/s	T_∞ K	Ma_∞	Re_∞ $\times 10^{-5}$	$c_{s,\infty}$ kg/kg
188	7.47	60.0	117	3.03	1860	4.52	6.66	CO_2 0.783 O_2 0.0787 CO 0.138 C 4.01×10^{-14} O 2.48×10^{-4}
189 190	8.52	60.0	106	3.18	2030	4.60	5.91	CO_2 0.722 O_2 0.0996 CO 0.177 C 8.64×10^{-14} O 1.52×10^{-3}
191	13.51	60.0	70.9	3.85	2400	4.90	4.07	CO_2 0.419 O_2 0.191 CO 0.369 C 4.63×10^{-13} O 0.0199
192	6.85	60.0	125	2.94	1740	4.51	7.27	CO_2 0.816 O_2 0.0669 CO 0.117 C 9.45×10^{-15} O 3.58×10^{-5}

Table A.12 Reservcir and freestream conditions for experiments using test gas carbon dioxide and a sphere of 4 in. diameter.

Shot No.	h_0 MJ/kg	p_0 MPa	ρ_∞ g/m³	u_∞ km/s	T_∞ K	Ma_∞	Re_∞ $\times 10^{-5}$	$c_{s,\infty}$ kg/kg
488	11.35	22.5	32.6	3.49	2010	4.92	1.94	CO_2 0.459 O_2 0.185 CO 0.344 C 7.73×10^{-13} O 0.0115
489 490	4.50	25.0	71.6	2.52	1130	4.78	4.99	CO_2 0.897 O_2 0.0374 CO 0.0655 C 5.18×10^{-18} O 2.69×10^{-11}
522 523	4.56	55.0	150	2.56	1240	4.71	9.96	CO_2 0.923 O_2 0.0281 CO 0.0492 C 1.01×10^{-17} O 3.03×10^{-10}
524	11.27	57.5	80.9	3.55	2260	4.77	4.53	CO_2 0.545 O_2 0.156 CO 0.289 C 3.24×10^{-13} O 9.16×10^{-3}

Table A.12(continued) Reservoir and freestream conditions for experiments using test gas carbon dioxide and a sphere of 4 in. diameter.

Shot No.	h_0 MJ/kg	p_0 MPa	ρ_∞ g/m³	u_∞ km/s	T_∞ K	Ma_∞	Re_∞ $\times 10^{-5}$	$c_{s,\infty}$ kg/kg
476	9.03	25.0	43.7	3.19	1850	4.69	1.94	CO_2 0.615 O_2 0.138 CO 0.245 C 2.36×10^{-13} O 1.68×10^{-3}
477	11.12	25.0	36.7	3.47	2020	4.89	1.62	CO_2 0.482 O_2 0.178 CO 0.329 C 6.99×10^{-13} O 9.95×10^{-3}
485	10.63	57.5	85.1	3.46	2220	4.74	3.56	CO_2 0.585 O_2 0.144 CO 0.264 C 2.68×10^{-13} O 6.87×10^{-3}
486	4.56	55.0	150	2.56	1240	4.71	7.47	CO_2 0.923 O_2 0.0281 CO 0.0492 C 1.01×10^{-17} O 3.03×10^{-10}

Table A.13 Reservoir and freestream conditions for experiments using test gas carbon dioxide and a sphere of 3 in. diameter.

Shot No.	h_0 MJ/kg	p_0 MPa	ρ_∞ g/m³	u_∞ km/s	T_∞ K	Ma_∞	Re_∞ $\times 10^{-5}$	$c_{s,\infty}$ kg/kg
500 509	4.50	25.0	71.6	2.52	1130	4.78	2.50	CO_2 0.897 O_2 0.0374 CO 0.0655 C 5.18×10^{-18} O 2.69×10^{-11}
501	10.63	57.5	85.1	3.46	2220	4.74	2.37	CO_2 0.585 O_2 0.144 CO 0.264 C 2.68×10^{-13} O 6.87×10^{-3}
502	7.18	70.0	140	3.00	1850	4.50	3.98	CO_2 0.810 O_2 0.0690 CO 0.121 C 2.51×10^{-14} O 1.42×10^{-4}
503	7.50	70.0	136	3.04	1910	4.52	3.30	CO_2 0.793 O_2 0.0750 CO 0.132 C 3.21×10^{-14} O 3.30×10^{-4}

Table A.14 Reservoir and freestream conditions for experiments using test gas carbon dioxide and a sphere of 2 in. diameter.

Shot No.	h_0 MJ/kg	p_0 MPa	ρ_∞ g/m³	u_∞ km/s	T_∞ K	Ma_∞	Re_∞ $\times 10^{-5}$	$c_{s,\infty}$ kg/kg
510	7.99	50.0	93.7	3.10	1900	4.56	2.66	CO_2 0.739 O_2 0.0941 CO 0.166 C 7.85×10^{-14} O 6.05×10^{-4}
515	11.95	25.0	34.4	3.58	2070	4.95	1.02	CO_2 0.432 O_2 0.191 CO 0.361 C 8.15×10^{-13} O 0.0150

Table A.14(continued) Reservoir and freestream conditions for experiments using test gas carbon dioxide and a sphere of 2 in. diameter.

Shot No.	h_0 MJ/kg	p_0 MPa	ρ_∞ g/m³	u_∞ km/s	T_∞ K	Ma_∞	Re_∞ $\times 10^{-5}$	$c_{s,\infty}$ kg/kg
516	5.96	55.0	126	2.80	1530	4.56	1.68	CO_2 0.857 O_2 0.0521 CO 0.0912 C 1.56×10^{-15} O 8.16×10^{-7}
517	10.63	57.5	85.1	3.46	2220	4.74	1.04	CO_2 0.585 O_2 0.144 CO 0.264 C 2.68×10^{-13} O 6.87×10^{-3}

Table A.15 Reservoir and freestream conditions for experiments using test gas carbon dioxide and a sphere of 1 in. diameter.